Studies on monolithic tandem structure for low cost and high efficiency dye-sensitized solar cells

Benjamin A. Grew

Submitted for the degree of Doctor of Philosophy

Heriot-Watt University

Engineering and Physical Sciences/Mechanical Engineering

August 2016

The copyright in this thesis is owned by the author. Any quotation from the thesis or use of any of the information contained in it must acknowledge this thesis as the source of the quotation or information.

Abstract

Multi junction solar cells are devices fabricated from two or more solar absorbers that absorb different parts of the solar spectrum. Typically this is done to yield a device with a superior efficiency to single junction devices derived from those absorbers and to surpass the efficiency limit of a single junction device (approx 30 %). The highest performing solar cells currently available are multi junction, but they are also the most expensive, typically restricting their use to applications that require a high power output from a small area. Another possibility for multi junction solar cells is to combine absorbers with a low production cost and simplicity to produce. This could potentially realise a solar cell with an efficiency greater than existing single junction technologies, but with a lower cost.

Absorbers such as the dye-sensitized solar cell (DSC or DSSC) are relatively simple and cheap to produce but are not currently being mass produced. By comparison the thin film technology, Cu(In,Ga)Se_2 or CIGS, is currently being manufactured for use commercially at a competitive price and performance to the current market leader, silicon. A tandem solar cell comprised of the DSC and CIGS absorbers has shown promise of an efficiency suitable for commercial application. Initially these tandem devices were demonstrated as a physical stack (one above the other) of the two separate solar cells connected electrically in series. The design has progressed to a monolithic design, highlighting several crucial areas requiring further development if the tandem is to prove successful.

Typical components of the DSC are sub-optimal for use in a tandem cell and require development of alternative approaches when combined into the proposed tandem cell. DSCs suffer drawbacks such as a lower efficiency and long term stability issues which has so far limited their commercial use. Optical losses from the transparent conducting oxide (TCO) used in both the DSC and CIGS absorb a small amount of light that is required by the CIGS. These parasitic losses ultimately reduce the overall performance of the tandem device. The work presented in this thesis makes use of pulsed DC sputtering to deposit titanium-doped indium oxide (ITiO), a material that is highly transparent across all the wavelengths absorbed in the DSC/CIGS. Pulsed DC sputtering reduces the time taken to deposit layers of ITiO whilst also exhibiting excellent electrical and optical performance, potentially reducing the overall cost of the DSC/CIGS tandem.

The monolithic configuration of the tandem leads to the electrolyte of the DSC

being brought into contact with the CIGS cell. The electrolyte is crucial to the operation of the DSC (and tandem) as an efficient hole conductor between the two absorbers. This electrolyte also corrodes the CIGS layer and complete device failure occurs within a matter of hours of device assembly. Use of another TCO, zinc oxide-doped indium oxide (IZO) is examined in this work, deposited in the amorphous phase to act as a barrier between the DSC electrolyte and the CIGS surface by preventing the electrolyte from reaching the CIGS through pinholes in the TCOs typically used as a top contact.

Finally the current-voltage (I-V) measurement of a solar cell determines critical parameters, of which includes the efficiency. The use of a mask across the DSC to accurately define the cell area is crucial for the measurement of its efficiency. This work demonstrates that applying this method to the tandem cell causes shading of the CIGS layer, resulting in a reduced electrical performance. A solution is proposed by modifying the device architecture to better match both absorber areas whilst preventing a short circuit between the DSC electrolyte and the CIGS back contact through the use of insulating SiO_2 layers.

List of Acronyms

TCO	Transparent Conducting Oxide
AZO	Aluminium-doped Zinc Oxide
ITiO	Titanium-doped Zinc Oxide
IZO	Zinc Oxide-doped Indium Oxide
FTO	Fluorine-doped Tin Oxide
ITO	Tin-doped Indium Oxide
CIGS	$Cu(In,Ga)Se_2$
DSC	Dye Sensitised Solar Cell
Isc	Short-circuit Current
Jsc	Short-circuit Current Density
Voc	Short-circuit Voltage
FF	Fill Factor
RF	Radio Frequency
PDC	Pulsed Direct Current
PV	Photovoltaic(s)
eV	Electron Volt
NIR	Near Infrared
XRD	X-Ray Diffractometry
EQE	External Quantum Efficiency
AM	Air Mass
kW	Kilowatt
TW	Terawatt

ACADEMIC REGISTRY
Research Thesis Submission

Name*:*			
School/PGI:			
Version: *(i.e. First, Resubmission, Final)*		Degree Sought (Award **and** Subject area)	

Declaration

In accordance with the appropriate regulations I hereby submit my thesis and I declare that:

1) the thesis embodies the results of my own work and has been composed by myself
2) where appropriate, I have made acknowledgement of the work of others and have made reference to work carried out in collaboration with other persons
3) the thesis is the correct version of the thesis for submission and is the same version as any electronic versions submitted*.
4) my thesis for the award referred to, deposited in the Heriot-Watt University Library, should be made available for loan or photocopying and be available via the Institutional Repository, subject to such conditions as the Librarian may require
5) I understand that as a student of the University I am required to abide by the Regulations of the University and to conform to its discipline.

* *Please note that it is the responsibility of the candidate to ensure that the correct version of the thesis is submitted.*

Signature of Candidate*:*		Date:	

Submission

Submitted By *(name in capitals):*	
Signature of Individual Submitting:	
Date Submitted:	

For Completion in the Student Service Centre (SSC)

Received in the SSC by *(name in capitals):*			
Method of Submission *(Handed in to SSC; posted through internal/external mail):*			
*E-thesis Submitted (**mandatory for final theses)***			
Signature:		Date:	

Please note this form should bound into the submitted thesis.

Updated February 2008, November 2008, February 2009, January 2011

List of Publications

B. Grew, J. W. Bowers, F. Lisco, N. Arnou, J. M. Walls and H. M. Upadhyaya. High mobility titanium-doped indium oxide for use in tandem solar cells deposited via pulsed DC magnetron sputtering. *Energy Procedia*, 60: 148-155, 2014.

P. J. M. Isherwood, A. J. Abbas, J. W. Bowers, B. Grew and J. M. Walls. Deposition of cupric oxide thin films by spin coating. *Materials Research Innovations*, 18, (2): 95-98, 2014.

B. Grew, J. W. Bowers and H. M. Upadhyaya. The optimization of optical properties for increased performance in a monolithic tandem dye-sensitized/Cu(In, Ga)Se_2 solar cell. *Photovoltaic Specialists Conference* (*PVSC*), 2013 IEEE 39th: 1008-1012, 2013.

B. Grew, J. W. Bowers and H. M. Upadhyaya. Zinc oxide-doped indium oxide (IZO): an amorphous transparent conducting oxide for use in tandem solar cells. *9th Photovoltaic Science Application and Technology* (*PVSAT*9), Swansea University 2013.

B. Grew, J. W. Bowers and H. M. Upadhyaya. Pulsed dc sputtered titanium-doped indium oxide as a high mobility transparent conducting oxide for tandem solar cells. *7th Photovoltaic Science Application and Technology* (*PVSAT*7), Heriot-Watt University 2011.

Contents

1 INTRODUCTION **1**

1.1 Energy From the Sun 2

1.1.1 The Solar Spectrum and Air Mass 2

1.2 Photovoltaic Devices 4

1.2.1 The Photovoltaic Effect 4

1.2.2 Semiconductors 5

1.2.3 Semiconductor Doping 6

1.2.4 The p-n Junction Solar Cell 7

1.2.5 Solar Cell Performance and the Shockley-Queisser limit 8

1.3 The Evolution of Photovoltaic Devices 9

1.4 Scope of Thesis 14

2 LOW COST ABSORBERS FOR USE IN TANDEM SOLAR CELLS 16

2.1 Introduction 16

2.2 The Dye-Sensitised Solar Cell 18

2.2.1 Fabrication and Performance 19

2.2.2 Working Electrode 20

2.2.3 Sensitising Molecules 22

2.2.4 Hole Conducting Electrolyte 25

2.3 Cu(In,Ga)Se_2 Solar Cells 28

2.3.1 Device Materials, Architecture and Performance 28

2.3.2 Vacuum Deposition Methods 31

2.3.3 Non-vacuum Deposition Methods 32

3 EXPERIMENTAL METHODOLOGY **35**

3.1 Magnetron Sputtering of TCOs 35

3.2 Material Characterisation 37

3.2.1 UV-Vis-NIR Spectrophotometry 37

3.2.2 Sheet Resistance and Hall Effect Measurements 38

3.2.3 X-Ray Diffraction (XRD) 40

3.2.4 Scanning Electron Microscopy (SEM) and Transmission Electron Microscopy (TEM) 40

3.3 Device Fabrication 40

3.4 Device Characterisation 42
3.4.1 Current-Voltage (I-V) Measurements 42
3.5 Conclusion 44

4 HIGH MOBILITY TRANSPARENT CONDUCTING OXIDES FOR USE IN TANDEM SOLAR CELLS 45
4.1 Introduction 45
4.1.1 Requirements of TCOs as Tandem Cell Contacts 46
4.1.2 High Mobility TCOs 46
4.2 Titanium-doped indium oxide 47
4.2.1 Optimisation of opto-electronic properties of titanium-doped indium oxide 48
4.3 Pulsed DC Magnetron Sputtering of ITiO Thin Films 52
4.3.1 Motivation 52
4.3.2 Results 53
4.4 Conclusion 63

5 THE MONOLITHIC DYE-SENSITISED/Cu(In,Ga)Se_2 TANDEM SOLAR CELL 64
5.1 Introduction 64
5.2 Progress on a Monolithic Design 66
5.3 Measurement of a DSC/CIGS Tandem Device 67
5.3.1 Results 69
5.3.2 Effects of Shading 69
5.4 Optimisation of Optical Parameters in the Monolithic Tandem Cell for Enhanced Performance 71
5.4.1 Improvements 73
5.4.2 Potential Strategies to Eliminate Corrosion in the Tandem Solar Cell 76
5.5 Conclusion 76

6 APPLICATION OF AMORPHOUS TRANSPARENT CONDUCTING OXIDES IN TANDEM SOLAR CELLS 78
6.1 Introduction 78
6.1.1 Amorphous Transparent Conducting Oxides 78
6.2 Zinc oxide-doped indium oxide thin films 79
6.2.1 Motivation 80
6.2.2 Results 80
6.3 Prevention of Electrolytic Removal of CIGS in a DSC/ CIGS Tandem by Incorporating an Amorphous Transparent Conducting Oxide . . . 88
6.3.1 Motivation 88
6.3.2 Results 89

6.4 Conclusion 98

7 POTENTIAL CONFIGURATIONS OF LOW-COST TANDEM SOLAR CELLS 99

7.1 Introduction 99
7.2 Motivation 100
7.3 Methodology 100
7.3.1 Model Design 100
7.4 Results 104
7.5 Conclusion 109

8 CONCLUSIONS 111

8.1 Future Directions 113

List of Figures

1.1 The spectral irradiance of AM0, 1.5 and 2 plotted alongside the spectral irradiance of a blackbody with T=5800 K, according to Planck's law 3
1.2 An example of how axial tilt of the Earth's axis gives rise to seasonal change 4
1.3 A sketch diagram, crudely depicting the valence band maxima, E_v and conduction band minima, E_c in a metal, semiconductor and insulator. 5
1.4 A simplified Bohr model diagram depicting the covalent bonding in p-type and n-type doped silicon and the resultant de-localised hole and electron that are generated. 6
1.5 A picture of the formation of a depletion region in a p-n junction. . . 7
1.6 Band energy diagram of a p-n homojunction. 8
1.7 The efficiency chart of advances in solar cell technologies. 11
1.8 A schematic cross section of the monolithic DSC/Cu(In,Ga)Se_2 tandem solar cell described and fabricated in this thesis. 14

2.1 A visual description of each layer in the InGaP/GaAs/InGaAs III-V multijunction stack. 17
2.2 A simplified electron energy level schematic describing the conversion of photons to electrical energy in a dye-sensitised solar cell. 18
2.3 A schematic cross section of a typical dye-sensitised solar cell. 19
2.4 Three commonly used ruthenium based photosensitisers. 24
2.5 The porphyrin based dye, YD2-o-C8, capable of efficiencies over 10 %. 24
2.6 A coumarin based dye, NKX-2677, able to demonstrate a high efficiency of 6 % in a solid state DSC. 27
2.7 Cu-In-Se phase diagram depicting the possible phases from Cu, In and Se precursors. 29
2.8 A collapsed view of the materials used and their typical thicknesses in a common CIGS solar cell. 30

3.1 A representation of magnetron sputtering with ionised argon atoms in pink and loose target particles in grey. 36
3.2 A visual representation of how incident light, I_0, is initially reflected, R and then transmitted, I_x, through a solid material with thickness, d. 38

3.3 A basic visualisation of the 4 point probe configuration with the TCO below. 39
3.4 An equivalent circuit of a non-ideal solar cell locating the series and shunt resistances in a solar cell. 42
3.5 An ideal I-V curve from a solar cell plotted using modelled data. . . . 43

4.1 A comparison between FTO TEC8 and as-deposited ITiO 47
4.2 Comparison of ITiO films deposited by RF magnetron sputteirng for 30 minutes each at increasing pressure and O_2 partial pressures. . . . 51
4.3 Transmission properties of all deposited ITiO films described in this study. 55
4.4 XRD diffractograms of both the RF and PDC deposited ITiO thin films. 57
4.5 Scanning electron micrograph images of ITiO films deposited at various working pressures by a RF power supply. 58
4.6 Scanning electron micrograph images of ITiO films deposited at various working pressures by a PDC power supply. 59
4.7 Scanning transmission electron micrograph cross section images of the ITiO films deposited by a RF power supply. 60
4.8 Scanning transmission electron micrograph cross section images of the ITiO films deposited by a PDC power supply. 61
4.9 I-V curves for DSCs fabricated on ITiO deposited by RF and PDC power supplies. 62

5.1 The External Quantum Efficiency (EQE) of both a dye-sensitised and Cu(In,Ga)Se_2 solar cell. 65
5.2 A schematic cross section of the monolithic DSC/Cu(In,Ga)Se_2 tandem solar cell. 66
5.3 I-V curves of the single DSC finished with a typical FTO counter electrode and a CIGS device. 68
5.4 I-V curves of the monolithic tandem cell, two measurements are shown to highlight the differences between using a mask to measure the cell area. 69
5.5 I-V curves of a modelled PV device, shaded at different percentages to demonstrate the effect of partial shading on the performance of a PV device. 70
5.6 A photograph depicting the modifications to the CIGS layer necessary to reduce shading losses from measurement of the DSC/CIGS tandem. 72
5.7 I-V measurements of the monolithic tandem device with a reduced CIGS area, measured with both the mask and without the mask. . . . 73
5.8 I-V curves of several DSCs fabricated with various thicknesses of SiO_2 deposited on the platinised counter electrode, detailing the resistive losses in the device. 74

5.9 The self-adhesive mask used to etch a specific area of a CIGS absorber 75

6.1 Transmission properties of the first IZO film, 13A0038, deposited from a ceramic target. 81
6.2 Transmission vs wavelength for all IZO films deposited during the optimisation process, with varying temperature, pressure and oxygen concentration. 84
6.3 Transmission vs wavelength for IZO films deposited at varying power supplied to the target. 85
6.4 Comparison of the redshift observed between the amorphous TCO, IZO and crystalline AZO with increasing thickness. 86
6.5 A tauc plot, calculating the band gap of the IZO films by extrapolation of the x axis intercept of the linear function for the plot of $(\alpha h\nu)^{0.5}(eV^2cm^{-2})$ vs $h\nu$. 87
6.6 The Urbach tailing scheme, as outlined by Boubaker. 88
6.7 The SnO_2/Au/AZO (200 nm) stack under magnification following immersion in DSC electrolyte. 90
6.8 The SnO_2/Au/AZO (1000 nm) stack under magnification following immersion in DSC electrolyte. 91
6.9 The SnO_2/Au/IZO (ca.200 nm) stack under magnification following 180 minutes immersion in DSC electrolyte. 92
6.10 The SnO_2/Au/IZO (ca.500 nm) stack under magnification following immersion in DSC electrolyte. 93
6.11 The SnO_2/Au/IZO (ca.3 μm) stack under magnification after 180 minutes immersion in DSC electrolyte 94
6.12 The SnO_2/Au/IZO bilayer stack under magnification following immersion in DSC electrolyte. 95
6.13 The SnO_2/Au/SnO_2 (1 μm) stack under magnification following immersion in DSC electrolyte. 96

7.1 A depiction of the interfaces indicent light must pass through to get to the CIGS solar cell, used in this chapters model. 101
7.2 Absorbance, transmission and reflectance data as a percentile for 1.1 mm glass, TEC8 fluorine-doped tin oxide and unsensitised TiO_2. . . . 103
7.3 Measured absorbance, transmission and reflectance of a DSC with a 8 μm thick TiO_2 layer sensitised with N719 dye. 104
7.4 Modelled data for % transmission of indicent photons through modelled stacks at varying DSC thicknesses. 105
7.5 Modelled data for % transmission of incident photons through modelled stacks at varying DSC thicknesses. 106
7.6 Modelled data for % transmission of incident photons through modelled stacks at varying DSC thicknesses. 107

7.7 Modelled data for % transmission of incident photons through a modelled stack at varying DSC thicknesses. 108
7.8 Modelled data of transmission (%) for FTO/DSC/ITO and ITiO/DSC/IZO stacks compared against EQE data of CIGS absorbers with different indium/gallium ratios. 109

List of Tables

4.1 Deposition conditions and film sheet resistances of ITiO films deposited with different oxygen in plasma concentrations. 50
4.2 Deposition conditions of the films grown to compare the differences between ITiO films grown using RF and pulsed DC power supplies. . 53
4.3 Deposition rates for all ITiO films deposited by both RF and PDC. . 54
4.4 Device parameters of DSCs fabricated on both RF and PDC deposited ITiO films (13A0314 and 13A0337 respectively). 63

5.1 Comparison of the performance of a typical DSC using fluorine-doped tin oxide as the TCO, a DSC using ITiO as the TCO and a CIGS solar cell. Light scattering layers were used in both DSCs. 68
5.2 Performance parameters of the monolithic tandem cell when masked to an area of 0.196 cm^2 or unmasked with the area estimated at 0.282 cm^2. 69
5.3 Performance of the reduced CIGS area monolithic tandem device measured with both the mask and without, detailing the similarities between both devices. 73

6.1 Deposition parameters for the optimisation of IZO thin films. 82
6.2 Electronic parameters of all IZO films deposited during optimisation. 82
6.3 Electrical characterisation of IZO thin films deposited at room temperature, 120 W and 1 mTorr. 85

Chapter 1

INTRODUCTION

During the 1800s the industrial revolution rapidly changed the way we live across the world. In its wake a time of creation, invention and innovation has followed, in a quest for a better standard of living. This continued development has resulted in a dependence on several forms of energy, provided primarily by burning fossil fuels. Despite the numerous and significant developments in our understanding of science and technology, we are still yet to break our reliance on these 'dirty' fossil fuels for energy generation.

Fossil fuels boast a high energy output whilst only requiring the most basic of operation to maintain: fuel, oxygen and heat. Their simplicity to use has come at a price: it is well known and to an extent accepted that the release of carbon dioxide from burning these fuels has lead to global climate change, a process whereby the planet's complex ecosystem is disturbed. One of the more iconic potential outcomes from climate change discussed is the melting of the polar ice caps, which would lead to an increase in global ocean water levels and reduction in available land mass. More recent acute changes in weather and seasonal patterns have been attributed to global warming, such as increased rainfall causing heavier floods and stronger seasonal events.

Regardless of data to suggest oil reserves are extensive, fossil fuels are a finite resource and their availability will eventually decline. The inability to meet the developed worlds demand for oil has been seen before over the last 100 years, especially during the 1973 OPEC crisis; If we are still reliant on this fuel when available reserves become depleted, the remaining supply will become an expensive luxury resource [1]. Researchers across the globe have therefore sought after several alternative energy generation methods, planning for a time where fossil fuels have either been depleted or are scarce.

Several alternatives have appeared since the 1940's with the most immediately viable being nuclear fission; however others such as solar photovoltaics, wind, nuclear fusion, biomass and hydroelectric energy are beginning to gain traction due to their intrinsic safety and low operating cost. This thesis will focus on the materials and design of solar photovoltaic (PV) devices for use in electricity generation.

1.1 Energy From the Sun

Life on Earth would not exist without the Sun. It is one of the constant factors that has enabled life to evolve and flourish over billions of years. All life in the planet's ecosystem relies on the Sun for energy either to produce their own food, such as plants, or by preying on other organisms who consume these plants. Plants use sunlight in a process called photosynthesis to convert solar energy to chemical energy, which in turn produces food. These reaction sites, called 'chloroplasts' are mainly present in the plant's leaf and benefit from having a large surface area exposed to direct sunlight. In tropical rainforests the competition between other plants have led to a complex ecosystem of trees growing to an enormous height with fascinating adaptations in order to enhance the area exposed to the sun. Photosynthesis itself is a complex, highly adapted process specific to the production of food and not large quantities of stored electrical energy. Of the light that a plant receives, only low energy red photons are used, the rest reflected - leading to the green appearance of the leaves.

It is believed that all plants in the world are able to generate, on average, 100 Terawatts (TW) of energy [2]. This is a truly staggering amount, given that photosynthesis does not utilise all of the sunlight it is exposed to. In context our civilization currently generates roughly over 5 TW of electrical energy, which is only likely to increase [3].

For practical solar electrical generation the process used would need to be much more efficient than that of photosynthesis. It would be impractical to occupy a similar sized area of the Earth that plants occupy to generate electricity from the sun (parts of the Earth's land mass appears green from orbit!).

Space is therefore an important consideration as we cannot cover our planet in solar panels, due to the problems it would cause to the ecology of the planet. Therefore an ideal solar cell would absorb as much sunlight as possible in as small an area, whilst efficiently converting it into electrical energy. In order to design a cell with this specification we need a comprehensive understanding of the materials we can use to convert light into energy and the light we can utilise.

1.1.1 The Solar Spectrum and Air Mass

The Sun is a massive nuclear fusion reaction, converting low atomic mass elements into larger atomic mass elements, releasing a tremendous amount of electromagnetic radiation. From the Earth's surface the radiation emitted from the Sun may be described as a blackbody using Planck's law, with a temperature of 5800 K. As such the spectral irradiance, I_λ, can be plotted against wavelength [4]:

$$I_\lambda = \frac{2hc^2}{\lambda^5} \frac{1}{e^{\left(\frac{hc}{k_B \lambda T}\right)} - 1} \tag{1.1}$$

Where h, c and k_B are constants, λ is the wavelength of radiation measured and

T is temperature in Kelvin. This theoretical spectrum of radiated energy from the Sun is plotted in Figure 1.1. This closely follows what has been measured outside of the Earth's atmosphere, which is also plotted in Figure 1.1 as $AM0$, meaning no atmosphere.

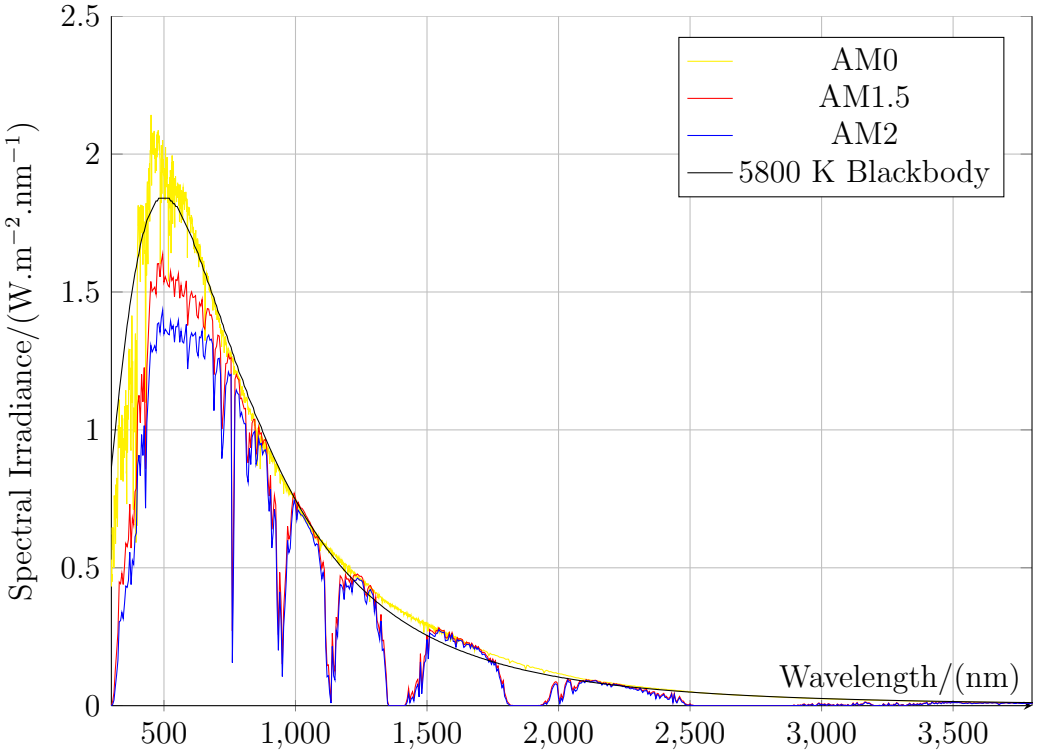

Figure 1.1: The spectral irradiance of AM0, 1.5 and 2 reproduced from [5]. Plotted alongside is the approximated spectral irradiance of a blackbody with T=5800 K, according to Planck's law.

Although this blackbody approximation is helpful to determine the potential available spectral irradiance, it is not indicative of what will arrive at the surface of the Earth. The Earth's atmosphere is able to absorb several different frequencies of visible and infra-red radiation from compounds present (O_3, O_2, H_2O and CO_2). These bands of absorption can be seen in Figure 1.1 in the AM1.5 and AM2 spectra at ca. 750 nm, 930 nm, 1125 nm, 1350 nm and 1800 nm. The angle of the Sun above the Earth will affect the distance the light must travel to reach the surface of the Earth, which increases the absorption of these wavelengths. Air Mass is therefore used to describe the relationship of incoming radiation of a given path length, L, at an incident angle at a surface, θ, relative to the Zenith path length, L_0:

$$Air\ mass = \frac{L}{L_0} \approx \frac{1}{cos\theta} \tag{1.2}$$

The American Society for Testing and Materials (ASTM) release reference data in an attempt to unify testing conditions for solar cells, so that research groups and commercial enterprises may make useful comparisons of solar cell performance. This reference data uses modelled AM 1.5G for the surface of incident irradiation and can

be seen in Figure 1.1 [5]. These conditions were chosen as they are representative of average latitude in the 48 contiguous states of the USA, but more conveniently the maximum power available is ca. 1000 Wm^{-2} when the spectral irradiance of AM1.5G is integrated [6]. In addition to air mass the axial tilt of the Earth on its orbit (23.5°) plays a pivotal role in seasonal change due to the uneven distribution of incoming radiation from the sun. This is represented in Figure 1.2 where the seasonal change can be depicted due to the axial tilt of the Earth. As a result seasonal change will contribute to the amount of sunlight there is for a PV device to convert into electricity, winter months will see a reduced solar resource relative to the summer months.

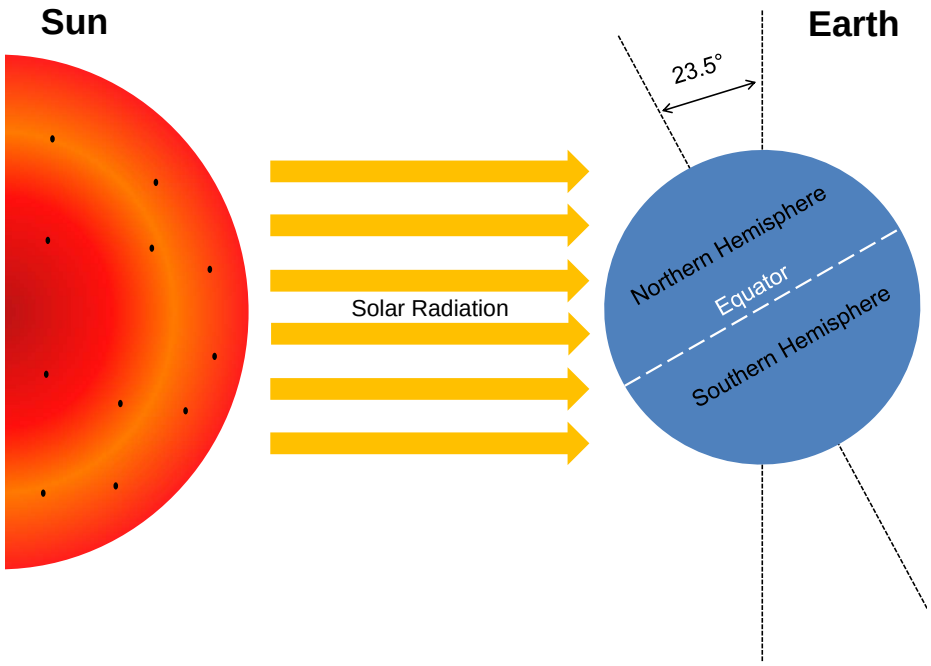

Figure 1.2: An example of how the axial tilt of the Earth can cause seasonal change due to the change in surface area exposed to incoming radiation. Here the northern hemisphere is experiencing summer and has a larger surface area exposed to the sun than the southern hemisphere and will therefore have a higher temperature relative to the southern hemisphere.

1.2 Photovoltaic Devices

1.2.1 The Photovoltaic Effect

The process whereby an electrical current is generated in a material directly from sunlight is referred to as the photovoltaic effect. It was first documented in 1839 by Edmund Becquerel, who noticed that two electrodes in an electrolyte solution could generate a small electrical current, based on the choice of metal(s) used as the electrodes, which increased when placed in direct sunlight. In modern photovoltaic

devices this effect is used as the principal method for electrical current generation, typically through the use of semiconducting materials.

1.2.2 Semiconductors

A semiconductor is a material that, dependant on conditions, may exhibit slight conducting properties. With respect to conducting properties, a semiconductor will lie between a resistor and conductor. Typically a semiconductor requires an external input of energy in order to conduct a significant electrical current, with conducting performance decreasing close to that of an insulator as temperatures tend towards 0 K. The difference in conductivity between conductors, semiconductors and insulators are dependent on their electron valence and conduction band energy levels. Electrons occupy orbitals around their respective atomic/molecular nuclei, confined to a series of allowed energy levels. Electrons initially fill the energy orbitals lowest in energy, closer to the nucleus, compliant with the Rutherford-Bohr model. As more electrons are present orbitals higher in energy will become occupied with a distance further away from the nucleus.

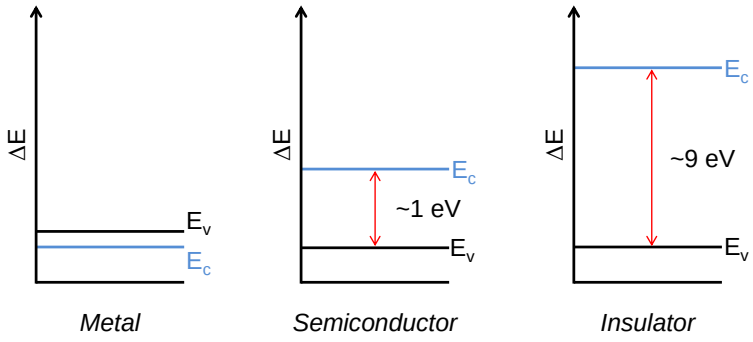

Figure 1.3: A sketch diagram, crudely depicting the valence band maxima, E_v and conduction band minima, E_c in a metal, semiconductor and insulator. The band gap is the difference in energy between the valence and conduction band. The band gap energy in the diagram is approximated for semiconductors, although this value will vary with material, for example silicon has a bandgap of 1.1 eV.

In a semiconductor and/or insulator the highest occupied molecular orbitals (HOMO) are termed the valence bands. After the valence band a series of higher electron energy states exist, which are the lowest unoccupied molecular orbitals (LUMO) and these are termed the conduction band. These two bands are separated by an area where electron energy states are forbidden, this region is the band gap. As LUMO states are occupied in a semiconductor its ability to conduct an electrical current will increase. Electrons promoted to the conduction band in a semiconductor must have an external input of energy equal to or greater than the energy of the band gap, shown in Figure 1.3. By comparison a metal has the intrinsic ability to conduct an electrical current, due to the overlap of its valence and conduction bands, resulting in

no band gap. In an insulator the band gap is so large that it is not able to conduct an electrical current. In photovoltaic devices this external source of energy is provided by absorbed photons from the sun.

1.2.3 Semiconductor Doping

Through the deliberate introduction of impurities into an intrinsic semiconductor it is possible to change its electrical properties, a process known as doping. Semiconductor doping is carried out to produce a semiconductor either deficient in electrons (p-doped) or have an excess of electrons (n-doped).

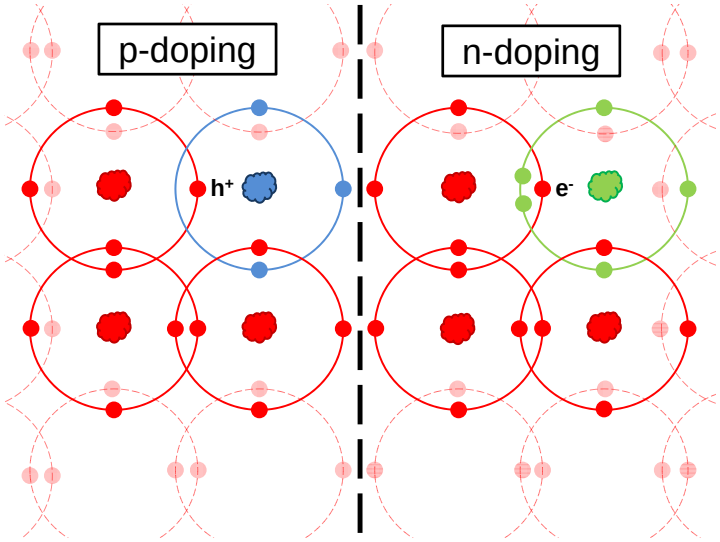

Figure 1.4: A simplified Bohr model diagram depicting the covalent bonding in p-type and n-type doped silicon and the resultant de-localised hole and electron that are generated.

The choice of dopant relies on the valence electron count of the semiconductor and whether the semiconductor needs to be p- or n- type. Silicon is a group IV semiconductor with four valence electrons; to introduce an electron deficiency (p-doping) a group III element would have to be added to the crystal structure, such as boron or aluminium which both have three valence electrons. To introduce an excess of electrons (n-doping) a group V element such as nitrogen or phosphorous would have to be added, due to their five valence electrons. Impurity atoms will fit into the semiconductor crystal structure, forming covalent bonds with four other silicon atoms, as demonstrated in Figure 1.4. By p-doping a semiconductor, the lack of an additional electron to form an electron bond pair creates a hole, a gap state due to the absence of an electron. By n-doping the semiconductor the excess electron introduced from the dopant atom is promoted into the conduction band. De-localised electrons introduced by n-doped will typically occupy the conduction band, as such semiconductors will display an increased ability to conduct an electrical current with increased n-doping. Typically the concentration of both forms of doping is in the parts

per million (ppm) range, although in highly n-doped semiconductors the increase in de-localised electrons may cause the semiconductor to begin to behave similarly to a metal, known as degenerate doping.

1.2.4 The p-n Junction Solar Cell

The semiconductor p-n junction could be described as one of the most important discoveries of the 20th century, giving rise to solid state transistors used in microprocessors. The invention of the transistor by Bell Laboratories in 1947 allowed the rapid reduction in size of computers of the day, as well as an increase in performance. The simplest p-n junction is a stacking of a p-type semiconductor and an n-type semiconductor that have been brought into contact to form a junction. This junction is not formed by physically placing one on top of the other, but by methods such as diffusion in crystalline silicon or using thin film deposition methods such as sputtering or evaporation to form one layer on top of another. When the junction is formed between p-doped and n-doped semiconductors a depletion zone will form, shown in Figure 1.5.

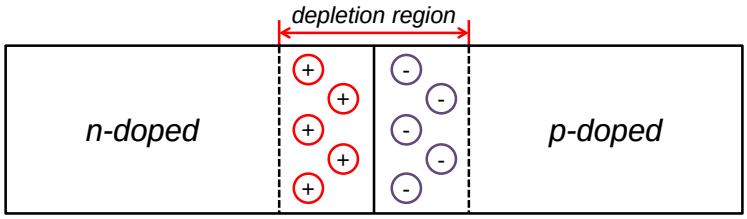

Figure 1.5: A picture of the formation of a depletion region in a p-n junction.

The absorption of a photon with energy greater than the band gap, by the p-n junction will provide an electron enough energy to occupy a state in the conduction band. Whilst the electron becomes mobile it leaves in its place an electron hole, a carrier that represents the lack of electron in a given space. Free carrier electrons from the n-doped region will diffuse into the p-doped region; the same is true of holes from the p- to n- region. This deficiency of electrons in the n-region and deficiency of holes in the p-region lead to the generation of positive and negative ions. This region of ions at the junction interface forms the depletion zone and gives the junction a built in potential, paramount to the functionality of the p-n junction. Eventually the diffusion process becomes suppressed due to the electric field effect generated by this depletion region, which stops further generation of ions and establishes an equilibrium for the junction.

It is possible to calculate the efficiency at which conversion of photons to electrons within the solar cell takes place. This is known as the energy conversion efficiency, η, and is an important benchmark measurement when judging solar cell performance.

Once an electron-hole pair is generated following the absorption of a relevant photon, they are separated by the built in charge of the p-n junction. Failure to do this results in decay of the excited electron leading to recombination of the electron-hole pair causing a loss in potential current and therefore a lower efficiency.

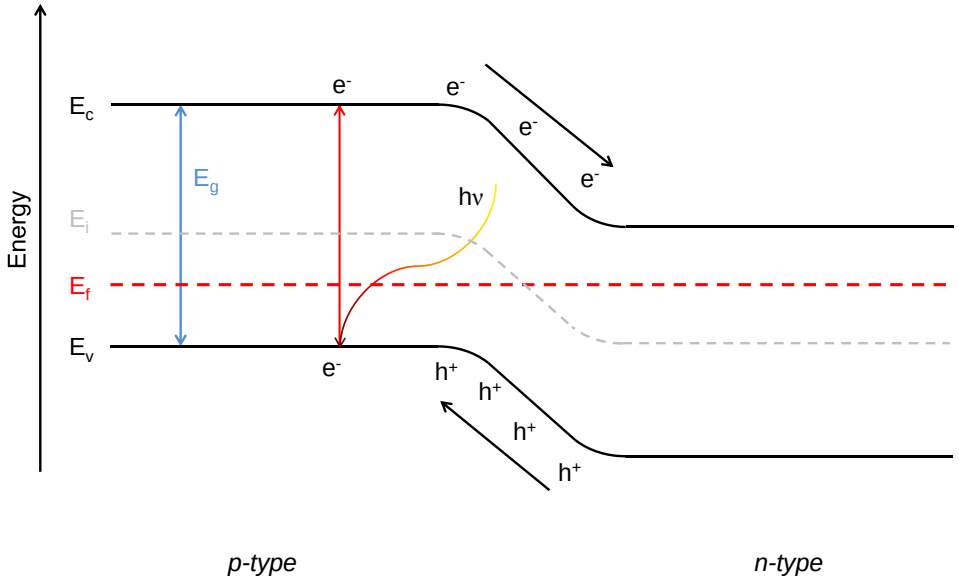

Figure 1.6: Band energy diagram of a p-n homojunction.

The basic operation of a homo-junction p-n junction is described in Figure 1.6 in relation to the semiconductor energy bands. Electrons in the p-type semiconductor are promoted from the valence band, E_v, to the conduction band, E_c, through the absorption of a photon. The energy of the photon must have energy equal to or greater than the band-gap, E_g, to create an electron-hole pair. The electron-hole pair are separated by the built in potential from the n-type semiconductors lower conduction band energy level and leaves the p-n junction through a closed circuit. The electrons once in the n-type semiconductor conduction band will eventually recombine with holes in the valence band. The device voltage under illumination and open circuit is referred to as the open circuit voltage, V_{oc}, and is determined by the difference between the Fermi energy of each doped semiconductor.

1.2.5 Solar Cell Performance and the Shockley-Queisser limit

Solar Cell Performance

Dependent upon the band-gap of an absorber material, different parts of the solar spectrum are absorbed. Not all semiconducting materials have identical band-gaps and these values can be altered by several factors, such as the doping concentration or changes in the material crystalline structure. The photon energy required for an electron to be promoted to the conduction band (typically referred to as the band-gap) is directly related to the wavelength of light:

$$E\,(eV) = \frac{hc}{\lambda} = \frac{1239.8\ nm}{\lambda} \tag{1.3}$$

On absorption of a photon with energy equal to or greater than the band-gap, an electron-hole pair are created and separated by the built in charge of the p-n junction. Photons with an energy above the band-gap are still absorbed, creating an electron-hole pair, but any excess energy is lost through thermal emission.

The Shockley-Queisser Limit

As seen previously in Figure 1.1 the spectral irradiance the Earth receives is not evenly distributed. As a result not all absorbing materials used in PV devices are considered to be optimal, as their band-gap does not match the peak spectral irradiance based on a blackbody emitter at 5800 K. It has been calculated that the maximum theoretical efficiency achievable, often termed the Shockley-Queisser limit, is 30 % from a material with a band-gap of 1.1 eV when matched to a blackbody of 6000 K [7]. Substitution of the blackbody radiation with the AM 1.5G spectrum later found that the ideal band-gap would be 1.4 eV [8].

Silicon solar cells, which hold an efficiency record of 25.0 %, have benefited from over 40 years of intensive research [9]. However the first certified efficiency of ca. 13 % was recorded in 1977, with the now highest efficiency of 25.0 % reached in 1998 [10]. Silicon solar cells are currently dominating the PV market for commercial and domestic installations and research is continuing to boost its efficiency close to this theoretical limit. Alternatively GaAs cells have also been produced capable of reaching an efficiency of 28.8 %, setting the efficiency for a single junction solar cell [9].

As we approach higher efficiencies close to the theoretical maximum limit it becomes more difficult to engineer performance increases. A combination of one or more p-n junction absorbers to form a multi-junction solar cell is a viable alternative to increase the efficiency of a solar cell above the single junction theoretical limit. This idea focuses on using absorbers which absorb different portions of the solar spectrum, to increase the voltage or current of the device, depending on whether it is configured in series or parallel. The theoretical use of 36 energy gap cells will produce a maximum efficiency device of 72 % [8]. Combining multiple band-gap cells to form a single device has been applied successfully in InGaP/GaAs/InGaAs cells, which have reached a record efficiency of 38.8 % which surpasses the limit for a single junction device and is consequently the most efficient PV device to date [9].

1.3 The Evolution of Photovoltaic Devices

There are several different materials which exhibit photovoltaic properties and as a result, several different technologies exist based on these various absorber materials

and their many architectures. Each absorber not only has advantages based on its absorption characteristics, but also from its complexity and cost to produce. The National Renewable Energy Laboratory in the U.S.A. produces a frequently updated chart, logging the record efficiencies for each type of main solar cell technology. This chart is reproduced in Figure 1.7 [11].

Crystalline Solar Cells

The potential of solar power was realised in the mid 20th century with cells based on mono-crystalline silicon. The unique behaviour of p-n junctions meant that a significant amount of development on the p-n junction focused on developing the first transistor, prior to the energy crisis of the 1970s. As the semiconductor industry began to grow in the second half of the century, knowledge gained was applicable to improving the performance of silicon PV. These improvements eventually led to solar cells being fitted to a man-made satellite over the use of a battery, a practice which is now commonplace [12]. The first generation of solar cells were typically crystalline in nature, such as GaAs and c-Si. The approach with these devices has been to develop high efficiency, large area (in modules), (mono) crystalline (c-Si) devices that can operate as close to the theoretical maximum efficiency as can be economically manufactured. This approach has led to the fabrication of a silicon cell with an efficiency of 25.0 %, the highest of any single junction silicon device [13].

Silicon has a band gap of approximately 1.1 eV and also has an indirect band gap, leading to photons penetrating further into the absorber layer before being absorbed [14]. Gallium Arsenide (GaAs) was a strong competitor to c-Si cells due to its wider direct band gap, offering efficiencies of up to 20 % even in the 1970s [15]. In recent years GaAs cells have found inclusion in high performance solar cells used in space due to their resistance to radiation damage [16]. Despite the higher efficiencies demonstrated by GaAs over c-Si a lack of abundant precursors, perceived toxicity due to the use of arsenic, and an inferior manufacturing infrastructure has led to Si based technologies being the dominant technology in the solar energy market [17]. With some 40 years of research into silicon cells, it is often considered that all that can be improved has been, thus leading to a drive to reduce the high production costs to become more competitive with wholesale energy. Major cost decreases can be attributed to the development of alternative silicon growth techniques such as poly-crystalline [18] and quasi-mono crystalline [19]. Though this cost reduction can in turn reduce purity of the silicon resulting in a reduced performance.

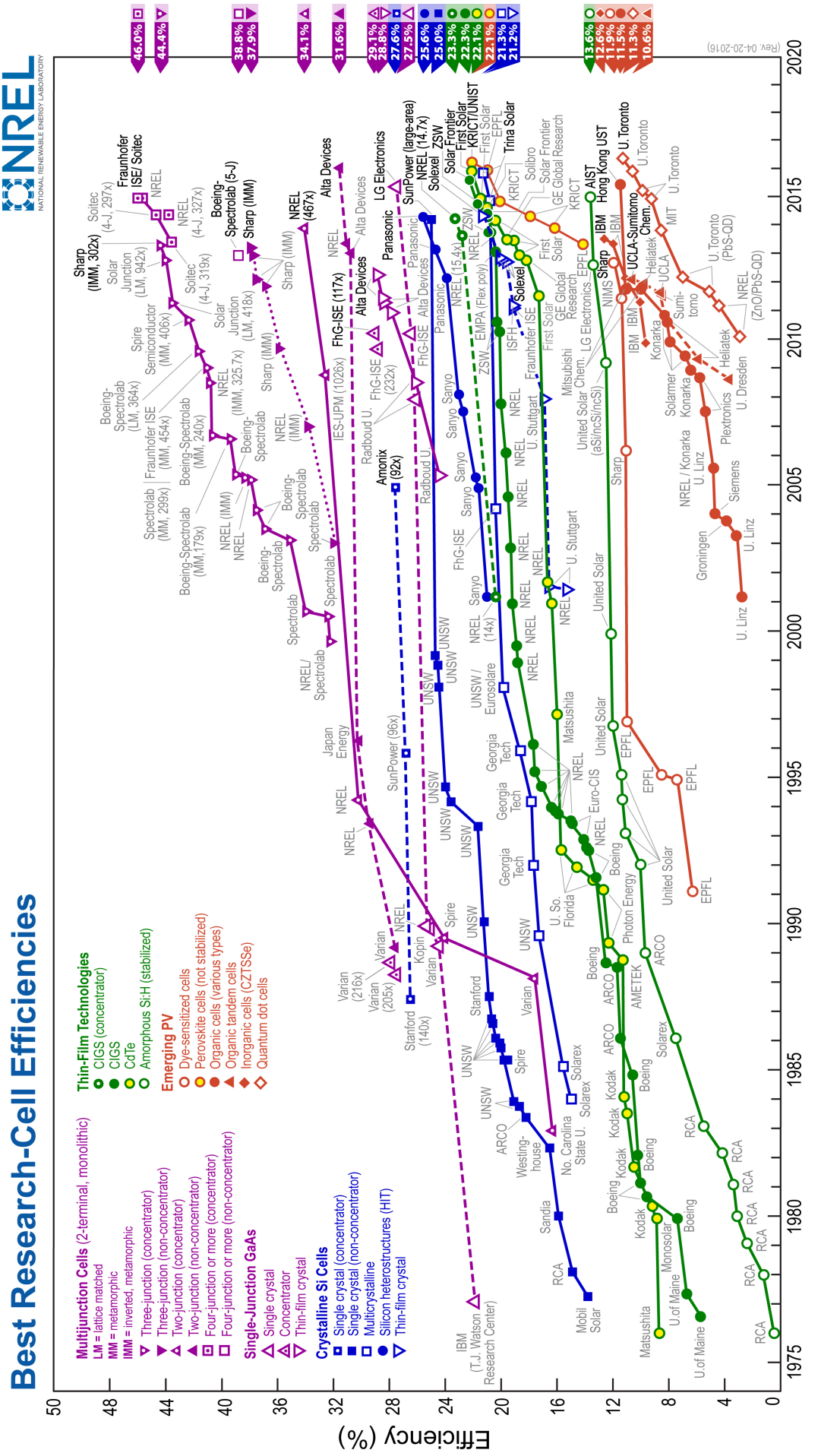

Figure 1.7: The National Renewable Energy Laboratory in the USA regularly updates this chart with advances in efficiency of solar cell technologies [11]

Thin-film technologies

Thin film cell designs only require a solar absorber to be a few microns thick, greatly reducing the amount of material required for production. The reduction in materials required has led to thin film devices (particularly Cu(In,Ga)Se_2 and CdTe) to be lower in cost than Si devices. Thin film technologies include cadmium telluride (CdTe) [20]; Cu(In,Ga)Se_2 (copper indium gallium sulfide/selenide) [21]; (Cu,In)S/Se_2 (copper indium sulfide/selenide) [22]; Cu_2S/CdS (copper sulfide/cadmium sulfide) [23]; and amorphous silicon (a-Si) [24]. CIGS currently offers the best efficiency (21.7 %) of all thin-film absorbers, close to multi-crystalline-Si and just short of mono-crystalline-Si [25]. Thin film devices are still based on the same p-n junction design, but employ different manufacturing methods to silicon. Magnetron sputtering and chemical evaporation deposition (CVD) were two already existent widespread, robust processes in industry that were used in the manufacture of thin film cells. Despite the reduction in material usage sputtering and CVD have drawn criticism due to a relatively high material waste (30-50 %).The use of rare earth metals in these technologies (indium, gallium and tellurium) has often questioned whether supply will ever be able to sustain demand. Companies such as First Solar, a manufacturer of CdTe cells, recycle their cells at the end of life [26]. This ensures a constant supply of cadmium and tellurium for new cells, whilst making sure these toxic materials are not simply land filled. First Solar have set up two of these recycling plants at each of their global manufacturing sites, with capital set aside to fund this project, with the capability to recycle approximately 95 % of semiconductor materials. The registration policy of First Solar regarding any new module sold will help track the supply of potential new modules once at end of life, as First Solar are a significant producer of thin-film PV (another large producer being Hangery, who manufacture Cu(In,Ga)Se_2 modules) this is vital to maintaining their supply source in the future if indeed cadmium and tellurium supplies begin to dwindle. In the last few years interest has been turned toward the thin film I_2-II-IV-VI_4 quaternary compound semiconductor CZTS (Cu_2ZnSnS_4), containing relatively abundant precursor materials with low toxicity [27].

Multi-junction cells

Multi-junction solar cells attempt to utilize the majority of the solar spectrum by using multiple band-gap absorbers, typically in a monolithic architecture. By using multiple varying band gap absorbers in a multiple junction device, the maximum efficiency is no longer limited to 31 % by the Shockley-Queisser limit. Several tandem cells have been created, of which the highest recorded efficiency of 38.8 % belongs to the stacked 5J GaAs/InP device [28]. These high performance devices require the intricate deposition of several layers, the addition of additional steps in any industrial process introduces a higher probability of errors. This makes high performance devices expensive and not in a position to challenge the PV market. The ability to generate

a higher voltage and current does, however, place them into a more niche market. Space stations, satellites and probes can make use of these devices when the need for a reliable long-term, relatively light and compact power source warrants the high cost.

In order to make triple junction cells more cost effective relative to their single junction counterparts, concentrators have been used to increase their performance through the use of optic lenses. This relationship can be interpreted from the Shockley Diode law, where increasing the illumination power will lead to a higher short circuit current density [29]. Under 364 Suns intensity a triple junction solar cell has reached an impressive efficiency of 44.4 %, over one and a half times more efficient than a crystalline silicon cell [30]. Low cost tandem devices have also been reported, using low cost photo-absorbers in an attempt to bring down the price, whilst delivering a higher performance over their single junction counterparts [31]. These low cost devices are directly relevant to this project and are discussed in more detail in the next chapter.

Emerging PV technologies

A new series of technologies based on organic and excitonic solar cells, has seen a growing number of publications in the last decade. The more famous of these excitonic devices being the Dye-sensitised Solar Cell (DSC); the culmination of improvements to photo electrochemical cells previously using flat semiconductor surfaces [32]. Typically the accepted benchmark for reproducible cells is set at an efficiency of 10 % [33], with emerging research cells beginning to deliver efficiencies between 11-13 % [34]. The main focus of excitonic cells has so far been to deliver a working cell with as low a production cost as possible with an efficiency close to 10 %. Exploitation of fabrication techniques requiring a low start up capital, use of abundant low-toxicity materials which are already supplied in industrial manufacturing and simple to use techniques has seen the field of DSCs grow at an incredible rate [35]. Other excitonic cells such as quantum dots (QDs) and organic PV (OPV) have seen less attention due to their lower efficiencies compared to DSCs.

More recently there has been a surge in research towards perovskite solar cells. These devices were first based on the DSC architecture, using a perovskite organic-inorganic metal halide as the sensitiser [36]. These initial devices, whilst not comparable in performance to champion DSCs, were superior in performance to other QD and inorganic sensitisers. A breakthrough in replacing the TiO_2 layer with Al_2O_3 and the hole conducting electrolyte with the solid state spiro-OMeTAD, led to devices with over 10 % [37]. The considerable amount of research into DSCs and infrastructure has enabled this technology to rapidy approach effiencies beyond 20 %, in a short space of time that no other PV technology has witnessed.

1.4 Scope of Thesis

Multi-junction solar cells have already demonstrated their ability to deliver superior performance over their single junction counterparts. With this increased performance also comes an increased cost, leaving them only to be used in niche applications. It may be possible through the use of multiple low-cost emerging PV technologies in a multi-junction device, to produce a device capable of competing with the dominating silicon solar cell at a lower cost.

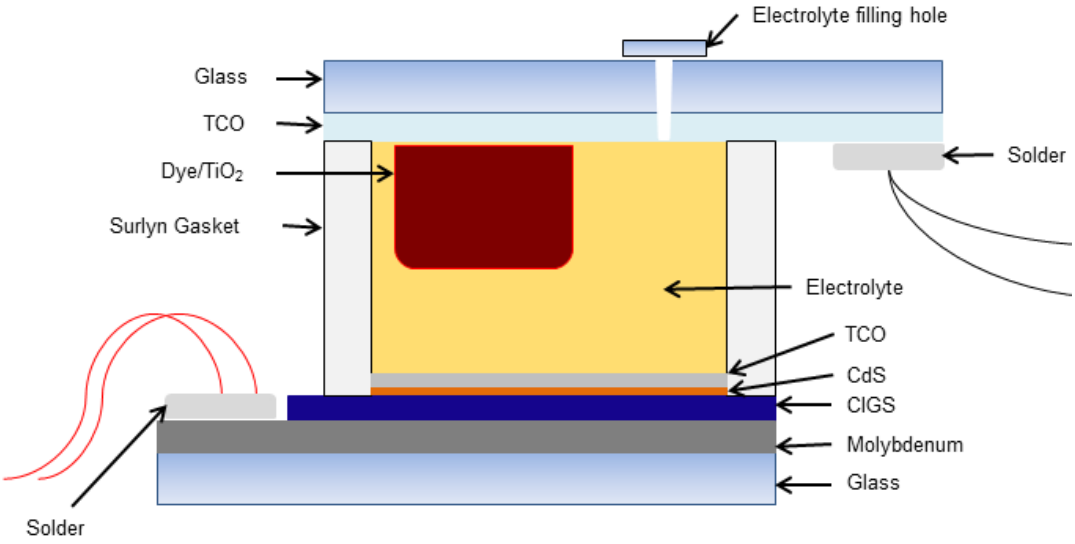

Figure 1.8: A schematic cross section of the monolithic DSC/Cu(In,Ga)Se_2 tandem solar cell described and fabricated in this thesis.

This thesis explores the combination of a dye-sensitised solar cell (DSC) and Cu(In,Ga)Se_2 solar cell (CIGS) in a tandem, monolithic design, a schematic of which can be seen in Figure 1.8. This monolithic design is an attempt to remove superfluous material from the physically stacked tandem, ultimately reducing the cost and increasing the performance. Chapter 4 elaborates on the materials needed to produce transparent contacts needed on the top of each absorber layer, to collect current generated by the device. It is split into two parts, the first on the high mobility transparent conducting oxide (HMTCO), titanium-doped indium oxide (ITiO). The second part focuses on the developments of the amorphous TCO, zinc oxide-doped indium oxide (IZO) which can be deposited at low temperatures whilst delivering comparable performance to TCOs used in mainstream solar cells. Chapter 5 investigates the monolithic design of the DSC/CIGS tandem cell and the importance of the cell architecture on performance when measuring under cell testing conditions. In order to accurately measure a solar cell, the area of the device must be accurately known, which can be difficult with a DSC. As a result the device is masked, but in a tandem cell this can affect the performance of the second cell, leading to overall current and voltage loss. The issues with corrosion in this type of tandem cell are also investigated in chapter 6 in an attempt to reduce the time taken to render the solar

cell inert due to the corrosive electrolyte used in the DSC. Apart from chapters 4 to 6 which represent the hands on experimental studies, chapter 7 provides the analysis of the DSC/CIGS tandem solar cell stack for the first time to analyse the overall impact on the device with the variation of different layers used in the tandem stack.

Chapter 2

LOW COST ABSORBERS FOR USE IN TANDEM SOLAR CELLS

2.1 Introduction

Multi-junction solar cells offer an opportunity to harvest and utilise more sunlight acting upon a fixed area, ultimately improving the efficiency of the overall device. They have seen a particular niche in powering extra-terrestrial satellites, where the weight and space requirements for a rockets launch need to be minimised. A satellite such as the International Space Station requires a stable and reliable power source capable of supplying a large power load for the extensive laboratories on board. The type of solar cell used in these applications, InGaP/GaAs/InGaAs, represents the pinnacle of solar cell efficiency but is reflected in their cost. With the best efficiency often comes the highest cost, resulting in a strong limitation for both large scale commercial and residential deployment. As a result InGaP/GaAs/InGaAs devices look to only fulfil niche applications where money isn't a problem, but power generation in a small area is. The cost of these multi-junction devices is primarily derived from the complicated fabrication process used, where several different layers (up to 20) are deposited by vacuum processes. An example of a resultant device can be seen in Figure 2.1 [38]. The efficiency limitation of a solar cell to only capture a range of visible light due to the band-gap of the absorber can be overcome through the use of a multiple absorber layer device, with each absorber band-gap chosen to absorb different ranges of the visible spectrum. Parallel to the high efficiency InGaP/GaAs/InGaAs solar cells, many devices have been presented using two absorber layers to boost performance, using absorbers that on their own are not considered suitable for industrial application.

It has been shown that the combination of two cheaper established technologies into a tandem configured device is able to challenge the efficiencies set by single junction devices [31]. This particular device was comprised of two separate absorber materials, a dye-sensitised solar cell (DSC) and Cu(In,Ga)Se_2 (CIGS) solar cell. Each cell absorbs separate parts of the spectrum, the DSC - blue and CIGS - red/near-IR.

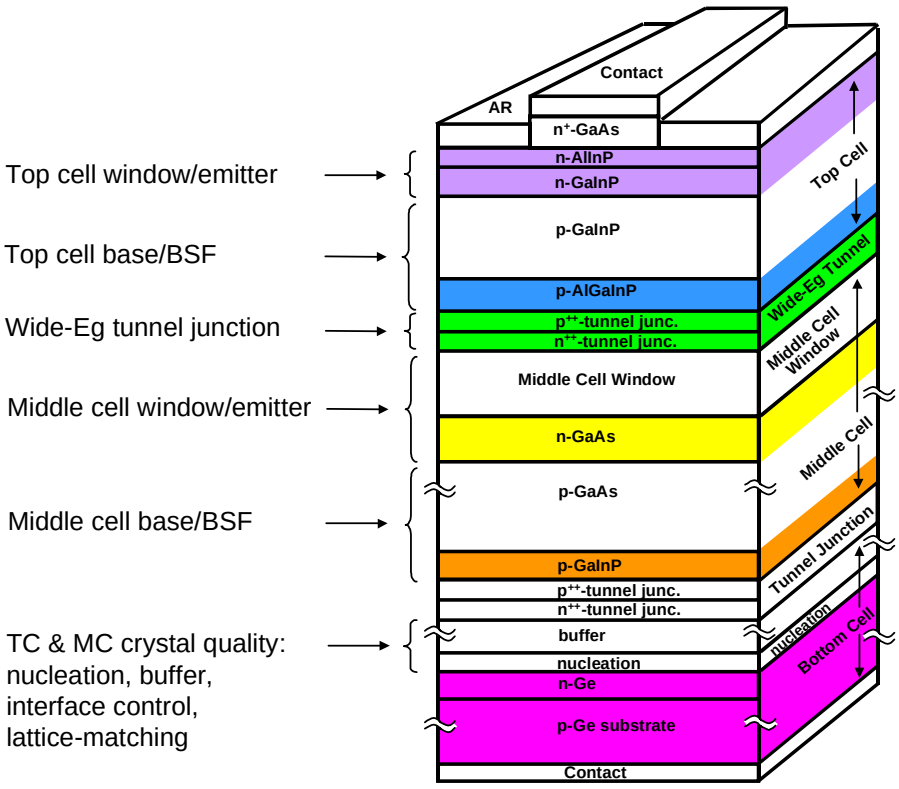

Figure 2.1: A visual description of each layer in the InGaP/GaAs/InGaAs III-V multijunction stack. Reproduced from [38].

The CIGS absorber layer used in this tandem device was produced using a vacuum process with a lower efficiency than that which is now currently achievable with the same process. Typically vacuum processes (sputtering, evaporation, closed space sublimation etc.) are able to produce an absorber layer of a superior quality than non-vacuum techniques (spray pyrolysis, inkjet printing, electro-deposition etc.) for use in solar cells. Since the publication of the seminal paper on the DSC/CIGS tandem cell, it is possible to deposit the CIGS layer through the use of non-vacuum methods to the same efficiency. This could potentially reduce the cost of making devices with a potential 15 % efficiency. In addition, the recent advances in excitonic solar cells and the increasing efficiency of non-vacuum deposited CIGS could in theory deliver cells with efficiencies over 20 %.

Optimising the optical and electrical parameters of both absorber layers is an important consideration to improve the efficiency of this tandem solar cell. For example, high efficiency DSCs require a scattering layer in order to enhance absorption in the near-IR. This layer must be removed for use in a tandem device, but causes a reduction in current and therefore performance for the tandem configured device. Other optical losses may occur in the device, such as the choice of transparent conducting oxide (TCO); typically the fluorine-doped tin oxide used in DSCs absorbs in the near-IR and as a result would reduce the performance of the CIGS absorber in a tandem device. This chapter describes the absorber layers in detail, to understand how they must be modified for use in a low cost tandem solar cell.

2.2 The Dye-Sensitised Solar Cell

The dye-sensitised solar cell (or DSC) is a photo-electrochemical cell able to achieve efficiencies over 10%, whilst being comprised of abundant materials. The DSC is different from most typical photovoltaic devices in that it is not a p-n junction. The main difference is that in a DSC the electron-hole pair is generated from a photosensitive dye, which is then injected into an n-type mesoporous scaffold, deposited on the transparent conducting oxide (TCO) front contact. In 1991 O'Regan and Grätzelpresented a breakthrough in photo-electrochemical cells, which were able to achieve a much higher efficiency of 7% compared to 1% of other photo-electrochemical cells of the time [32].

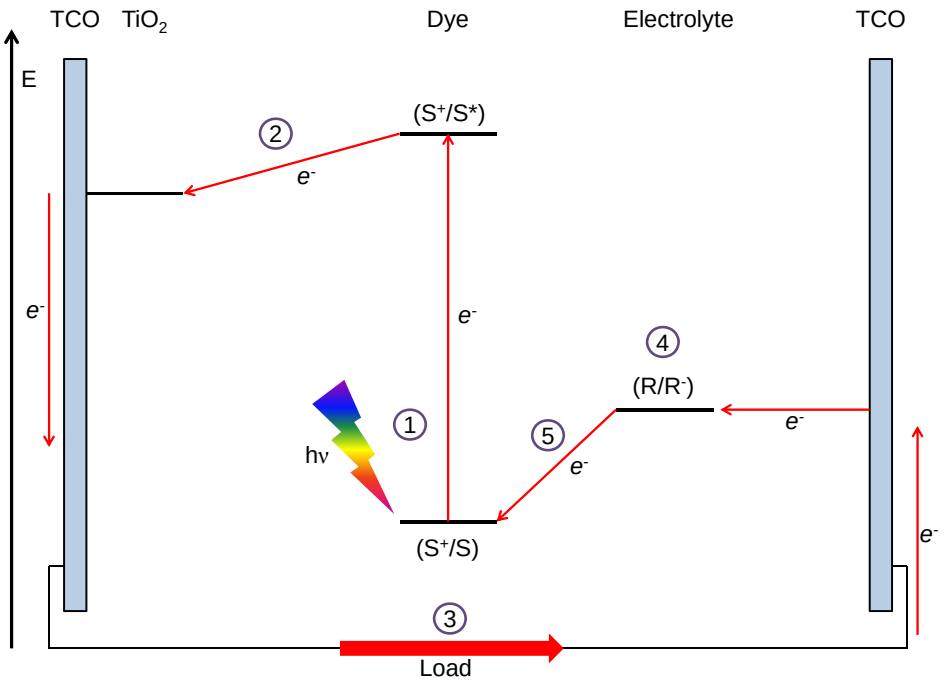

Figure 2.2: A simplified electron energy level schematic describing the conversion of photons to electrical energy in a dye-sensitised solar cell. Adapted from [32].

The process in which the DSC converts light to electrical energy can be seen in Figure 2.2. A summary of the stages involves are as follows: A mesoporous wide band gap semiconductor (commonly TiO_2) is deposited onto a TCO, and then sensitised by a molecular dye with a broad absorption and high molar extinction coefficient. The dye will absorb photons over a wavelength unique to the dye used (1), promoting an electron from the Highest Occupied Molecular Orbital (HOMO) to the Lowest Unoccupied Molecular Orbital (LUMO); the excited electron is then injected into the semiconductor layer (2). These photo-generated electrons then leave the cell through a TCO, perform work in a circuit and return in a completed circuit to the counter electrode (3). A hole conducting redox electrolyte lies between the working

electrode and counter electrode, electrons flow from the counter electrode through the electrolyte (4) back to the oxidised dye in order to regenerate it (5).

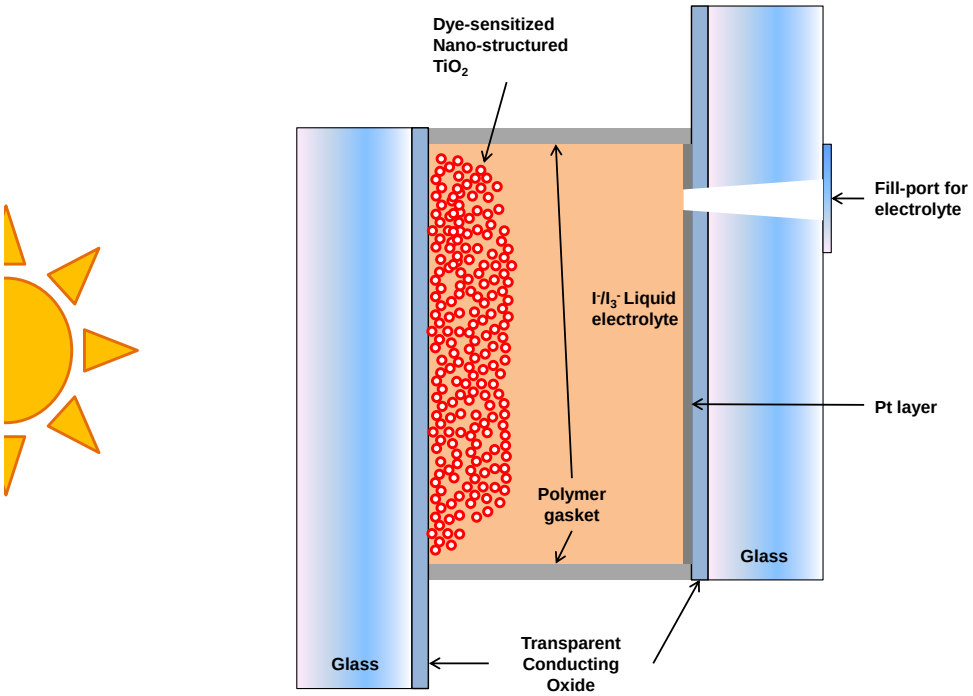

Figure 2.3: A schematic cross section of a typical dye-sensitised solar cell.

2.2.1 Fabrication and Performance

The popularity of research into dye-sensitised solar cells can, in part, be attributed to their relative simplicity of fabrication. Using well established hands on techniques such as doctor blading and screen printing, devices can potentially be made in a matter of hours. The ultimate advantage of these techniques though is the ability to scale up to a commercial sized output, without requiring as large a capital investment as other technologies such as silicon and Cu(In,Ga)Se_2.

The performance of the DSC can be altered by many parameters but it is particularly reliant upon the quality of the mesoporous TiO_2 layer. In this instance the quality refers to the ability of the TiO_2 to exhibit desired electron transport and low recombination rates, which are affected by the presence of trap states in the TiO_2 bandgap [39]. Transport of electrons to the front contact, injected from the photo-sensitising dye, occurs through the mesoporous TiO_2 by trapping and detrapping of the injected electrons [40]. More TiO_2 trap states will increase the time taken for injected electrons to reach the anode for collection, thus decreasing the performance of the device. Debate still rises on the nature of these trap states and the precise relevance of the TiO_2 structure on their prevalence [35]. However despite these trap states and their relationship with the semiconductor and the DSC perfor-

mance, there are other performance limiting factors that can arise from changes in the semiconductor structure.

The thickness of the TiO_2 layer directly affects the amount of current collected from the DSC. Up to a limit, increasing the TiO_2 thickness decreases the resistance of electron transport in the TiO_2/dye/electrolyte interface. As a result this increases the electron lifetime and the efficiency of a DSC. Increasing the thickness past the considered optimum thickness of 20 μm begins to decrease the performance by an enhanced recombination effect [41].

Currently the highest certified efficiency for a DSC is 11.9 %, which uses a highly optimised dye and electrolyte [9],[42]. Whilst this is a strong achievement for these cells, record breaking cells are typically hand picked to deliver a high efficiency for certification. Being able to replicate the fabrication of research scale DSCs with an efficiency of 10 %, is considered to be a benchmark amongst researchers in the field. Through the use of several well researched and understood materials this should be possible for most laboratories, although the use of a screen printer to deposit the TiO_2 layer gives better control of the thickness rather than doctor-blading [33].

Like most PV devices the DSC is characterised using a solar simulator with a spectrum closely matched to AM1.5G. Whilst the precise nature of the measurements of PV devices are covered in the next chapter it is important to mention the importance of masking DSCs whilst measured in a solar simulator. The active area of a solar cell is an important variable when calculating the efficiency of a solar cell. Most thin film technologies have this area defined using a machine that mechanically scribes the absorber layers in order to electronically isolate each individual cell. This process also accurately defines the cell area, which may then be used to ascertain the cell efficiency. The active area of a DSC is defined by the area of the screen printer mesh or by the spacers used in doctor blading, of which neither is an accurate indication of the area, as the paste is prone to relaxing and spreading out during fabrication. This means that it is possible to either over or underestimate the actual area of the absorber layer, leading to inaccurate efficiency calculations. Reflective enhancements are also expected dependant upon the thickness of the glass used in the device. To eliminate inaccuracy from measurements, a blackened metal mask is applied to the top of the device, with an aperture of a predetermined size. The device is also masked using tape around all sides of the device to stop reflective enhancements. A study on the findings of these inaccuracies and their effects on device performance can be found elsewhere [43].

2.2.2 Working Electrode

The choice of semiconductor in most DSCs is typically TiO_2, as so far this has lead to devices with the highest efficiency. Other similar semiconducting materials such as ZnO, SnO_2 and Nb_2O_5 have been explored [35]. TiO_2 will be the semiconductor used

and discussed in this thesis, although a more thorough of these alternatives, ZnO is better covered elsewhere [44].

In order to produce a high efficiency DSC, the TiO_2 layer must have a large surface area. A larger surface area will increase the amount of dye adsorbed, giving a much larger photocurrent due to more efficient light absorption. The TiO_2 layer is typically comprised of 3 different layers: a compact layer, a transparent layer and a light scattering layer. These different layers are each optimised to enhance the performance of the DSC and are deposited sequentially. The TiO_2 working electrode is commonly deposited on to commercially available Pilkington TEC™. This TEC glass is soda lime glass with a layer of fluorine-doped tin oxide (FTO) deposited on top, the sheet resistance of the layer given by the product name (TEC8 is 8 $\Omega/\square$ and TEC15 is 15 $\Omega/\square$). This FTO layer is transparent in the same range as the DSC once sensitised, the surface is rough which enhances the adhesion of the TiO_2 to the surface, it has a good conductivity and it is chemically and thermally stable.

The first step in fabricating the DSC working electrode is to immerse the substrate into a $TiCl_4$ solution at 70 °C both before and after the application of the transparent and light scattering TiO_2 layers. This step has been shown to increase the photocurrent collection by 10 - 30 % [45]. The application of the next layer, the transparent TiO_2 layer is carried out either by the deposition of a paste by doctor blading or screen printing, typically to a thickness of 12 μm. Whilst this paste can be purchased commercially by companies such as Solaronix or DyeSol, they have a similar composition to pastes previously reported. The typical composition of a transparent TiO_2 paste contains a colloidal suspension of 10-25 nm anatase TiO_2 particles with a carbon containing binding agent, such as ethylcellulose or polyethylene glycol, this gives the paste a suitable rheology for both deposition methods [46]. The third and final layer, the light scattering layer, is applied directly on top of the transparent layer. This is similar in content to the transparent except the TiO_2 particles are much larger in size, typically around 400 nm. This layer comprised of the larger TiO_2 molecules causes an enhanced absorption of light in the near-infrared, acting as a photon trapping system and demonstrating photovoltaic properties [33]. The substrate is fired to 450 °C whilst holding at lower temperatures before ramping up. This causes the burning of the carbon containing binders, initially turning the TiO_2 electrode brown, but finally turns a bright white as the binder is fully decomposed and burnt away. The absence of the binder material after thermal decomposition helps to form the porous nano-structured TiO_2 layer. The substrate then undergoes the second $TiCl_4$ treatment described previously and is then sintered at 500 °C to leave a high quality TiO_2 working electrode, ready for sensitising by the dye.

Electrodes formed from using these pastes to form the porous nano-structure have so far delivered the most efficient devices to date, however a series of other TiO_2 nanostructures such as nano-rods [47], nano-wires [48] and nanotubes [49] have been presented. With these increased knowledge and improved techniques in nanotechnology,

research groups have attempted to emulate the success of the 1991 nature paper with the intention of increasing the surface area of the TiO_2 working electrode. It has been postulated that reducing the distance an electron has to travel through the ZnO/TiO_2 semiconductor will lead to more efficient charge separation and performance. By producing a highly ordered single crystal of TiO_2 it is hoped that the electron diffusion length will be increased, without the loss of the large surface area afforded by a mesoporous structure. These assemblies are grown directly on the TCO and have a short, vertical path for current flow. Theoretically once an electron is generated it may travel directly unhindered to the TCO contact, not through a series of trapping and detrapping states.

2.2.3 Sensitising Molecules

Several different types of inorganic and organic photo-reactive dyes exist for use in DSCs, which can in each case, be further categorised. The dye used in the DSC must be able to absorb a broad range of visible light, in order to maximise the current density of the device. Some dyes have a very specific and/or narrow absorption region in visible light and as a result do not perform as well compared to those that are able to absorb more light. Infra-red absorption is also possible from some dyes, especially when used with a light scattering TiO_2 layer, this can potentially increase the current density of a DSC even further. Given the maximum thickness limitation of the semiconductor layer, mentioned earlier, it is vital too that the dye have a relatively large molar extinction coefficient, ε. This is in relation to the Beer-Lambert law where A is the Absorption, c is the concentration in mol.dm^{-3} and l is the path length.

$$A = \varepsilon\ cl \tag{2.1}$$

By maximising this value, it is possible for the dye to more efficiently absorb incident photons in relation to the available surface area of the absorber layer. Tailoring of the dye structure by the addition of certain functional groups and chromophores will influence the molar extinction coefficient and will be explained in more detail later in this section. The structure is not only important to the function of the dyes ability to absorb light, but how well the dye adsorbs to the semiconductor layer and how efficiently it injects electrons generated from the dye into the semiconductor layer. The use of different functional groups such as H_2PO_3, -SO_3H and -COOH have been studied in detail, with the carboxyl group -COOH more frequently used due to its stability, easier synthetic procedure and efficient electron charge injection into the TiO_2[35].

Finally the dye must have very particular electronic properties in order to function correctly in a solar cell. As seen in previously in Figure 2.2 the energy levels of the dye must be tailored to both the working electrode and redox couple electrolyte. The

ground state of the dye (HOMO) must be lower than the energy level of the TiO_2 and the excited state (LUMO) above it, such that the electrons produced can be favourably injected into the semiconductor layer. For regeneration of the oxidised dye following charge generation and extraction of the electron-hole pair, the dye must have a more positive redox potential than that of the electrolyte.

Dyes

Inorganic ruthenium complexes are amongst the most common and successful dyes employed in DSCs. This is somewhat of an oddity due to their relatively low extinction co-efficient and long term instability when used with a tri-iodide redox electrolyte (covered later). N719, N3 and Z907, each seen in Figure 2.4, are perhaps the most common ruthenium dyes, each incorporating NCS thiocyanate ligands [50].

Metal complex dyes (including Ru dyes) rely on the metal to ligand charge transfer (MLCT) for absorption of visible light photons, where an absorbed photon causes the transfer of an electron from the metal d orbitals to the ligand π^* orbitals [51]. This excited state electron is then injected into the conduction band of the TiO_2 semiconductor. Through modification of the ligands chosen it is possible to modify the HOMO and LUMO levels of the dye. The ruthenium sensitiser N749 or black dye demonstrates a wider absorption by the inclusion of an additional thiocyanate ligand and a tridentate terpyridine ligand [52]. This addition red-shifts the absorption compared to that of the common N719 and N3 dye by decreasing the energy of the π^* orbital and increasing the Ru t_{2g} metal orbital. Modifications to the energy levels of Ru dyes and their effects to device performance have been well documented [51].

Thiocyanate ligands give the dye the benefit of a broad absorption spectrum through tuning of the dye energy levels, but also react over time with the tri-iodide electrolyte, rendering the dye inactive [53]. Interesting findings have resulted in an attempt to stem this reaction, by using the chelate effect to develop new bi-dentate ligands; these ligands are promising but require more optimisation in order to broaden their absorption spectra [54].

Other types of dye exist which take advantage of different electron generation mechanisms. These dye types include porphyrins [34][55], phthalocyanins [56] and organic dyes [57].

Perovskites (Meso-superstructured solar cells)

Perovskite solar cells have recently changed the direction of research into excitonic solar cells thanks to a breakthrough in solid state devices. The use of a organometal halide material with the perovskite structure, ABX_3, has led to some rapid advances in device efficiencies in the last few years. It has been demonstrated as a quantum dot sensitiser on a TiO_2 meso-porous layer, with early devices delivering a thin absorber layer with a respectable efficiency of 6.5 % due to a larger extinction co-efficient than

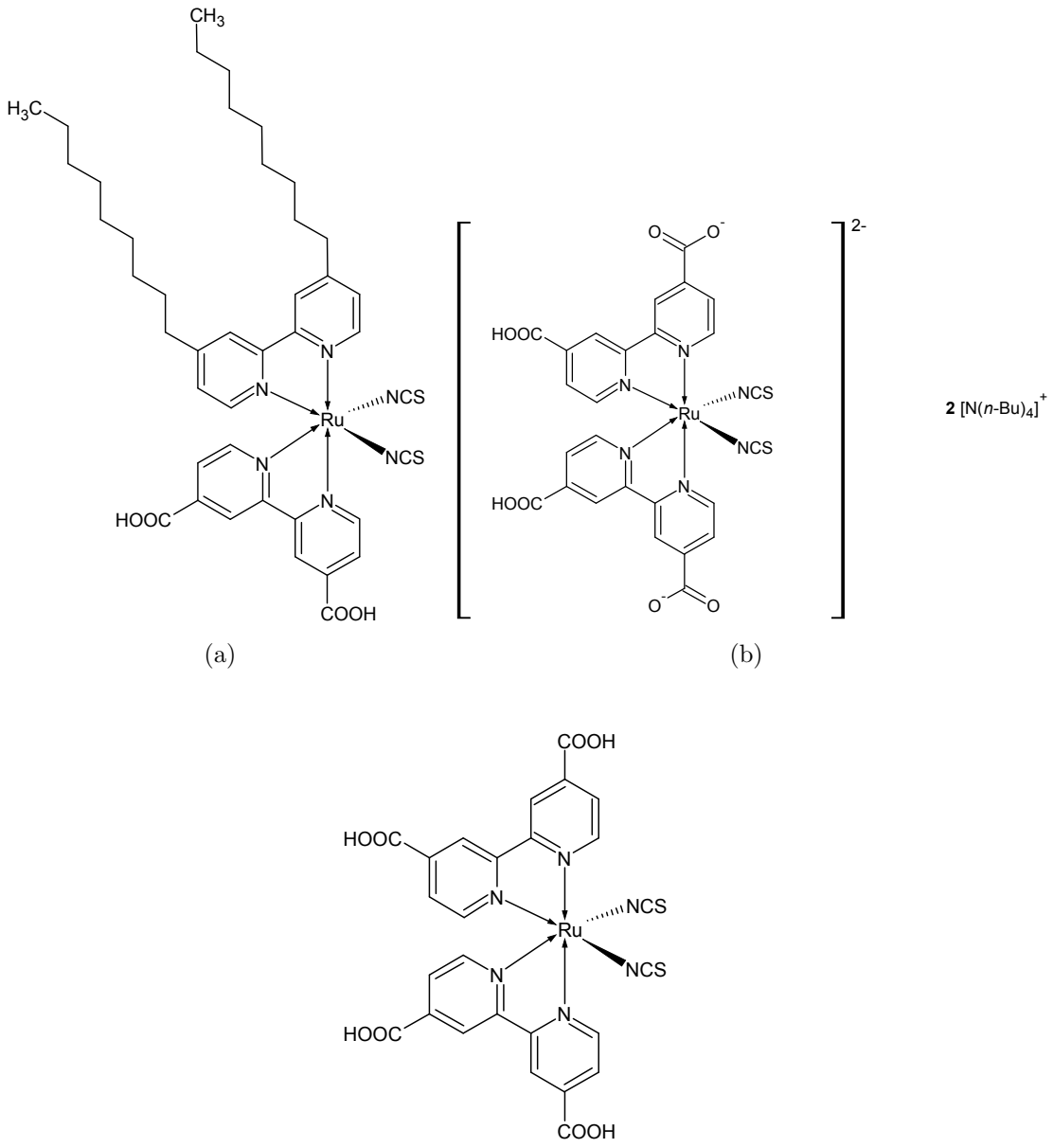

Figure 2.4: Three commonly used ruthenium based photosensitisers, (a) Z907, (b) N719 and (c) N3.

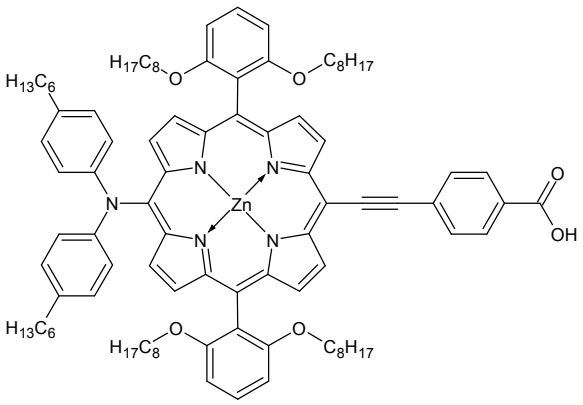

Figure 2.5: The porphyrin based dye, YD2-o-C8, capable of efficiencies over 10 %.

the N719 dye. These devices bested the champion QD devices, but suffered from rapid deterioration of the absorber layer as it dissolved into the liquid electrolyte [58]. The realisation that the electron transport properties of the perovskite were, in fact, superior than TiO_2 bought about a change in device architecture and with it, an efficiency of 10.9 % [37]. The use of an insulting Al_2O_3 scaffold as opposed to TiO_2 ensured that the photo-generated electrons were not injected into the metal oxide layer, but transported through the perovskite absorber. This change resulted in a V_{oc} over 1 V and a J_{sc} similar to that of a high efficiency DSC. With the Al_2O_3 layer not contributing to the electron transport or electronic parameters and only acting as a scaffold, the devices are referred to meso-superstructured solar cells (MSSCs). The inclusion of a solid state hole conductor, spiro-OMeTAD, due to the low thickness of the absorber layer (3-4 μm) eliminates the risk of dissolving the absorber layer, it also solves one of the primary setbacks with DSC research in not having to use a liquid electrolyte. However in order to stop shunting pathways in the device between the absorber and Ag back contact, a thick layer of spiro-OMeTAD is used. This demonstration of a solution processed, solid state device from low-cost precursors has caused a sharp increase in research undertaken in this field. Currently the world record for a thin film perovskite has surpassed 20 %.

Of particular interest to tandem solar cells is the inverted cell design, where by the regular design akin to the DSC is changed such that the perovskite cell may be incorporated into a tandem design as the top absorber [59]. The EQE of a perovskite cell has a similar absorption onset as a DSC, but has the advantage of being a solid state design, which would be much more preferred in a tandem solar cell. With a similar current also, but a larger voltage it can be expected that a tandem cell designed with an inverted MSSC/CIGS absorber configuration should yield promising results despite the absorber overlap.

2.2.4 Hole Conducting Electrolyte

For the DSC to work correctly a hole conducting material must be applied between the dye-sensitised TiO_2 and the counter electrode in order to regenerate the oxidised dye. This is accomplished through the use of an iodide/tri-iodide redox couple, although other redox electrolytes have been used such as the cobalt (II/III) electrolyte [60]. The I^-/I_3^- electrolyte is the most successful electrolyte in terms of frequency of use in research, due to its simplicity to make, slow recombination and compatibility with Ru based dyes in high efficiency DSCs. The I^-/I_3^- mechanism works such that the electrons from the counter electrode are transferred to regenerate the oxidised dye by the I^- ion, upon which the iodide ion is oxidised to an I_3^- ion, which is then reduced after diffusion to the surface of the platinum coated counter electrode. The iodide redox couple is typically comprised of elemental iodine and an iodide salt. The addition of inorganic iodide salts such as LiI or organic imidazolium salts enable the

enhancement of photocurrent in the device, through enhanced electron separation and injection, at the cost of the DSC V_{oc}. Specifically with regards to lithium, the adsorption of Li^+ to the TiO_2 layer increases the injection efficiency of electrons into the semiconductor caused by a reduction in energy level of the conduction band [61]. This reduction of the conduction band level in turn leads to a reduction in the Fermi level and the V_{oc}, which therefore requires careful optimisation to enhance the efficiency of the device. Smaller cations such as Li^+ have a more pronounced effect in altering these electronic properties, over larger cations such as Rb^+. In tandem with cation additives, 4-tert-butylpyridine is combined in the electrolyte as it also adsorbs to the semiconductor to modify the conduction band, increasing the energy of the TiO_2 conduction band, but is able to reduce recombination losses between the TiO_2 and I_3^- ions. As a result these two additives are used in a complimentary composition to maintain a sufficient voltage, whilst delivering a slightly larger J_{sc} due to faster electron injection times [62]. Finally to improve the photocurrent of the device, to achieve efficiencies either approaching or surpassing 10 % guanidinium thiocyanate is added into the electrolyte by impeding surface recombination [63].

In basic laboratory cells the solvent is typically a mixture of valeronitrile and acetonitrile, where long term stability is not a concern. The solvent must readily dissolve the electrolyte components, but not the adsorbed dye and have a sufficiently low viscosity to enable filling of the DSC device with the electrolyte. For long term stability this electrolyte must be able to resist leaking/evaporation out of the sealed device and not chemically attack the gasket of the DSC. Due to the volatility of these solvents a move toward the use of 3-methoxypropionitrile (MPN) was taken, improving the stability of DSCs under long term illumination [64]. Solidification of the electrolyte in-situ after filling the DSC was identified as a convenient way to prevent device leaking. This was accomplished through the use of ionic liquids, comprised of imadazolium salts such as 1-propyl-3-methylimidazolium iodide (PMII). Despite their relatively high viscosity to organic solvents, they are able to be used in DSCs and do not suffer the mass transport issues believed to occur in high viscosity electrolytes, due to the increased diffusion coefficient of the tri-iodide ions [65]. The use of eutectic melts comprised of high melting point imidazolium salts was employed to deliver a solvent free electrolyte with a high conductivity. This demonstrated that the mixture of normally solid imidazolium salts at room temperature in a mixture would demonstrate a higher conductivity than pure PMII whilst having a melting point below 0 °C, enabling filling of a DSC. The increase in conductivity was attributed to the enhanced fluidity, increased ion concentration and smaller cation sizes in the melt whilst delivering a respectable DSC efficiency of 8.2 % [66].

Solid state hole conductors

As has been highlighted liquid electrolyte DSCs deliver the highest device efficiencies when compared to quasi-solid state DSCs, such as the eutectic melt electrolytes. Despite the low cost of DSCs and the vast improvements in increasing the stability of the dye/TiO_2 component, the stability of the electrolyte with regards to sealing is still a concern prohibiting large scale commercial deployment. Solid state hole conducting polymers, such as spiro-OMeTAD, may be employed to replace the traditional liquid electrolyte, however initial devices suffered from lower efficiencies (<1 %) when compared to the liquid or quasi-solid state DSCs [67]. Identification of the low efficiencies due to interfacial charge recombination losses between the TiO_2 and hole conductor, led to the addition of additives similar to the liquid electrolyte, to reduce these losses and significantly boost the efficiency (2.5 %) [68]. The main impedance to higher solid-state device efficiencies is the thickness limitation of the TiO_2 layer and the inability to use light scattering layers for the dyes. The thickness is restricted due to the need to effectively fill the pores with the hole conductor, as it is typically spin coated onto the TiO_2/dye stack. Unfortunately the ruthenium based dyes used most commonly in liquid based DSCs have a relatively low molar extinction co-efficient and are not well suited in thin layers, only reaching a maximum efficiency of 5.1 % in solid state DSCs [69].

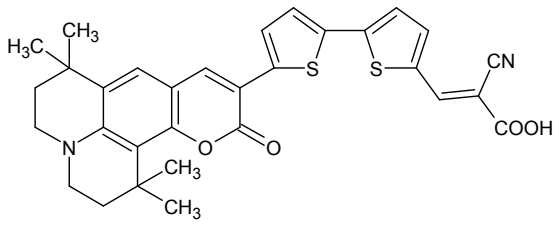

Figure 2.6: A coumarin based dye, NKX-2677, able to demonstrate a high efficiency of 6 % in a solid state DSC [57].

Theoretically an increase in molar extinction co-efficient would lead to a greater absorption of photons in a more compact layer, such as those used for solid-state DSCs. As a results a series of dyes were employed which demonstrated this trait, with a value several times higher than Ru based dyes, such as coumarin which can be seen in Figure 2.6 [57]. Not only are these dyes able to surpass the efficiency of Ru based solid-state DSCs, they are cheaper to produce due to the absence of expensive metals needed for the MLCT process. These dyes may be an attractive inclusion into a tandem device due to their thin layers, which would potentially increase light to a bottom absorber.

2.3 Cu(In,Ga)Se_2 Solar Cells

Copper indium gallium diselenide, Cu(In,Ga)Se_2 (or CIGS) solar cells currently offer the highest performance of all thin film technologies, with a record efficiency close to 22 %. They are an ideal co-absorber with DSCs due to their absorption of light in the red to near-infrared range. Similarly to DSCs the properties of the CIGS absorber can be modified to better suit operation in a tandem device.

It was predicted that CIGS devices would eventually out-compete c-Si in the PV market, but uncertainties concerning the world's indium supply can present a problem when increasing the manufacturing output of CIGS panels. Indium mining does not occur directly and is processed as a by product of zinc mining, essentially binding indium supply with the demand of zinc. The opto-electronic industry consumes nearly five times the amount of indium than the PV sector, wasting almost 80% of indium in the coating of glass when making TCO contacts [70]. With the sharp price increase of indium to over $1000/kg in 2006 from $400/kg in 2004, the opto-electronic industry moved to increase their supply by recycling indium from end of life products [70]. It has been predicted that assuming the manufacture of 19% efficient CIGS panels using the remainder of the worlds indium supply, that CIGS would only be able to provide 0.02 TWy of power [71]. This is compared to the silver shortage of silicon cells, however they would be able to contribute 2.5 TWy of power from known reserves; whist it would also be possible to develop new electrodes using more abundant resources. This would not be the case in CIGS absorbers as indium is a key material in the absorber layer and may not simply be replaced. Future exploitation of indium sources in the United States and Australia hope to alleviate the current pricing of current indium sources. It would appear that any manufacturer of CIGS would be wise to attempt recycling of end of life products, similar to First Solar and the opto-electronic industry.

2.3.1 Device Materials, Architecture and Performance

Cu(In,Ga)Se_2 is a quaternary I-III-VI chalcogenide based p-type semiconductor material with the chalcopyrite crystal structure (ABC_2), similar to the ternary chalcopyrite semiconductor CuIn(S,Se_2) (CIS). Through the substitution of indium atoms for gallium atoms it is possible to adjust the band gap from 1.0 eV for $CuInSe_2$ to 1.7 eV for $CuGaSe_2$. To achieve an ideal band gap of 1.4 eV, the adjustment of the composition to give Cu($In_{0.7}$, $Ga_{0.3}$)Se_2 has found to be successful [21].

This increase in band gap gives a higher V_{oc} and fill factor, leading to an overall more efficient device. Significant research into CIS solar cells prior to the common incorporation of gallium led to a comprehensive understanding of the phase chemistry of the Cu-In-Se system. The formation of the desired α-chalcopyrite CIS structure is somewhat of a challenge, with the ability to form many different phases from precursor compounds, seen in Figure 2.7 [72].

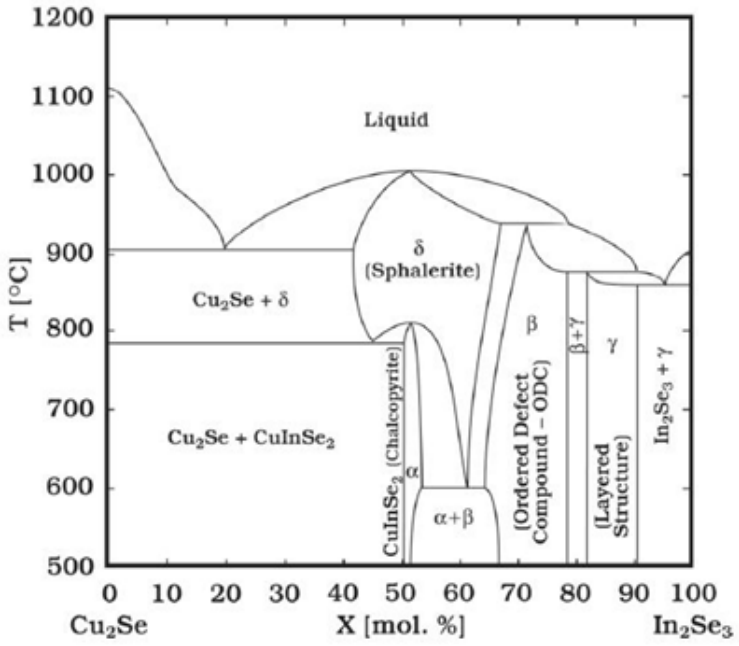

Figure 2.7: Cu-In-Se phase diagram depicting the possible phases from Cu, In and Se precursors. The desired α-phase is formed when indium and copper concentrations approach equivalence, given the correct temperature [72].

Modification of the CIS structure through the introduction of gallium to form CIGS serves to increase the performance of the absorber layer. Gallium incorporation also widens the α range in the Cu-In-Se phase diagram. This combined with doping of the CIS/CIGS layer with sodium, proved to also reduce the exsolution of the β phase for the conditions used to form absorber layers [73]. More importantly, relevant to tandem solar cells, it is possible to tune the absorption profile of the CIGS layer through alteration of the Ga concentration. An increased gallium concentration serves to reduce current whilst increasing V_{oc} [74]. This is of particular importance to tandem cells when considering current matching in the overall device. When a tandem solar cell is in a series configuration the absorber layers must be current matched, meaning they must have a similar photo-current. Although the current of the device is limited to the performance of the absorber with the worst current other issues may occur, such as excess heat generation, from current mismatching in a tandem solar cell.

Sodium doping the CIGS absorber can increase the conductivity by an order of magnitude and is a process implemented in all high efficiency CIGS devices [75]. The Na source has typically originated from the substrate used for the solar cell. Substrates such as soda-lime glass can provide a sufficient dopant concentration of 0.1 at% for an improvement in conductivity. If a Na source is present during the growth of the CIGS layer, the grain size is reduced relative to no sodium being present [76]. A reduction in grain size in theory reduces the performance in solar cells, as the grain boundaries become more frequent with a larger surface area. Whilst this is the case in nearly all crystalline solar cells, the improvement in electrical parameters from

the sodium incorporation makes up for the reduction in performance for the reduced grain size. The use of a post deposition treatment to incorporate Na into the film following deposition of the CIGS layer showed a reduced Na incorporation into the CIGS layer, compared to the diffusion from soda-lime glass. More importantly it was found that a post treatment to incorporate sodium into the film did not reduce the size of the grains in the absorber layer [77]. This is particularly useful when it is necessary to deposit devices onto substrates that do not contain sodium, such as the plastic substrates used for flexible solar cells.

The CIGS Solar Cell

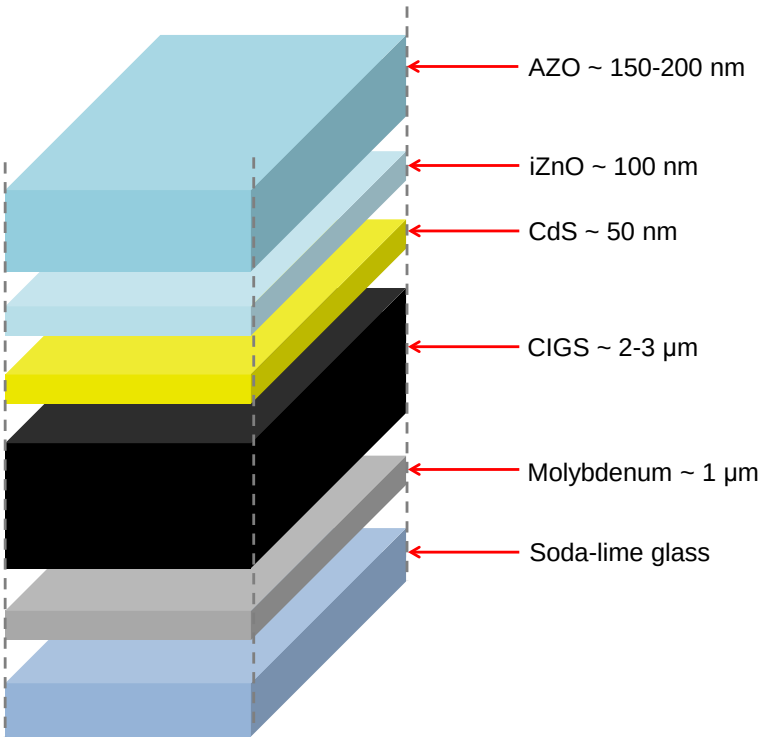

Figure 2.8: A collapsed view of the materials used and their typical thicknesses in a common CIGS solar cell.

The most typical configuration of a CIGS solar cell is that of a substrate and can be seen in Figure 2.8 and begins with the deposition of molybdenum as a back contact material onto soda-lime glass. Mo has a high stress on its crystal structure and has poor adhesion and as a result can de-laminate fairly easily from the substrate. To combat this poor adhesion a bi-layer of Mo is deposited, comprising of a first layer deposited at a higher working pressure and a second deposited at a lower pressure. Investigations into using Ag, Au, Cu, Mo and Pt have been conducted, concluding Mo to offer better stability at the temperatures used in CIGS processing steps. In addition it has been shown that the formation of $MoSe_x$ between the CIGS and Mo films enhances the electrical contact for holes and reduces electron recombination [78][79]. Next the CIGS photo-absorber is deposited, typically to a thickness of 2-3

microns. Many different methods exist to deposit the CIGS layer, which shall be summarised in more detail later. These methods mostly focus on forming a CuInGa precursor layer, with the most efficient devices using a 3 stage co-evaporation process. This precursor layer is then selenised in a nitrogen diluted Se vapour at low pressure, this process forms the quaternary CIGS layer. Once the CIGS film has been formed, a layer of n-type CdS is applied as a buffer layer by chemical bath deposition. This buffer protects the CIGS layer from chemical reactions, optimises band alignment and forms a depletion layer wide enough to minimize tunnelling. The band gap of CdS is 2.42 eV and although it is wide enough to ensure efficient transmission of photons to the CIGS layer, some losses are expected from a slight overlap of absorption spectra. Finally an intrinsic layer of zinc oxide and aluminium-doped zinc oxide are RF sputtered to finalise the p-n junction and act as the front contact.

2.3.2 Vacuum Deposition Methods

Currently the deposition of CIGS absorber layers by vacuum techniques has delivered the highest efficiency devices [13]. Fabrication of the highest efficiency CIGS devices currently requires the use of vacuum techniques. Deposition of materials in a vacuum, such as sputtering, ensures that no contamination from air, moisture and other particulates can contaminate the finished product. Sputtering in particular is a well used and established industrial process, used for several applications outside of the PV sector. Although this thesis is concerned with low cost processing of the absorber layers, vacuum deposited CIGS devices have been used to make higher performing tandem devices.

Co-evaporation

The 3 element source co-evaporation process has been used to great effect when depositing the CIGS absorber layer. It has been the most common vacuum technique currently used for depositing high efficiency CIGS since the early 90's, developed at NREL before being patented [80][81]. Through control of the flux of each evaporation source it is possible to produce compositional gradients for Ga/(Ga+In) relative to the thickness of the layer. This has a direct impact on the conduction band of the CIGS material, by raising the band edge. By increasing the Ga concentration at the back contact, the conduction band is higher in energy toward the back contact of the absorber, causing electrons to be pushed towards the depletion region and away from the back contact, reducing recombination losses and increasing current [80]. Some processes directly incorporate the selenium source into the process, whereas others make use of a post selenisation step. Elimination of the post evaporation selenisation step has been attempted though the use of selenium containing precursors during deposition, or in fact a single evaporation source containing a stoichiometric combination of Cu, In, Ga and Se [80][82].

Sputtering

Sputtering is an excellent technique for the deposition of thin films, able to produce more uniform and more dense films than those by evaporation. At an industrial level it is easier to scale up a sputtering process than an evaporation process, with films deposited from evaporation at a large area suffering from a lower deposition rate and poorer step coverage. Given the complexity of the 3-stage process commonly used in evaporation processes, the advantage of sputtering from a single metal tertiary target (with a post-deposition selenisation step) or chalcopyrite quaternary target to simplify fabrication of CIGS absorber layers has been demonstrated [83][84]. Although research devices made from these absorber layers have not achieved an efficiency greater than 10 %, cells with an efficiency of 17.2 % have been produced by sputtering commercially by Miasole [85][86]. These cells in a module currently hold the record efficiency for a CIGS module, demonstrating the potential for sputtering CIGS in industry [28].

2.3.3 Non-vacuum Deposition Methods

High performance CIGS cells are produced using relatively expensive vacuum processes, which coupled with scarce precursors can reduce the potential competition of CIGS with c-Si despite the reduction in material usage. In fashion with third generation approaches to low cost manufacturing alternatives, non-vacuum CIGS devices have been studied as alternative methods to deposit CIGS. These eliminate the need for high vacuum equipment and expensive precursors at the cost of performance. These non-vacuum fabrication techniques are of particular interest for use in proposed low-cost tandem devices.

Electrodeposition

The electrodeposition of PV absorber materials has been a popular research point, due to the low cost of equipment and the ability to scale up research processes to industrial outputs. This is no different with CIGS and many attempts have been made to deposit efficient layers through this process with industrial cell records reaching an efficiency of 15.9 % [86]. As with most low-cost processes electrodeposition of the highest efficiency layers typically involves electrodepositing a precursor film consisting of multiple Cu, In and Ga stacks with a post process selenisation step. This process is carried out in three separate reaction vessels, which could potentially reduce a commercial output rate. As a result a co-deposition of all three precursors would be preferable for industrial application. Co-deposition of all three metallic precursors together in a single electrodeposition to obtain a controlled Ga concentration is not as straight forward due to the negative potential of Ga. Successful attempts to co-deposit the metallic precursors with the desired Ga concentration has been demonstrated through control of the solution pH, but can require additional

reagents and leave structural defects not present in the multiple electrodepostion process (also leading to lower efficiencies) [87]. A change in the use of starting materials to form a metallic mixed oxide/hydroxide precursor film, followed with a reduction step by annealing in a hydrogen environment and then selenisation delivered a 12.4 % efficient electrodeposited solar cell [88]. This is a promising step forward for one-pot electrodeposition processes for CIGS layers, although the removal of the reduction step is a limiting factor for industrial application.

Metal Salt Solutions and Pastes

The use of metal salts, typically nitrides and/or chlorides, dissolved in a carbon binder is an approach similar to that used to form the mesoporous TiO_2 layer in DSCs. This approach took a precursor solution containing a desired composition of Cu, In and Ga and dissolved it into a solution of 1-pentanol and ethylcellulose. The finished paste has suitable properties for deposition onto a SLG/Mo substrate using a doctor blading process. The substrate is annealed to remove the organic binders, then selenised and the cell finished as with typical CIGS cells. This method produces cells with efficiencies around 6-8 % but they suffer a relatively high series resistance and low fill-factor due to the amorphous carbon layer, left from the burnt organic binders between the CIGS/Mo interface [89]. An improvement in reducing the thickness of this carbon layer to increase the device performance has been a focus of study. Using the same methodology but with replacement of the binding agent ethyl cellulose with a viscous chelating solvent led to an improvement in the device performance. 1,2-propanediol forms a metal-organic complex from the precursor metal salts to avoid unwanted side reactions prior to formation of the CIGS layer. When heated the solvent decomposes and evaporates more readily than the ethylcellulose, although a slight residual carbon layer is still observed. Devices from this methodology deliver a higher efficiency and an EQE profile more fitting to a vacuum deposited high efficiency CIGS device. It has been suggested that the selection of more thermally labile ligands could produce a more efficient decomposition of the precursor and further reduce the thickness of the carbon layer [90]. It has been shown that the post treatment annealing of the precursor layer in a sulphur and/or reducing environment can reduce the amorphous carbon layer and increase the grain size of the CIGS absorber [91].

The elimination of the selenisation step is often a goal to accomplish when fabricating CIGS cells via a low cost process, as this step can often require fine tuning to the process used to deposit the CIGS layer. The use of metal sulphides and/or selenides, such as Cu_2S, provide a potential chalcogen source without the need of a sulfurisation/selenisation step. This has been successful through the use of a hydrazine solvent [92]. The use of hydrazine also eliminates the inclusion of unwanted contaminants such as Cl, O or C from the binding materials described previously, as the precursors used are all present in the finished film. Films prepared using this

method are of a high quality with large monocrystalline grains. It should also be noted that despite a lack of a selenisation step, a $MoSe_2$ layer is still formed at the Mo/CIGS interface [93]. So far efficiencies have reached 15.2% which is an incredible achievement for a solution based process compared to ZSWs 20.8% record vacuum cell. In comparison the solution processed device had a slightly lower V_{oc}, J_{sc} and fill factor, but electronic losses from electron-hole pair recombination and lower minority carrier lifetime were believed to be the limiting factors to a comparable performance [94]. Despite these gains in efficiency the parameters required during deposition would be non-ideal for scaling up. The most notable concern is that hydrazine is a highly toxic, flammable liquid (and finds use in some rocket fuels). If another suitable solvent were to be found however the current process must be carried out in an inert atmosphere, which is not cost effective when scaled up. Spin coating used to produce these films is also a very wasteful method used to cast precursors on a substrate and is not considering for industrial use.

Chapter 3

EXPERIMENTAL METHODOLOGY

3.1 Magnetron Sputtering of TCOs

The most common deposition technique employed in industry to deposit TCOs is sputtering. This technique can deposit a thin film with excellent crystallinity with excellent reproducibility when compared with open-air techniques such as spray pyrolysis. Magnetron sputtering is a vacuum process where a desired material is deposited onto a substrate from a target source. This selected source material is bonded onto a copper backing plate (typically using indium) and is referred to as the target. An argon plasma is formed by a negatively biased electrode behind the target and confined above the target through the use of a magnetic field, from magnets positioned behind the target. Through electrostatic attraction the ionised argon atoms strike the target surface with a high energy, ejecting the target material. These ejected particles travel away from the target and towards the substrate as seen in Figure 3.1. Rotation of the substrate during the deposition ensures that a homogeneous thin film is deposited. The choice of power supply and type of target greatly affect the properties of TCOs deposited. When depositing TCOs it is possible to either deposit from a ceramic doped oxide target, or to co-sputter from two or more intrinsic oxide targets. As metal oxides, especially intrinsic oxides such as tin oxide, have a poor conductivity it can be difficult to maintain a plasma using a standard DC power supply (typically used when sputtering metals) and as such RF and pulsed DC powers supplies are alternatives designed to overcome this limitation.

During the course of this thesis only ceramic targets have been used to deposit all TCOs used, as they offer a more reproducible result than co-sputtering. Despite this, co-sputtering has the advantage of allowing control of the doping concentration during depositions, however the TCOs used in this project have been extensively documented to determine the optimum doping concentrations.

Sometimes it is necessary to reactively alter the composition of the TCO, through

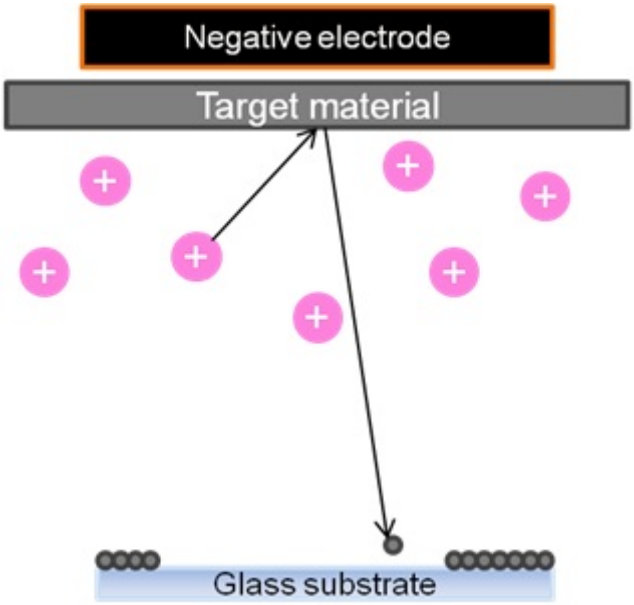

Figure 3.1: A representation of magnetron sputtering with ionised argon atoms in pink and loose target particles in grey.

the introduction of reactive gases into the chamber during deposition, to improve characteristics of the film. Reactively sputtering with oxygen is perhaps the most used when depositing TCOs, especially during the deposition of doped indium oxide TCOs. But it is also possible to reactively sputter with nitrogen to form conductive nitrides, such as TiN.

TCOs used during research presented in this thesis were deposited in an AJA International (USA) ATC Orion 8 magnetron sputtering system from 3" diameter, 0.125" thick ceramic targets. To enable lengthy depositions, all the target mounting guns have a watercooling system. A load lock system to load samples without venting the deposition chamber was installed, typically keeping the main chamber pressure around $1x10^{-7}$ mTorr, despite periods of heavy use. Thanks to a fully automated system, a VAT pressure adaptive gate mounted in front of the main turbo-pump and mass flow controlled gas inputs; the pressure of the deposition can be finely tuned and controlled ensuring excellent reproducibility. The use of two 1 kW halogen bulbs below a plattern sample holder, the substrate may be heated to temperatures of 500 °C. Any samples vacuum annealed during the course of this work will have been done so in this apparatus.

Substrates used for TCO deposition were 50 x 50 x 11 mm soda-lime glass slides (Fisher Scientific, UK). The nature of the atomic scale deposition requires that the substrates must be cleaned to a high standard before use. Prior to use, 10 glass slides are cleaned with a brush in a soap and de-ionised water solution. Next the slides are placed into a PTFE sample holder designed to fit into a 500 ml beaker and immersed into a solution containing soap and DI water. This beaker is placed into a sonicbath at 70 °C for 20 minutes. The samples are rinsed with DI water to remove any excess soap and placed into a solution, RCA 1, which contains 50 ml ammonia solution, 50

ml hydrogen peroxide (40 % v/v) and 250 ml DI water. The samples are left to soak for 10 minutes at 70 °C, which after that time are removed and rinsed. The samples are then immersed into a second and final cleaning solution, RCA 2, which contains 50 ml conc hydrochloric acid, 50 ml hydrogen peroxide (40 % v/v) and 250 ml DI water and soaked for 10 minutes at 70 °C. Finally the samples are removed and rinsed with DI water before being stored in a breaker with 350 ml DI water until needed for use in a deposition. Prior to loading into the load lock the samples are dried using a compressed nitrogen line.

3.2 Material Characterisation

3.2.1 UV-Vis-NIR Spectrophotometry

The optical properties of a transparent conducting oxide thin film material will identify its potential performance in a solar cell. Typically a thicker TCO will lead to a more conductive film, whilst also reducing the transmission through the film. As a result the overall transmission of the film is measured, which can then be used with a device EQE to estimate the maximum current achievable for a particular PV device.

Measurements of transmission and reflection were made using a Cary 5000 UV-Vis-NIR Spectrophotometer (Varian, USA). Baseline measurements were made first using air as a reference instead of glass so that the transmission data would indicate all of the available light a solar absorber would be exposed to. Both transmission and reflectance measurements are made between 200 - 1800 nm with the use of an integrating sphere. It is possible to better compare TCOs by correcting for the substrate used, by subtracting the absorption of the TCO from 100 % it is possible to compare TCOs from other laboratories without having to take into consideration reflection and absorption of the substrate.

Estimation of the Band Gap

It is possible to estimate the band gap of any TCO from its transmission and reflectance measurements. The Beer-Lambert law describes the interaction of light as it passes through a material, such as a solution or in this case a thin film. This interaction for a solid material is expressed below in Equation 3.1.

$$I_x = I_0 exp\left(-\alpha d\right) \tag{3.1}$$

From this equation it is possible to calculate the absorption co-efficient for a material given its transmission properties. This relationship for the interaction of incident light with a material can be visualised in Figure 3.2.

Incident light, I_0, may also be represented relative to the reflective losses incurred from the surface of a material. If I_0 is the total of all light, the subtracted percentage

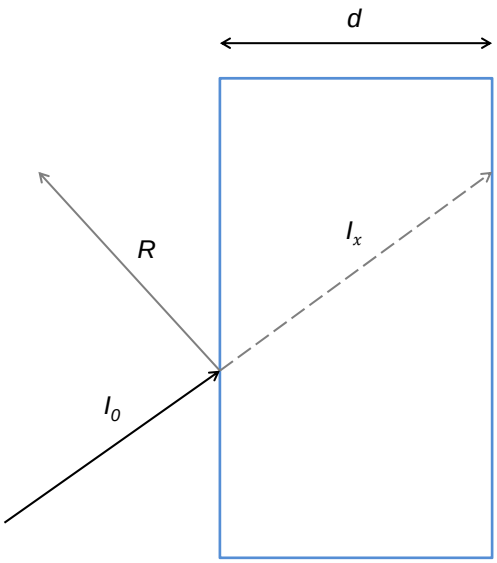

Figure 3.2: A visual representation of how incident light, I_0, is initially reflected, R and then transmitted, I_x, through a solid material with thickness, d.

of reflected light, R from 1 will equal I_0. which is expressed in Equation 3.2.

$$I_0 = 1 - R \tag{3.2}$$

It is possible to calculate the absorption co-efficient from both Equation 3.2 and Equation 3.1. Substitution of Equation 3.2 and Equation 3.1 and rearranged to give the absorption co-efficient, α as seen in Equation 3.3, which is vital for the estimation of the band gap.

$$\alpha = -ln\left(\frac{I_x}{1-R}\right)\frac{1}{d} \tag{3.3}$$

With transmission data, reflectance data and film thickness it is possible to estimate the bandgap of a TCO thin film through the use of a Tauc plot. By plotting $(\alpha h\nu)^r$ against $h\nu$ it is possible to display the absorption spectrum for a given wavelength of a material. The onset of absorption can be seen from the linear absorption relationship. Extrapolation of this to the x axis results in the determination of the band gap for the material.

3.2.2 Sheet Resistance and Hall Effect Measurements

Sheet Resistance

Four point probe measurements are carried out to determine the sheet resistance of deposited TCO films. These are carried out using a four-point probe (Jandel Engineering LTD, UK) connected to a source meter (Keithley, USA). The four probes are brought into contact with the TCO surface in order to take the measurements.

It is possible to approximate the resistivity of a TCO using a four-point probe

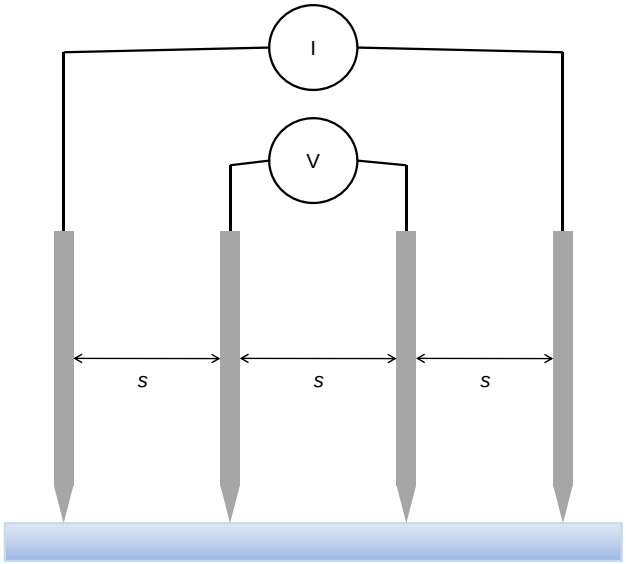

Figure 3.3: A basic visualisation of the 4 point probe configuration with the TCO below. Each probe is equidistant, s, with an applied constant current, I, across the outermost probes and the voltage, V, measured on the innermost probes.

although Hall measurements are more accurate and as such are used to calculate the resistivity. It is possible to crudely measure the resistance across the film between the probes contacts using Ohm's law. However as this law does not consider the spatial dimensions of the TCO film being measured, it is necessary to include a correction factor to give a more accurate measurement.

$$R = \frac{V}{I} \tag{3.4}$$

The correction factor is derived from the geometry of the semiconductor; it is assumed that current supplied from the outermost points follows a spherical path. However for a thin film semiconductor the current will follow the path of a ring rather than a sphere. For a thin film with thickness t the resistivity ρ of a thin film will be

$$\rho = \frac{\pi}{\ln 2} t \left(\frac{V}{I}\right) \tag{3.5}$$

It is possible to define the sheet resistance R_{sheet} as:

$$R_{sheet} = \frac{\rho}{t} \tag{3.6}$$

Substitution of Equation 3.6 into Equation 3.5 will give Equation 3.7 which is solved to give the correction factor of 4.532. As a result sheet resistance measurements are carried out with a current of 4.532 mA and a voltage sense in the mV range. This current enables any value read from the source meter (in mV) to be given as the sheet resistance in $\Omega/\square$.

$$R_{sheet} = 4.532 \, \frac{V}{I} \tag{3.7}$$

Hall Effect Measurements

Hall effect measurements are a useful characterisation of a TCO used to determine the resistivity, ρ, the carrier concentration, N, and the mobility, μ, of the semiconductor material. These measurements were carried out using an Ecopia HMS 3000 Hall measurement system using the Van der Pauw method [95]. Samples are cut into 1 cm x 1 cm pieces and mounted into a sample holder with contacts taken in the four corners of the thin film.

3.2.3 X-Ray Diffraction (XRD)

Structural characterization was performed using powder X-Ray diffraction on a D2 Bruker X-Ray diffractometer. Samples were analysed for 30 minutes with results cross referenced against the International Centre for Diffraction Data (ICDD) database, a database of over 815,000 unique data sets for XRD measurements of materials. The diffractometer used was not capable of grazing angle measurements.

3.2.4 Scanning Electron Microscopy (SEM) and Transmission Electron Microscopy (TEM)

Scanning Electron Microscopy and cross-section Transmission Electron Microscopy. STEM imaging was carried out using a FEI Tecnai F20 (S)TEM, collected using a Bright Field detector at 200 kV. The TEM samples were prepared by Focused Ion Beam (FIB) milling using a dual beam FEI Nova 600 Nanolab. A standard in situ lift out method was used to prepare cross-sectional samples through the coating into the glass substrate. A Pt over-layer was deposited to define the surface of the samples and homogenise the final thinning of the samples, down to 75 nm.

3.3 Device Fabrication

Dye-sensitised Solar Cells

In order to fabricate dye-sensitised solar cells a comprehensive guide published by Ito *et al* is followed with slight adaptation. TiO_2 electrodes are deposited onto a 5 cm x 5 cm TCO/glass substrate. The thickness of the substrate will change depending on whether the TCO was deposited manually or commercially bought in. This glass substrate can have a choice of different coatings, but typically in non-tandem DSCs commercially available fluorine-doped tin oxide (FTO) coated glass is used (Pilkington TEC™ 7, 8 or 15). The product number denotes the conductivity of the film, referring to the sheet resistance in $\Omega/\square$. The sheet resistance is directly related to the transmission of the FTO, with thicker FTO films giving superior conductivity, but a reduction in the transmission of photons.

The FTO substrate is treated in a 40 mmol $TiCl_{4(aq)}$ solution for 30 minutes at 70 °C, prior to the application of TiO_2 electrodes. This treatment forms a thin layer of TiO_2 to enhance adhesion of the electrodes to the substrate as well as blocking surface recombination of electrons in the finished cell, leading to a preferential increase in shunt resistance. Screen printing is often the preferred deposition method for TiO_2 electrodes in the fabrication of high efficiency DSCs, as this method offers better control of electrode thickness and density over methods such as doctor blading. Two TiO_2 pastes are used to make a bilayer working electrode in a standard DSC, a transparent layer (18NR-T, Dyesol) and scattering layer (18-NR-A, Dyesol). The transparent layer is applied first, acting as semi-transparent layer once dyed, with a typical particle size of 40 nm. The optimisation of the thickness of this layer varies between research groups, but a layer of 10 um is used in this thesis unless stated otherwise. The scattering layer uses larger particles of around 200-400 nm, which are designed to absorb more of the near infra-red spectrum, to enhance the current density of the DSC. This layer is typically deposited to be a thickness of 6 μm and is applied after the transparent layer.

Once the TiO_2 electrodes have been screen printed to the FTO, the substrate is then annealed to a temperature of 450 °C. At temperatures close to 400 °C the ethyl cellulose binders giving the TiO_2 paste its viscous consistency, begin to burn, turning the electrodes temporarily black. Left sufficiently long enough (ca. 20 mins) all of the binding agents will be burnt, oxidised and removed, leaving the electrodes a bright white colour. Once cooled to room temperature a successive $TiCl_4$ treatment is performed, identical to before. Finally the electrodes are washed with de-ionised water and dried, of which they are then sintered at 500 °C for 30 mins to improve TiO_2 crystallinity.

Once cooled the substrate is cut into twelve individual 1.25 x 1.7 cm working electrodes and immersed into a sensitizing dye solution, typically of a concentration of 0.3 mmol. The dye time and dye container is crucial to the adsorption onto the TiO_2, if the electrodes are not exposed long enough an insufficient uptake will lead to poor performance. 22 hours is usually sufficient for regular ruthenium dyes such as the N719 ruthenium based dye.

Counter electrodes are made of the same FTO substrate used to make the working electrodes and are cut to match the dimensions of the working electrode. A hole is sandblasted from the glass side through to the FTO with a diameter of approx 1-5 mm. These are then washing in an IPA solution and left in a sonic bath for 20 mins to remove and particles from the sandblasting process. The counter electrodes are dried and heated to 400 °C in air to remove any organic contaminants. These are cooled and a drop of Platisol™(Solaronix) is added to each counter electrodes FTO surface. This solution contains a chemical platinum precursor, which following a successive heat treatment at 400 °C, removes any binding agents to leave a compact layer of Pt atoms on the counter electrode to serve as a catalyst for the hole conductor electrolyte

used layer in the cell.

Once dying of the working electrode is completed, it is washed in acetonitrile to remove excess dye solution and bonded to the counter electrode using a hot-melt polymer gasket (Surlyn™). This gasket is arranged around the TiO_2 working electrode and the counter electrode is placed on top with the sandblasted hole in line with the working electrode. This stack is then carefully placed onto a hot plate at 130 C, the heat melts the polymer gasket to form a tight seal around the electrodes. The iodide/tri-iodide electrolyte is added through the hole with the aid of a vacuum pump, which is then sealed with a piece of Surlyn™ and a watch glass cover. Contacts are ultrasonically soldered onto to exposed parts of the FTO substrates ready for characterisation of the cell.

3.4 Device Characterisation

3.4.1 Current-Voltage (I-V) Measurements

The accurate measurement of photovoltaic devices is an important characterisation step in the development and certification of solar cells. An equivalent circuit diagram may be drawn to model the electrical behaviour of a solar cell, shown in Figure 3.4. The p-n junction of a solar cell does not display ideal diode performance due to series and shunt resistance (R_s and R_{sh} respectively). Series resistance is an opposition to current flow through the cell material, front contacts and resistive contacts. Shunt resistance is caused by a leakage of current across the p-n junction, crystal defects, between contacts of different polarity and through the edges of the device.

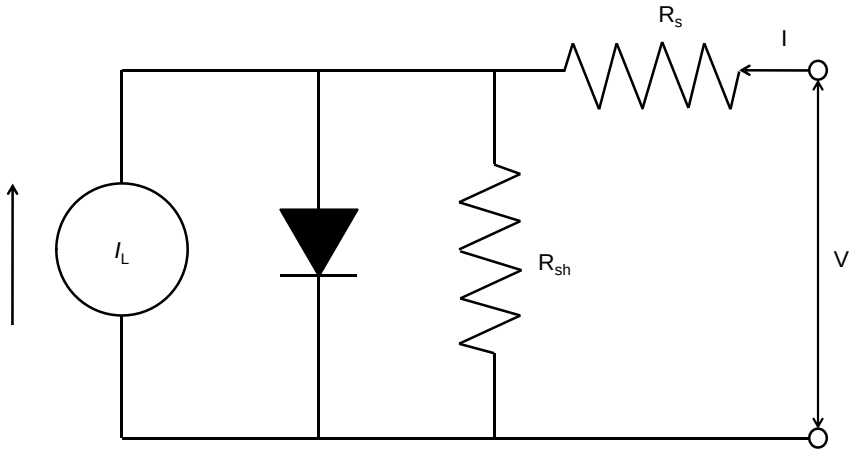

Figure 3.4: An equivalent circuit of a non-ideal solar cell locating the series and shunt resistances in a solar cell. The current supply, I_L, is photo-generated, whilst the diode represents the rectifying depletion zone.

Modelled I-V data of an ideal diodic photovoltaic cell is shown in a current-voltage graph in Figure 3.5. Two curves are present on the graph, one is that to be expected

from a device when measured in the dark and the other expected when under illumination. When measured in the dark, the cell will behave as a rectifying diode, which will undergo reverse breakdown if measured with a great enough bias. Under illuminated conditions the curve will be down shifted to intersect the y axis, this value is the short circuit current density (I_{sc}). Intersection of the x-axis will determine the cells open circuit voltage (V_{oc}). This also gives the current density and voltage (I_{mp} and V_{mp}) at the maximum power point (M_{pp}).

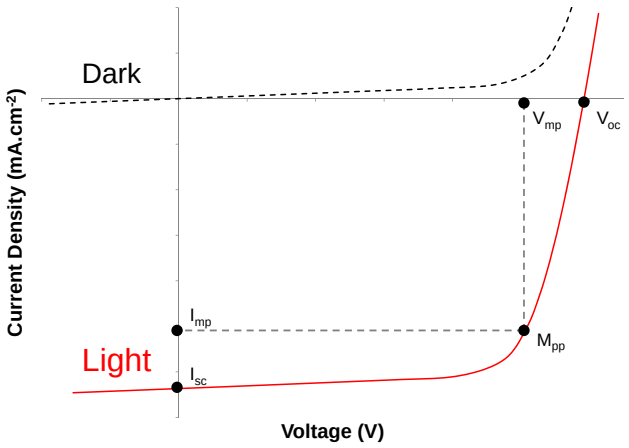

Figure 3.5: An ideal I-V curve from a solar cell plotted using modelled data.

The mathematical representation of current generation in a solar cell is expressed using a modification of the Shockley diode equation:

$$I = I_0 \left(exp \left(\frac{V + IR_s}{k_B T} \right) - 1 \right) + \frac{V + IR}{R_{sh}} - I_{ph} \tag{3.8}$$

Measurement of an illuminated cell is achieved using a linear voltage sweep and measuring current. By measuring the I-V curve of a solar cell it is possible to calculate how efficiently the device converts absorbed photons into electrons that may be made to do work shown by:

$$\eta = \frac{I_{mp} V_{mp}}{P_s} \tag{3.9}$$

$$\eta = \frac{I_{sc} V_{oc} FF}{P_s} \tag{3.10}$$

Where η is efficiency, P_s is the incident light power density and FF the fill factor, defined by:

$$FF = \frac{I_{mp} V_{mp}}{I_{sc} V_{oc}} \tag{3.11}$$

Solar Simulator

The solar simulator used to characterise the devices fabricated in this thesis used a solar simulator closely matched to the AM 1.5G spectrum (Sciencetech, Inc) using an appropriate filter and Xenon arc lamp (1 kW, Osram XBO1000W/HS). The illuminated area was a 15 cm x 15 cm sample holder, custom designed to enable simple loading of DSCs. The DSCs would sit in the centre of the holder, which could be raised or lowered away from the illumination source. This was also a convenient assist to the calibration of the simulator illumination, which was achieved by measuring the current output of a reference silicon photodiode.

A KG5 (Schott) glass filter was placed above the reference photodiode and the sample holder raised or lowered until a predetermined current output was measured. The KG5 filter is applied to better simulate the spectral response of a DSC (dyed with N719), as a number of wavelengths not absorbed by the DSC otherwise contribute to the calibration measurement. Their subsequent removal by the filter enables the illumination to better match the wavelengths present in AM1.5G, which are absorbed by the DSC [96].

The I-V measurement was made in a 4-wire configuration (for both DSC and tandem cells fabricated in this thesis) and the voltage swept from -0.4 V to 1.4 V. This was measured using software developed at CREST using LabVIEW, which in turn controlled a sourcemeter (Keithley 2425).

3.5 Conclusion

Presented in this chapter are the methodologies used to produce any data or devices presented in this thesis. The measurement and fabrication techniques described are commonplace in the area of DSC photovoltaics. As a result data in this thesis is presented in a comparable format to that expected for research publications and comparative analysis with other published research. Any deviation from the fabrication and/or measurement techniques presented in this chapter will be described as they appear in their relevant chapter and will either be presented as novel or cited appropriately.

Chapter 4

HIGH MOBILITY TRANSPARENT CONDUCTING OXIDES FOR USE IN TANDEM SOLAR CELLS

4.1 Introduction

A transparent conducting oxide (TCO) is a thin film metal oxide (also generalised as Transparent Conductors), often n-doped for use in opto-electronics often as a front contact. These materials have existed since the 1940s and are present in nearly every LCD panel. This class of materials are considered as a primary element for any optoelectronic device, as it acts as a contact as well as a window for light. The most common of these TCOs is tin-doped indium oxide (ITO) which has a good transparency in the visible range of the electromagnetic spectrum, along with a low resistivity and high carrier concentration. As a result of these properties TCOs have also found use as contacts in solar cells. Dependant upon whether the device is in substrate (e.g. CIGS) or superstrate (e.g. CdTe), the TCO is the first layer thin film layer for light to pass through in a completed PV device. Because of this TCOs in a solar cell must have a high transparency and low reflectivity, increasing photon transmission and reducing optical losses, contributing to a more efficient solar cell.

To achieve the required sheet resistance and transmittance for use in solar cells, the resistivity of a TCO would ideally be in the range of ρ<1-3 x10^{-4} Ω.cm, although values in the range of 10^{-3} Ω.cm are not uncommon for TCOs deposited at room temperature such as ITO. This translates to seet resistances of ca. 20 Ω/□although this is dependant upon the thickness of the film. The transmittance of the TCO film would need to be between 80-90 % between 300-1200 nm to be comparable to ITO. ITO is currently the most commonly used TCO in the opto-electronics industry. The charge carrier density typically has values $\geq 10^{20}$cm^{-3}, requiring relatively low

mobility values of 10-20 $cm^2.V^{-1}.s^{-1}$.

4.1.1 Requirements of TCOs as Tandem Cell Contacts

The TCOs commonly used in blue absorbing solar cells suitable for tandem applications absorb a large portion of available near-infrared photons (800-1800 nm) due to free carrier induced photon absorption. This is a result of the desirable properties of this material, caused by its relatively high carrier concentration. This reduction of near-infrared photons reaching the bottom absorber reduces the current generated when compared to its single junction counterpart. Current matching is an important part of multi-junction cell design, requiring both absorbers to generate similar currents under illumination. This requires both parts of the device to be optimised in a different configuration to that of their single junction counterpart, for example the scattering layer of the DSC is removed to ensure efficient transparency to the bottom layer. This significantly reduces the current generated from the DSC, but the enhanced transparency of near-infrared photons increases the bottom absorber performance. This transparent TiO_2 layer may be made thicker to generate more current to counteract these losses but the performance increase is limited.

To improve the efficiency and current generation of some multi-junction devices it is necessary to investigate TCOs which may reduce photon absorption in the near-infrared. Not only must the TCO chosen display a high near-infrared transparency, it must be compatible with current device fabrication processes. For example, DSC fabrication requires the TCO substrate to be chemically and thermally stable, properties that make FTO a popular choice in their fabrication is that it is able to withstand exposure to high temperatures in air and the acidic processes vital in ensuring the compact TiO_2 layer deposition. Finally the TCO must have comparable electronic properties to ITO or FTO, otherwise any superior optical properties displayed may not lead to an overall improvement in device performance.

4.1.2 High Mobility TCOs

The combination of a high carrier concentration in FTO and ITO are attributed to the low resistivity needed for use in solar cells. However free carriers are primarily responsible for the absorption of near-infrared photons. The conductivity, σ, of a transparent conducting oxide (or its reciprocal, resistivity, ρ) of a TCO are governed by the mobility, μ, charge carrier density, N and the electric charge, q of the material:

$$\sigma = \frac{1}{\rho} = \mu N q \tag{4.1}$$

As a result a material suitable as a TCO for tandem applications requires a reduced carrier concentration without compromise of the electrical properties. To accomplish this the material would require a larger carrier mobility to compensate, as free carriers

availible for charge transport are in fewer numbers. It has been shown using Drude's model that increasing the mobility in a material with a fixed carrier concentration reduces its absorptance in the near-infrared [97].

Investigation into improving the mobility of existing TCOs has been undertaken, although the direct relationship between transmittance and TCO electrical performance is not fully understood [98]. It has been shown that the mobility of an n-type TCO may be improved through empirical experimentation, by improving the quality of the materials crystallinity. This has been performed in high mobility TCOs through the determination of dopant concentration [99], post deposition annealing of the TCO [100] and modification of the deposition parameters [101][102].

4.2 Titanium-doped indium oxide

Titanium-doped indium oxide (ITiO) is a high mobility TCO suitable for use in tandem DSC/Cu(In,Ga)Se_2 solar cells. It has a relatively high mobility $\geq$100 $cm^2.V^{-1}.s^{-1}$ and a much lower carrier density than other TCOs typically $\sim 10^{19}$ cm^{-3} which translates as a significant improvement in the transmission of near-infrared photons which can be seen in Figure 4.1. Its electronic properties are also suitable, able to demonstrate a similar, if not better, resistivity to that of ITO and FTO. Unfortunately ITiO suffers from similar chemical and thermal instability properties as ITO, which results in a need to suitably modify the fabrication process of a DSC when used as the TCO [103]. The application of an additional thin tin oxide layer (20 nm) on top of the ITiO can assist in allowing the processing of ITiO in a $TiCl_4$ bath, for surface treatments necessary in a DSC fabrication [104].

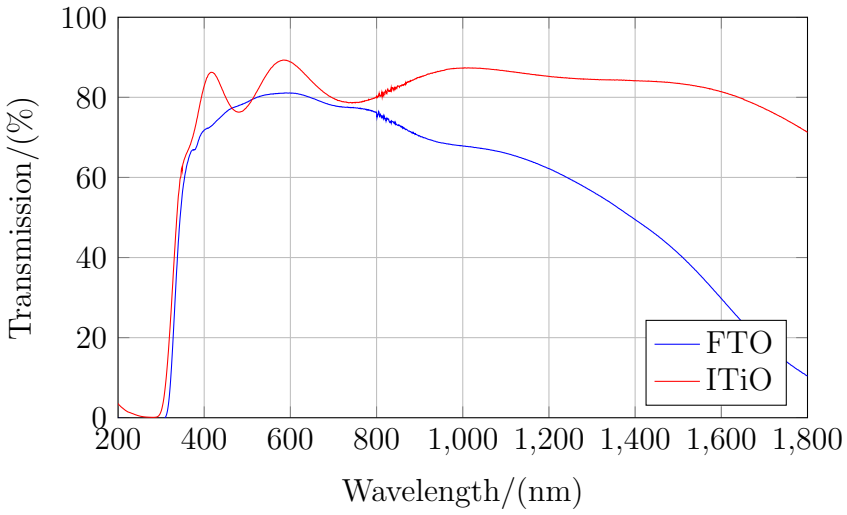

Figure 4.1: A comparison between UV-Vis-near-infrared spectra for commercially purchased NSG-Pilkington TEC 8 FTO, with a sheet resistance of 6 Ω/□ and as deposited ITiO with a sheet resistance of 8 Ω/□ . The absence of any interference fringes in the FTO transmittance data is indicative that the film has a relatively rough surface, unlike the ITiO film.

4.2.1 Optimisation of opto-electronic properties of titanium-doped indium oxide

As described previously the crystalline quality of TCOs are linked to the methods by which they are deposited. Superior results are typically achieved through the use of a process called sputtering. This vacuum process uses an ionised argon gas stream to mechanically remove material from an electronically biased target source by ion bombardment, upon which it recrystallises on a substrate typically placed at a perpendicular plane to the target source. This is a well developed process already widely used in industry for thin film growth onto a variety of substrates (including TCOs for LCD displays). Other methods of thin film growth exist which have been shown to deposit TCOs with sufficient optical transparency and ideal resistivity requirements. The high temperatures required to recrystallise the TCO on the substrate suface causes problems for atmospheric based deposition processes as these higher temperature typically cause additional oxidation incorporation into the film, thus reducing the overall film conductivity. Other methods such as evaporation often fail to match the throughput of sputter coating as well as the relative simplicity to operate and serve the equipment.

The optimization of deposition parameters via magnetron sputtering can largely be a process of trial and error with new materials, however for more common materials (such as In_2O_3, ZnO and AZO) changes to particular process parameters will modify the opto-electronic properties in a controlled and predictable fashion, although the magnitude of the change cannot be easily predicted. For example an increase of oxygen concentration in the plasma leads to a higher resistance and greater transparency in deposited films for materials such as ITO and AZO.

When a new target is installed in magnetron sputtering equipment and used for the first time it must typically be conditioned and optimised before depositing useful films. Following a burn-in whereby the target is subject to deposition parameters for several hours with the shutter door closed, samples are then taken under different conditions in order to determine the parameters that will deliver a film with optimum performance. ITiO films are deposited in this thesis from ceramic targets, with a 2% wt. TiO_2 : 98% wt In_2O_3, by reactive magnetron sputtering. This particular ceramic target is not conductive enough to allow sputtering using a DC power supply and as a result the popular choice for deposition has been to use a Radio Frequency (RF) power supply.

For the optimization of thin films deposited by sputtering the main process parameters to alter which have the most significant effect are the temperature of the substrate during deposition, the working pressure, target power density and the oxygen partial pressure. From previous investigations into ITiO the target power density and substrate temperature were fixed at 450 °C throughout the work presented in this chapter.

Sputtering at low working pressures is known to increase the quality of electrical and structural performance of a thin film. Ejected target material has a greater mean free path at lower pressures as there are fewer argon plasma ions, leading to more material deposited with a much higher crystallinity. This is exploited in the deposition of Mo onto glass substrates during CIGS solar cell fabrication, as high stress between Mo and glass can lead to delamination of the film. Deposition of Mo at a higher working pressure causes a less dense, lower quality film to adhere to the substrate with lower stress. Following this a second layer of Mo is deposited on top at a lower pressure to deliver the low resistivity required, that is not provided by the layer deposited at a higher working pressure. Introduction of oxygen into the argon plasma during deposition will introduce additional oxygen atoms into the deposited film. This is particularly useful for materials where by the exact oxygen composition from the target to the deposited film is reduced, typically leading to a more metallic film. This allows for a degree of control over the transparency and resistivity of the deposited film. Reactive sputtering with oxygen also reduces the deposition rate and can lead to a poisoning effect, where the surface of the target forms a thick oxide. This can make successive depositions difficult, as the plasma may not stay lit at lower pressures until the oxide layer is removed by a pre-cleaning step.

To determine the optimum working pressure and oxygen concentration at which ITiO films would achieve desired performance parameters for use in tandem solar cells, a series of depositions were carried out at varying working pressures and oxygen concentrations. Films that delivered a superior sheet resistance with desired transparency were used as a benchmark and those deposition conditions were considered as optimal. A summary of the process parameters are shown in Table 4.1 with their corresponding sheet resistances. The full experimental proceedure for films deposited during the rest of this chapter can be found in the methology, any derivation from this method will be explained in sequence.

Looking at Table 4.1 we can see that the introduction of oxygen during deposition has a detrimental effect on the electrical performance of the ITiO films. The films without additional oxygen during deposition provide useful sheet resistances for films deposited for only 30 minutes. Despite the reduced electrical performance brought about from the introduction of oxygen into the sputtering plasma the use of reactive sputtering using the ITiO targets supplied for this project was vital. It was found that an absence of oxygen during deposition led to films that would easily de-laminate from the soda-lime glass substrate. The reason for this is still not fully understood, however it was hypothesised that it could be caused from a poor crystalline structure due to a deficiency of oxygen atoms deposited in the bulk from the target, leading to the hazy metallic-like film seen. Despite delivering a sheet resistance that would be expected for an ITiO film, the bulk of the film could easily be removed by rubbing the surface with a non abrasive material.

From the transmission data for each of the films, seen in Figure 6.2 it can be seen

Table 4.1: Deposition conditions and film sheet resistances of ITiO films deposited with different oxygen in plasma concentrations. All films were deposited for 30 minutes at 450 °C.
*o/s - (off scale) films measured with the four-point probe would not display a sheet resistance in the desired scale ($\leq$ 200 $\Omega/\square$)

Sample	Pressure Deposited/ (mTorr)	Oxygen in Plasma/ (v/v%)	Sheet Resistance/ $\Omega/\square$
13A0325	1	0	18.7
13A0326	5	0	26.1
13A0327	10	0	37.5
13A0312	1	1	26.0
13A0315	5	1	o/s*
13A0317	10	1	o/s*
13A0294	1	10	o/s*
13A0295	5	10	o/s*
13A0296	10	10	o/s*

that the increase in oxygen during deposition increases the transparency through the glass/TCO stack. The electrical properties in Table 4.1 identify that the process parameters belonging to the sample 13A0312 are ideal, as it is the only reactively sputtered film to deliver a sheet resistance, as the non reactively sputtered films are too fragile to be of any use (and have poor transmission properties). The trends in resistivity and transmission are similar to that seen previously during group investigation into AZO and ITO films.

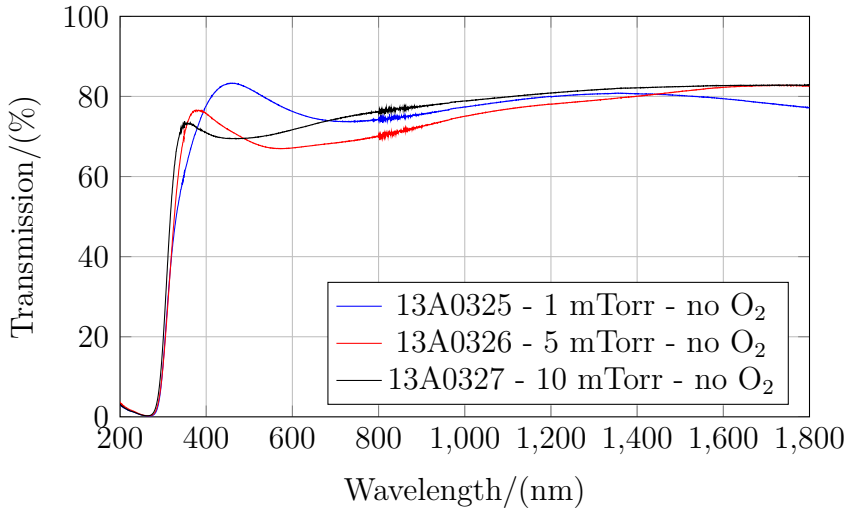

(a)

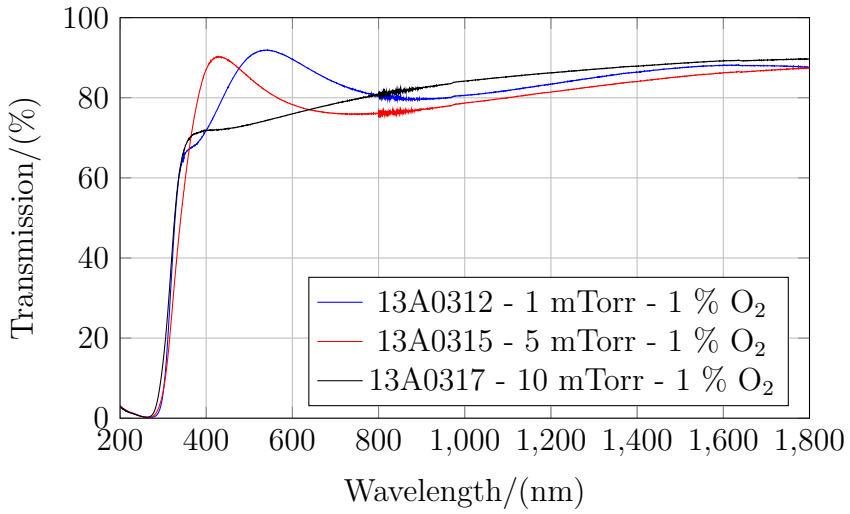

(b)

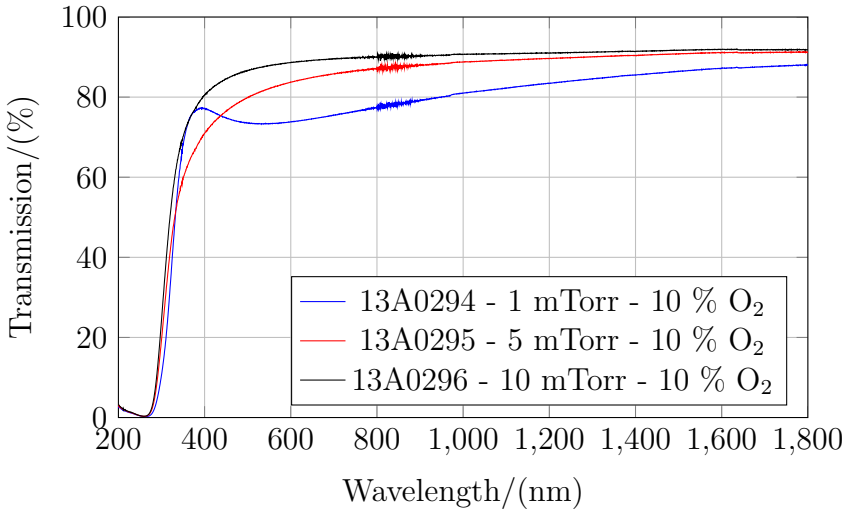

(c)

Figure 4.2: Comparison of ITiO films deposited by RF magnetron sputteirng for 30 minutes each at increasing pressure at (a) no O_2, (b) 1 % O_2 and (c) 10 % O_2 plasma partial pressures.

4.3 Pulsed DC Magnetron Sputtering of ITiO Thin Films

4.3.1 Motivation

The use of a RF power supply for magnetron sputtering is commonly known to deliver thin films with a high quality crystal structure, but reduce the throughput of the process due to a relatively slow deposition rate in comparison to DC and pulsed DC power supplies. Combined with reactive sputtering processes the deposition rate can be further drastically reduced, such as is the case with AZO and TiO_2. If ITiO films are to be considered as a potential candidate in low cost multi-junction solar cells they must also be cost effective. There are many studies to suggest that the World's current and unexploited indium deposits may not be able to sustain the future demand for ITO in thin film displays [70]. This future supply and demand complication would enivitably lead to an increase in cost for indium, because of this the cost to produce ITiO films should be kept to an absolute minimum if possible without any loss of performance in the film. Increasing the throughput of any production line will lead to a reduction in cost per unit produced, but in this example the quality of the product must not be affected. A potential way to increase the throughput of the ITiO thin films is by increasing the deposition rate by using a pulsed DC power supply. Unlike a typical DC power supply, the pulsed DC power supply is designed to be compatible with low conductivity materials. Similarly to a DC power supply it is able to deposit thin films with a relatively high deposition rate, especially when compared to RF power supplies. Capital costs for the pulsed DC unit are also cheaper, as RF power supplies require impedance matching networking equipment, which can be very expensive in addition to the intial outlay of a vacuum system. A potential disadvantage of the pulsed DC process however, is the kinetic energy which the ejected target particles possess when they reach the substrate surface.

It has been suggested that methods such as pulsed DC sputtering can damage the film as it is deposited, potentially leading to a film with reduced mobility and resistivity [105]. This could potentially be a severely limiting factor for this technique when depositing ITiO films. As it is imperative that ITiO films have a high mobility to make up for their intrinsic low carrier concentration, previously dictated by the relationship in Equation 4.1. It is important therefore to determine the effects, if any, of using a pulsed DC power supply to deposit ITiO thin films. If damages to the crystalline structure do lead to a reduced mobility, the effect on the film's performance should be investigated. For a useful comparison between power supplies a set of ITiO films were deposited from both power supplies. Optimum parameters have already been determined to produce a film with ideal performance, deposited using the RF power supply for comparison, another film of the same parameters needs to be deposited by the pulsed DC supply (referred to now as PDC). High working pressures

have also been determined to detrimentally affect the electrical performance of the ITiO films deposited by RF, so for comparison these pressures were also used for the PDC deposited films. To limit unwanted variation in transmission properties between films as a result of thickness variation, the samples were deposited at a set thickness as opposed to a pre-determined amount of time, as the deposition rates would be expected to vary. Under each set of conditions a film was deposited for 30 minutes. The thickness of this film was then measured and the deposition rate determined. Using the deposition rate for each set of conditions each sample was deposited to a thickness of 200 nm to ensure a film thick enough for materials characterisation techniques such as XRD, SEM and TEM. From previous optimisation work this is also a thickness likely to yield a film with suitable opto-electronic properties, using the optimum process parameters. This also ensures that electrical properties such as the sheet resistance, which is dependent on film thickness is being compared based on any changes in the film structure. For each power supply, RF and PDC a sample was deposited at 1, 5 and 10 mTorr. The PDC power supply was kept at its default settings with a frequency of 150 kHz and a reverse time of 3 μs. All other process parameters are kept as before, but are summarised below in Table 4.2.

4.3.2 Results

Table 4.2: Deposition conditions of the films grown to compare the differences between ITiO films grown using RF and pulsed DC power supplies. All films were grown at 450 °C with a power density of 3.28 W/cm^2.

Sample	Pressure Deposited/ (mTorr)	Power Supply	Mobility/ ($cm^2.V^{-1}.s^{-1}$)	Carrier Conc./ $x10^{20}(cm^{-3})$	Resistivity/ $x10^{-3}$(ohm.cm)
13A0337	1	PDC	101.90	1.88	0.33
13A0339	5	PDC	64.57	0.70	1.37
13A0341	10	PDC	39.29	0.28	5.74
13A0314	1	RF	108.31	1.72	0.34
13A0316	5	RF	35.28	0.33	5.41
13A0318	10	RF	10.05	0.27	22.65

From Table 4.2 it can be seen that the RF film deposited at a working pressure of 1 mTorr exhibited the highest mobility of all films in this study, although the PDC grown film demonstrates a comparable mobility and resistivity. The PDC 1 mTorr film exhibits the desirabled mobility of $\geq$ 100 cm^2.V^{-1}.s^{-1}, revealing that a PDC power supply does not decrease the mobility significantly when compared to an RF ITiO film deposited under the same conditions. In addition the film demonstrates desired properties for use in a multi-junction solar cell. As the pressure is increased during the deposition, the resistivity increases whilst the carrier concentration decreases across

all samples. Whilst a reduction in carrier concentration is desired for TCOs used in multi-junction devices, the mobility must also be increased to compensate. As expected from the earlier optimisation process the mobility decreases for both RF and PDC films as the pressure increases. As a result this unquestionably confirms that for both RF and PDC, sputtering at lower working pressures leads to a film with superior electronic properties. Quite interestingly though, is the difference in the extent of the reduced electrical performance at higher pressures between the RF and PDC power supplies. Although both sets of films see a reduction in performance, the PDC films appear to be more resilient to an increase in working pressure. It could be hypothesised that this could be attributed to the high kinetic energy that PDC ejected target material has relative to RF, leading to fewer unexpected trajectory alterations following collisions with Ar^+ ions, preserving energy whilst being deposited onto the substrate.

Table 4.3: Deposition rates for all ITiO films deposited by both RF and PDC.

Sample	Pressure Deposited/ (mTorr)	Power Supply	Deposition Rate/ ($nm.min^{-1}$)
13A0337	1	PDC	5.2
13A0339	5	PDC	4.5
13A0341	10	PDC	3.3
13A0314	1	RF	4.7
13A0316	5	RF	4.1
13A0318	10	RF	2.3

The deposition rates for films deposited by PDC are generally slightly higher than their RF film counterparts, which are all displayed in Table 4.3. As the pressure increases the deposition rate begins to decrease, which is to be expected as discussed previously. The rate of decrease between the 1 mTorr and 10 mTorr samples in the RF films though is interesting when compared to the PDC, as the sputtering rate decrease for RF is much sharper. This again could be attributed to the energy in which the PDC power supply grants the ejected material, giving it a greater likelihood of reaching the substrate following a collision leading to a thicker film. For a 200 nm ITiO film, a sheet resistance of 16.4 $\Omega/\square$ is obtained from the 1 mTorr RF deposited film. For use in a solar cell this value would preferably be closer to 10 $\Omega/\square$. We can roughly estimate the thickness of the film needed to supply this sheet resistance, from $R_{sheet}=\rho/t$. This would mean that an RF deposited film would need to be approximately 330 nm thick, taking 70 minutes to deposit. By comparison a PDC film deposited at 1 mTorr, which demonstrates a similar mobility, would take approximately 63 minutes for a 330 nm thick film. Although this difference in time appears to be fairly trivial, it translates to a much greater loss of time in an industrial environment. Especially when both methods are able to produce films with comparabe properties.

The transmission data for both the RF and PDC ITiO films can be seen in Figure 4.3. Each deposited film demonstrates a superior transparency in the near-infrared when compared to FTO, fulfilling the $\geq$ 80 % transmission criteria between 800 - 1800 nm. As all the films compared in this experiment are ca. 200 nm there is very little difference in transmission between the RF and PDC films and their pressure derivatives. Similarly to the increased electrical performance, the 1 mTorr samples do have a slight increase in transmission in the near-infrared compared to the other films. The 5 mTorr film stands out though with the lowest transmission across all wavelengths, this deposition was performed a number of times to rule out the possibility of potential contamination of the sample and/or target.

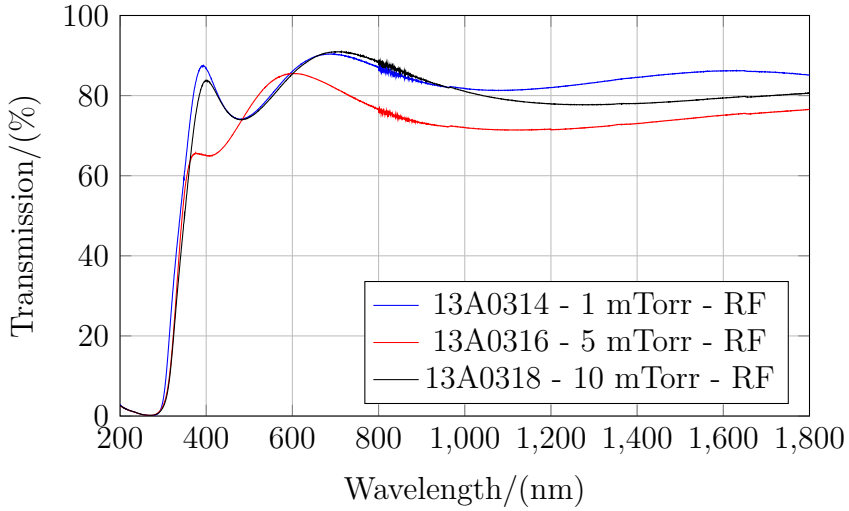

(a) %T of RF deposited ITiO

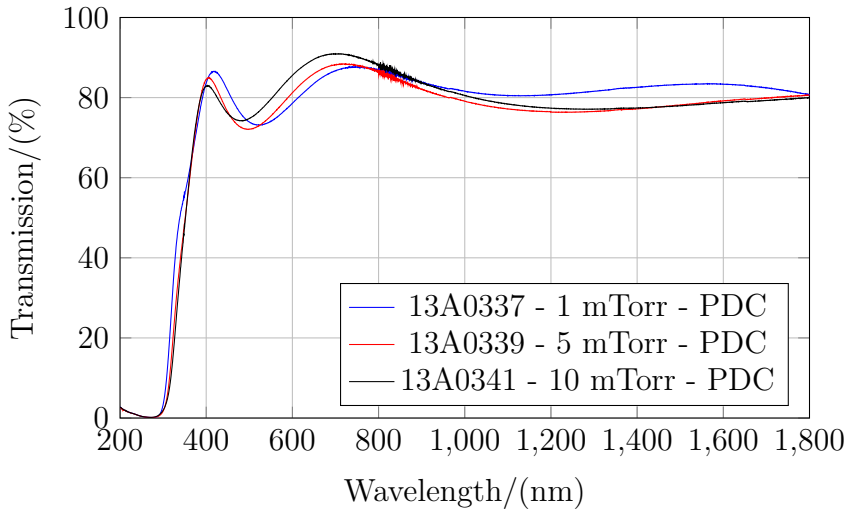

(b) %T of pulsed DC deposited ITiO

Figure 4.3: Transmission properties of all (a) RF and (b) pulsed DC power supply deposited ITiO films described in this study.

Investigation into the crystal structure can potentially eludicate to the cause of these trends seen. Powder X-ray diffraction is a particularly useful characterisation tool to assist in analysing the crystalline structure of ITiO films. Differences in the

film structure shown by XRD data becomes apparent between the pressure variations and the change in power supply, as shown in Figure 4.4. All ITiO films have a strong peak at 30.5°, corressponding to the (222) In_2O_3 peak, with the RF films displaying a much greater intensity relative to the other PDC peaks, which suggests a preferred orientation in this plane. It can also be seen that the increased working pressure for RF films shows a reduction in peak intensity relative to the 1 mTorr sample. The PDC sample set show a much stronger correlation to the peaks seen from an In_2O_3 diffractogram. Comparison of both 1 mTorr samples, chosen due to their presumed higher crystal quality, with the ICDD XRD database file (PDF 00-006-0416) shows a strong similarily between the PDC sample peaks and the database entry for In_2O_3 in the cubic phase. Due to the preferred orientation of the RF sample this match is not as strong, although some similarities can be seen. Both samples return a slight match with the 31° peak corresponding to the rutile phase of TiO_2 which is likely caused by the TiO_2 dopant present in the samples.

Scanning Electron Microscopy (SEM) is used to analyse changes in the film surface structure. SEM images are given for RF samples in Figure 4.5 and PDC in Figure 4.6. The PDC films deposited at all pressures have triangular shaped crystallites, with the size of these decreasing as the working pressure increases. The 5 mTorr and 10 mTorr samples appear to show gaps between the crystallites, possibly pin holes or pore channels, with the frequency of these increasing through up to the 10 mTorr sample. This appears to be in agreement with the electrical properties measured previously, as smaller crystallites lead to a greater concentration of grain boundaries, serving as an area of high resistivity for electrons thus reducing overall electrical performance. A trend is not as easily identified in the 1 mTorr RF sample, as the crystallite shape changes entirely compared to the 1 mTorr PDC sample. The 5 and 10 mTorr samples show similarities to their PDC counterparts, albeit with a slight increase in crystallite size and reduced pore/pinhole frequency. This is seemingly in contradiction to what would be expected from looking at the electrical properties of these films. The crystallites in the 1 mTorr film hold no similarity to either the other RF or PDC samples, with the RF 1 mTorr film crystallising into rice-grain shapes with no observable pores/pinholes but appearing to be more laterally oriented.

A cross section of the film will would allow further analysis of the bulk structure, particularly the growth pattern of the grains. Unfortunately the thickness was a limitation when attempting a fracture cross section with the FEGSEM equipment. As a result a higher resolution (S)TEM technique was used. The images of the RF and PDC films can be seen in Figure 4.7 and 4.8 respectively. As these samples have been measured using a bright field detector the glass substrate appears white in the image, which is not easily distinguished on a white background. These images are all positioned such that the glass substrate is always at the bottom of the image, with the scale bar overlaid. The black coating on top of the ITiO film is a sputtered layer of platinum, required for the imaging. Looking at the RF ITiO samples, the

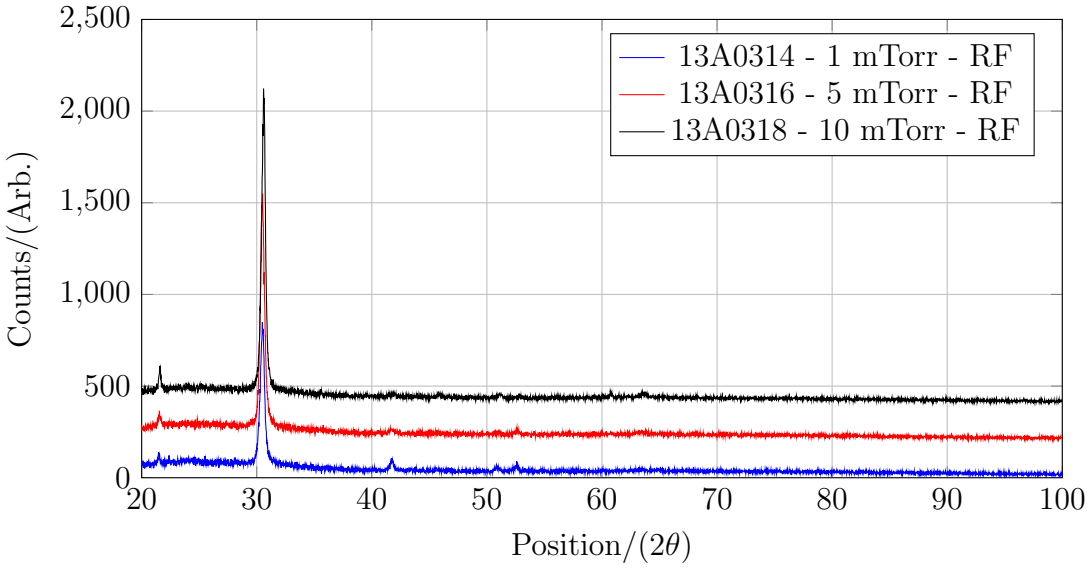

(a)

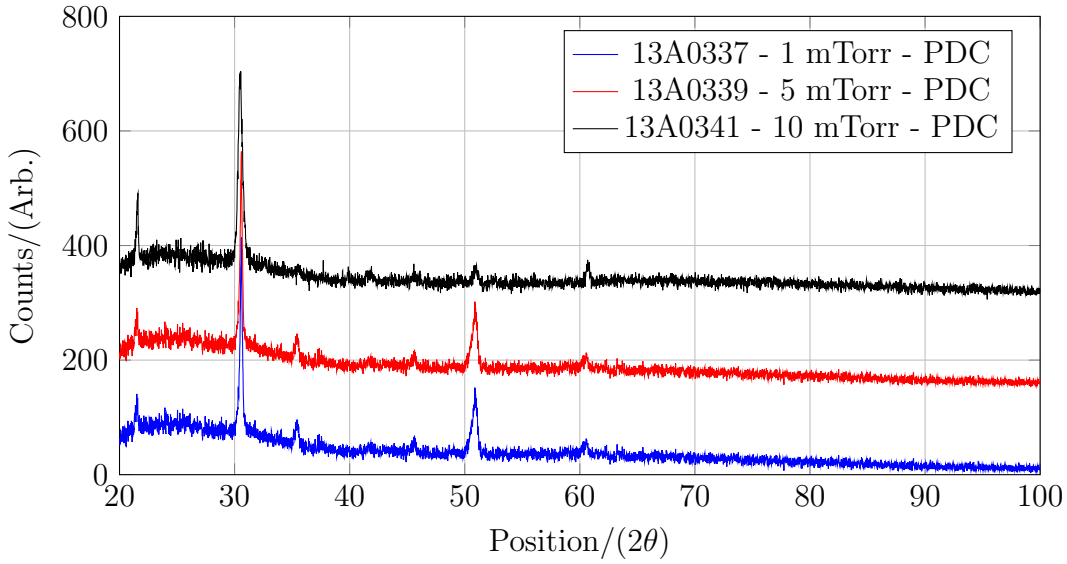

(b)

Figure 4.4: XRD diffractograms of both the (a) RF deposited and (b) PDC deposited ITiO thin films.

crystal structure appears to change between the 1, 5 and 10 mTorr samples. The 1 mTorr sample has poorly defined crystal grains in the cross section, unlike that seen in the SEM image, which would suggest very good crystalline quality. The increase in working pressure leads to a better definition of grain boundary, with pore channels appearing in the 10 mTorr sample. The grains in the 10 mTorr sample are much more narrow and less dense than those in the 5 mTorr sample, which explains the reduced electrical performance in the film.

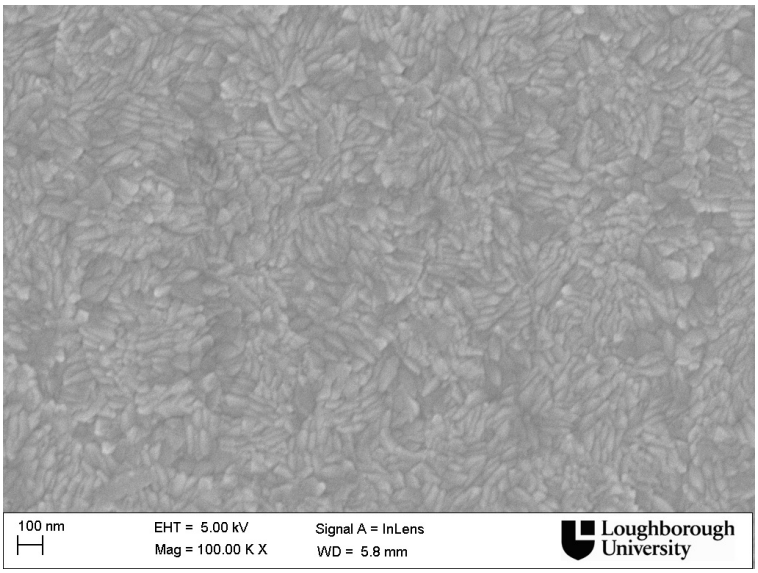

(a) 1 mTorr

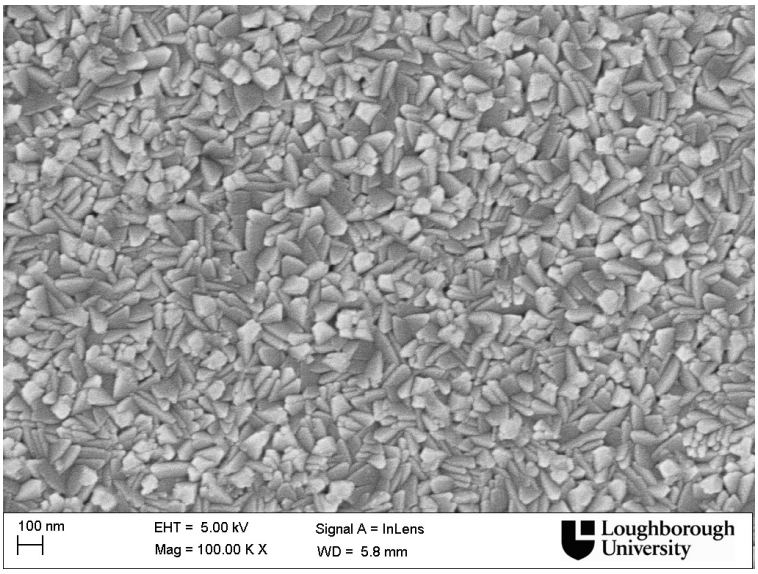

(b) 5 mTorr

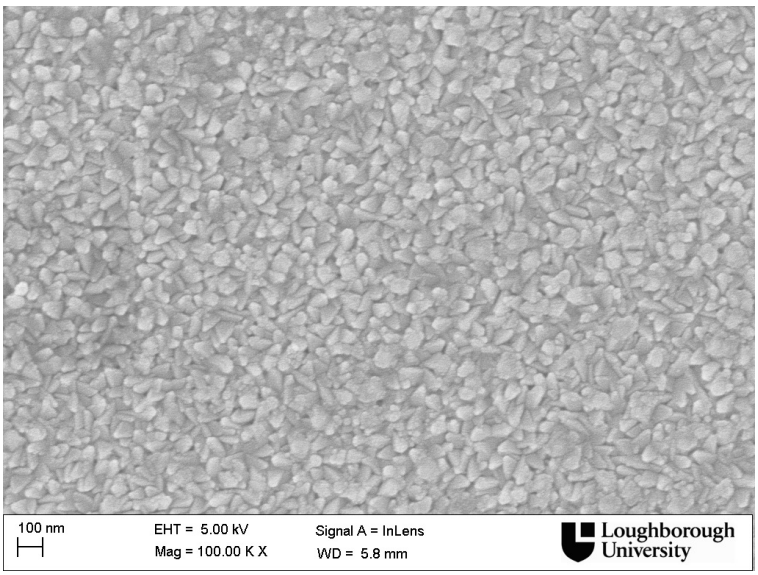

(c) 10 mTorr

Figure 4.5: Scanning electron micrograph images of ITiO films deposited at (a) 1 mTorr, (b) 5 mTorr and (c) 10 mTorr with a RF power supply.

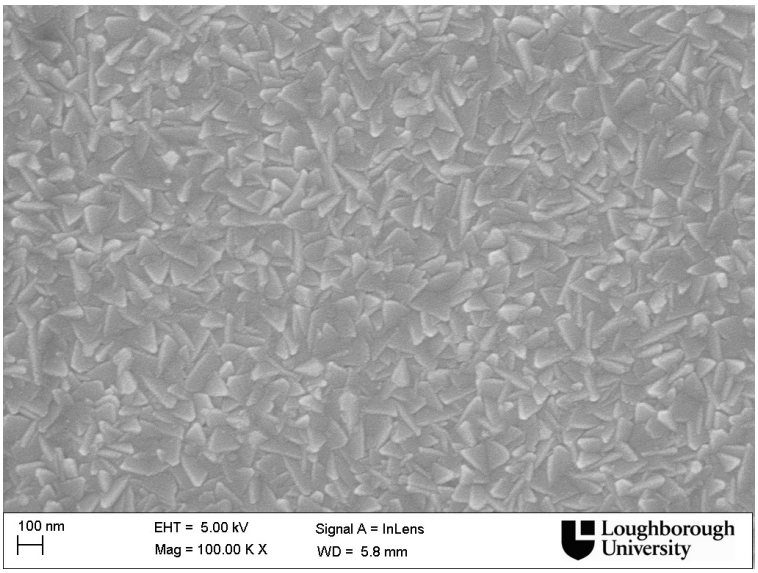

(a) 1 mTorr

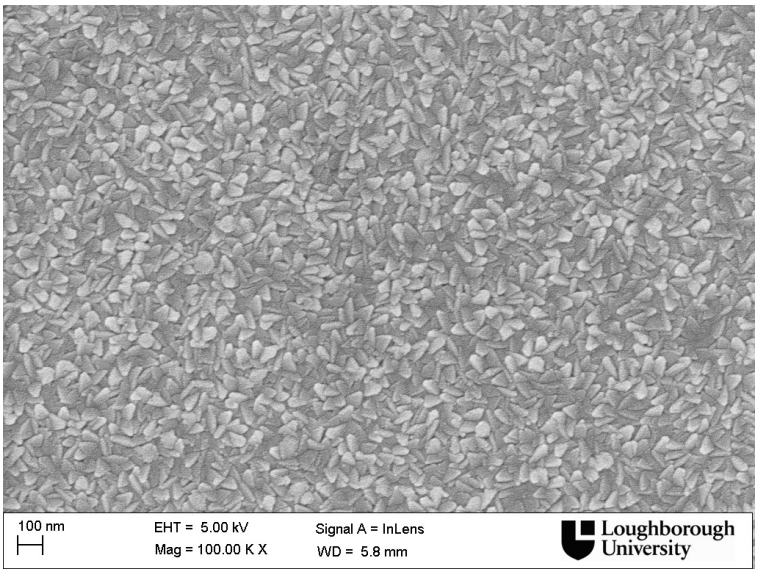

(b) 5 mTorr

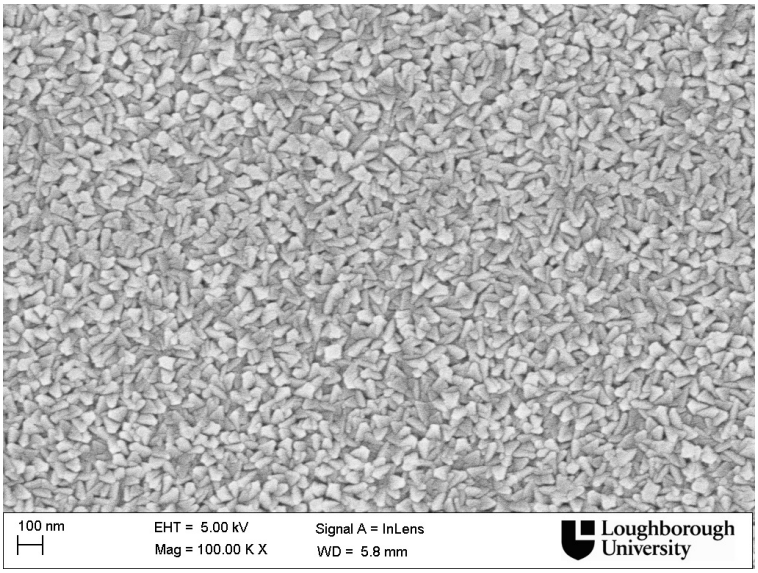

(c) 10 mTorr

Figure 4.6: Scanning electron micrograph images of ITiO films deposited at (a) 1 mTorr, (b) 5 mTorr and (c) 10 mTorr with a PDC power supply.

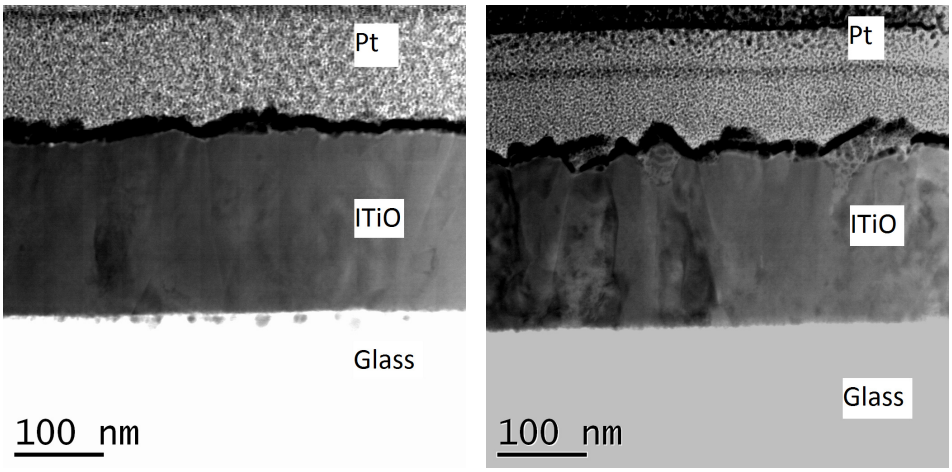

(a) 1 mTorr (b) 5 mTorr

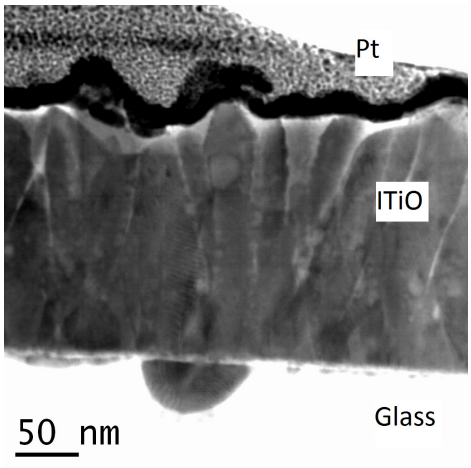

(c) 10 mTorr

Figure 4.7: Scanning transmission electron micrograph cross section images of the ITiO films deposited at (a) 1 mTorr, (b) 5 mTorr and (c) 10 mTorr by a RF power supply.

From looking at the PDC film cross sections it becomes apparent that the use of a pulsed DC power supply does indeed produce differences in the crystal structure when compared to RF deposited films, particularly at lower working pressures. This confirms the XRD patterns seen previously, where the RF has a preferred orientation in the (222) plane. The grains in the PDC film appear to be in a more random orientation when compared to the RF films, as this occurs so does the size, where the columnar grains are more narrow. This may explain the slight reduction in mobility.

As these ITiO substrates are intended for use with dye-sensitised solar cells they must be suitably resilient to the thermal and chemical processes used during fabrication. Iit is unlikely that the slight differences in crystal structure will affect the resilience of the ITiO film to these processes, it may change the adhesion of the TiO_2 semiconductor layer to the ITiO surface. Tin oxide has been successfully used as a buffer layer to increase the adhesion of TiO_2 to the substrate, however the change in orientation and structural differences may possibly require further optimisation for the PDC ITiO films. As a result an ITiO film was deposited each for the RF and PDC

power supply at a working pressure of 1 mTorr. This sample was however deposited to a thickness greater than 200 nm, to deliver an appropriate sheet resistance for use in solar cells. From the equation given previously, we can estimate the thickness required to produce a film with a desired sheet resistance, by $t = \rho/\mathrm{R}_{sheet}$

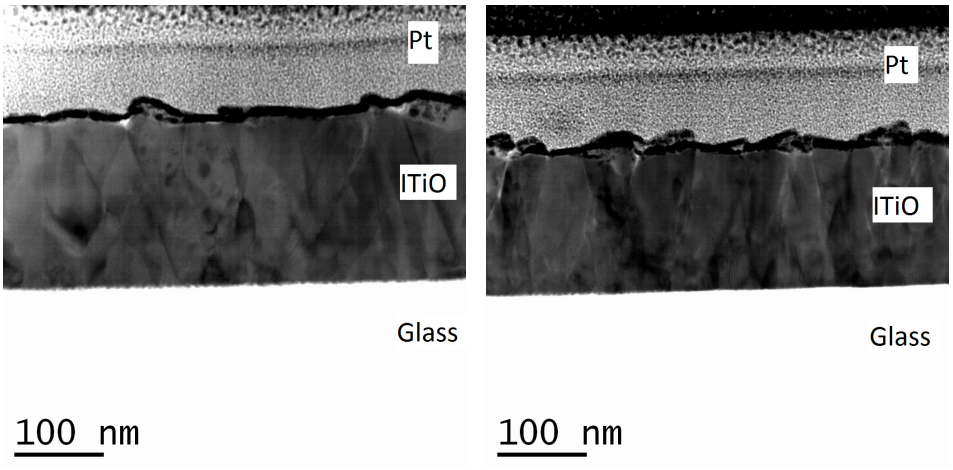

(a) 1 mTorr (b) 5 mTorr

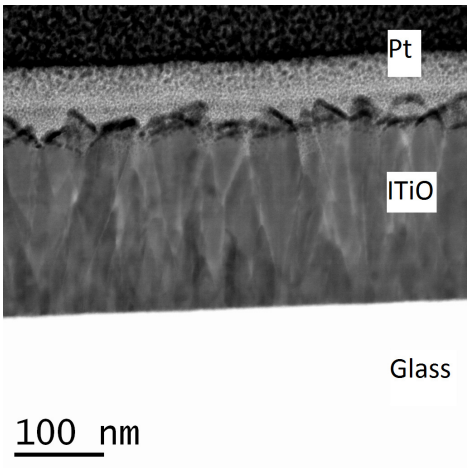

(c) 10 mTorr

Figure 4.8: Scanning transmission electron micrograph cross section images of the ITiO films deposited by a PDC power supply at (a) 1 mTorr, (b) 5 mTorr and (c) 10 mTorr. An increased working pressure leads to a greater amount of crystal grains with a greater frequency of pinholes. Compared with the RF deposited 1 mTorr ITiO film the 1 mTorr PDC film appears to have poorer crystallinity and may explain the reduction in electrical performance.

Dye-sensitised solar cells were deposited onto ITiO substrates as detailed in the experimental methodology chapter, with slight modification. To prevent delamination of the TiO_2 electrode, a 100 nm thick layer of SnO_2 was deposited immediately after the deposition of the ITiO films. The ITiO films were deposited separately and measured to check the required sheet resistance and film thicknesses were correct. The ITiO films were both cut into 2.5 x 5 cm pieces and placed in the chamber together for the SnO_2 deposition. This ensures that the SnO_2 layer is uniformly deposited to the same thicknesses for both ITiO films. The SnO_2 films were deposited in a similar method to that reported previously [104].

Following the deposition of a 100 nm layer of SnO_2 the substrate is then ready for the DSC fabrication process. Tandem DSC/CIGS devices require a higher transmission of light in the near-infrared which renders the light scattering layer often employed in DSCs detrimental to the performance of a completed tandem device. As a result the TiO_2 layer was only deposited using the transparent TiO_2 paste and to a thickness of 8 μm.

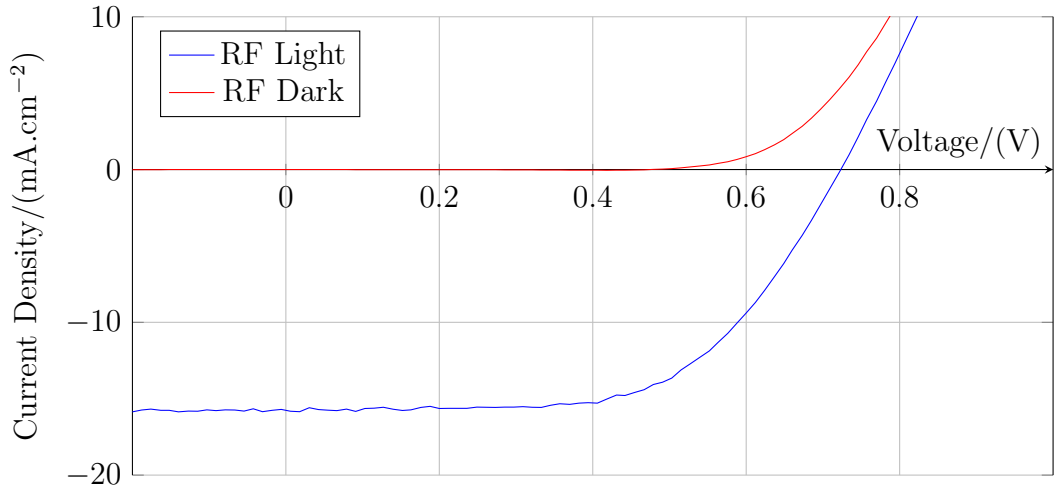

(a)

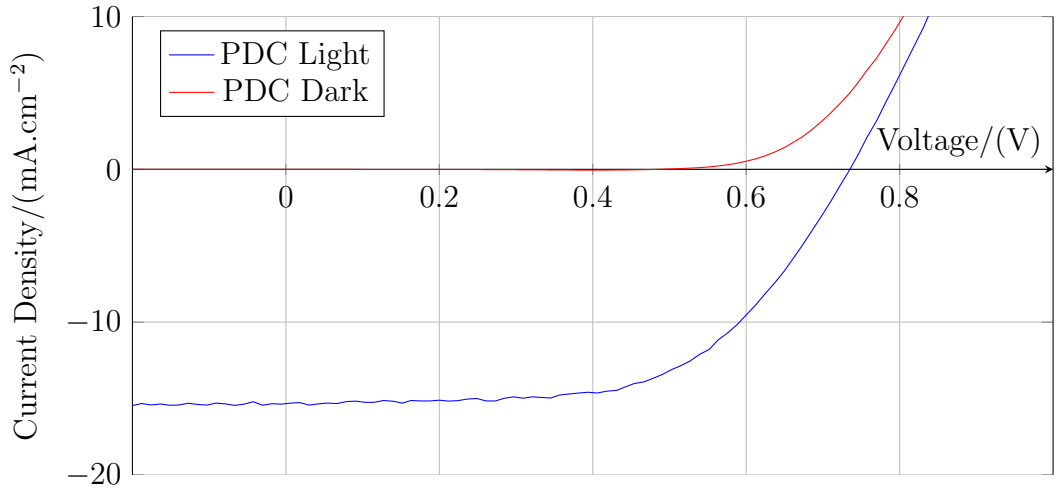

(b)

Figure 4.9: I-V curves for DSCs fabricated on ITiO deposited by (a) RF and (b) PDC power supplies. All DSC electrodes were screen printed with a mesh diameter of 6 mm and a total area size of 0.28 cm^2.

The I-V curves of the DSCs fabricated on the ITiO/SnO_2 substrates can be seen in Figure 4.9 and the characteristics are tabulated in Table 4.4. Although there is a marginal difference in efficiency between the two sets of devices, it can be observed that ITiO deposited by either method will produce solar cells of equivalent performance.

Table 4.4: Device parameters of DSCs fabricated on both RF and PDC deposited ITiO films (13A0314 and 13A0337 respectively).

	RF DSC	PDC DSC
V_{oc}/(V)	0.72	0.73
J_{sc}/(mA.cm^{-2})	15.7	15.3
FF/(%)	60	58
Efficiency/(%)	6.8	6.6

4.4 Conclusion

High mobility TCOs such as ITiO could be vital in developing tandem DSC/CIGS solar cells and other tandem technologies. The success of these technologies depends upon their cost and efficiency, so that it is crucial that each part of the device be optimised. This chapter has demonstrated that ITiO may be deposited at faster rate using a pulsed DC power supply over an RF power supply. This faster rate appears to have no trade off, as the ITiO layers have comparable performance to the RF deposited ITiO films, even when incorporated into a DSC solar cell. Slight differences appear in the crystallites of the pulsed PDC film, but these appear to have no affect on the film performance. Pulsed DC sputtering is a much cheaper option than RF sputtering and it is already widely used. As a result ITiO films may be deposited more cost effectively and on a larger scale, given that it is compatible with sputtering by this technique.

Chapter 5

THE MONOLITHIC DYE-SENSITISED/Cu(In,Ga)Se_2 TANDEM SOLAR CELL

5.1 Introduction

In order to produce a solar cell capable with efficiencies higher than the Shockley-Quiesser theoretical limit, two or more cells with different band gaps must be combined to form a multi-junction solar cell. Currently the most efficient devices to date employ this architecture (InGaP/GaAs/InGaAs) but are also amongst some of the most expensive. Silicon solar cells have so far dominated the PV market for several reasons, but one of the most important of these is their high efficiency relative to their cost. As with any industry, new methods to reduce the cost of manufacturing have been sought. This has delivered several novel methods which often emphasise non-vacuum techniques, either to compliment vacuum techniques for an existing technology (such as hydrazine deposited CIGS) or to stand alone (such as DSCs). These non-vacuum technique devices often have lower efficiencies relative to their vacuum counterparts, but offer the advantage of a lower production cost. Although these technologies have not been widely deployed in industry yet, the research output into DSCs since their seminal paper highlights the interest in these low cost technologies.

The incorporation of a dye-sensitised solar cell (DSC) and a Cu(In,Ga)Se_2 solar cell into a tandem device is a potential way to deliver a high efficiency, low cost solar cell. As described previously both devices can make use of non-vacuum deposition techniques whilst demonstrating efficiencies greater than 10 %. The devices on their own have a complimentary absorption overlap, which covers the range of wavelengths between 400 - 1200 nm. The DSC may also be easily tailored to suit certain operating requirements, which in a multi-junction device can require ingenuity to solve. The thickness of the TiO_2 layer can be easily adjusted, leading to a change in current density (a thicker layer results in a higher current density) and as a result transparency,

whilst different dyes may be selected to tune the absorption profile. The EQE curves of both a DSC and CIGS solar cell can be seen in Figure 5.1. An increase in bandgap (shorter wavelength) leads to a greater voltage, but a smaller current density. The same is true in reverse, a reduction in bandgap reads to a lower voltage and larger current density. As a result tandem solar cells must not only be configured with absorbers to utilise all of the available light, but must also be configured electronically to counteract the differences in voltage and current between the two separate cells. This was demonstrated using both a single DSC cell and single CIGS cell, which were placed one atop the other and connected in series for measurement [31]. This physical stacking of the two individual devices delivered an encouraging device efficiency of 15 %. Interestingly this tandem device delivered such a high efficiency despite not having the two device currents matched. Current matching of PV devices in a series connection, both physically connected (such as cells in a module) or in a multi-junction device is paramount to high performance.

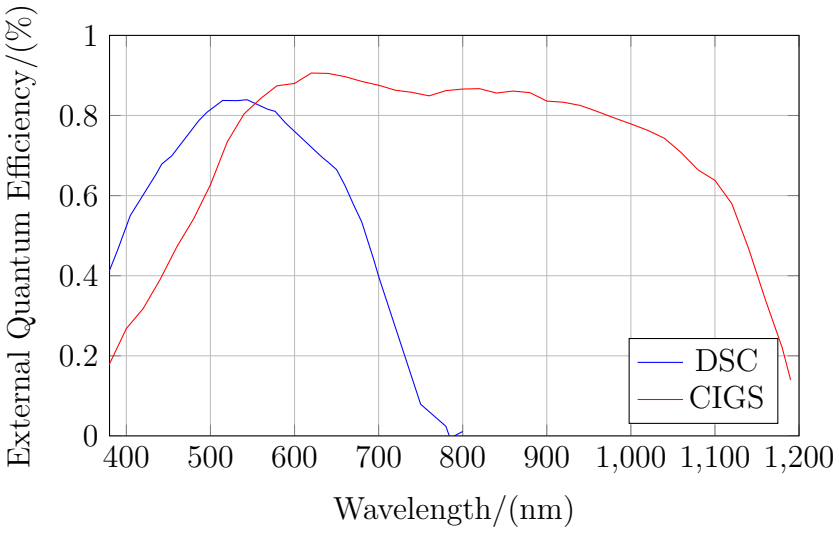

Figure 5.1: The External Quantum Efficiency (EQE) of both a dye-sensitised and $Cu(In,Ga)Se_2$ solar cell, detailing the increased spectrum absorption through the use of two absorbers.

Despite these encouraging results the described stacked tandem cell is non-optimal, using excess materials which could potentially be reduced. Replacement of the DSC counter electrode with the CIGS cell itself would eliminate the need to wire the device up externally for measurement and operation, whilst reducing the use of glass and index matching material. This would yield a monolithic tandem cell, with fewer optical losses brought about from the DSC counter electrode. This should in theory allow more light to pass to the CIGS absorber, allowing for a thicker TiO_2 layer, leading to increased photocurrent and therefore a higher efficiency [106][107]. This also requires a degree of planning prior to fabrication, as failure to current match the monolithic design could lead to a reduced fill factor, due to the 'hump' seen in the stacked tandems I-V curve [31].

5.2 Progress on a Monolithic Design

It is possible to connect two separate devices either in series or parallel, either to increase the voltage or the current. Some multi-junction devices are configured in such a way that it is possible to select either. However a monolithic device is typically configured in a series configuration, leading to a greater voltage, but requires current matching. Current matching is performed such that both cells output an equivalent current, failure to do this results in the lower performing device from determining the overall tandem performance.

Fabrication of a DSC/CIGS tandem solar cell is not too dissimilar to that of a normal DSC. Instead of sealing the DSC TiO_2 electrode and counter electrode together with the Suryln™gasket, with the electrolyte filled from a port on the counter electrode, the CIGS cell is instead used in place of the counter electrode. Other modifications are to move the fill port to the top glass substrate and to deposit a platinum layer on top of the CIGS cell prior to sealing with the DSC. Due to the temperatures used to do this using Platisol™, the layer is instead sputtered from a benchtop unit to a thickness of approx. 10 nm.

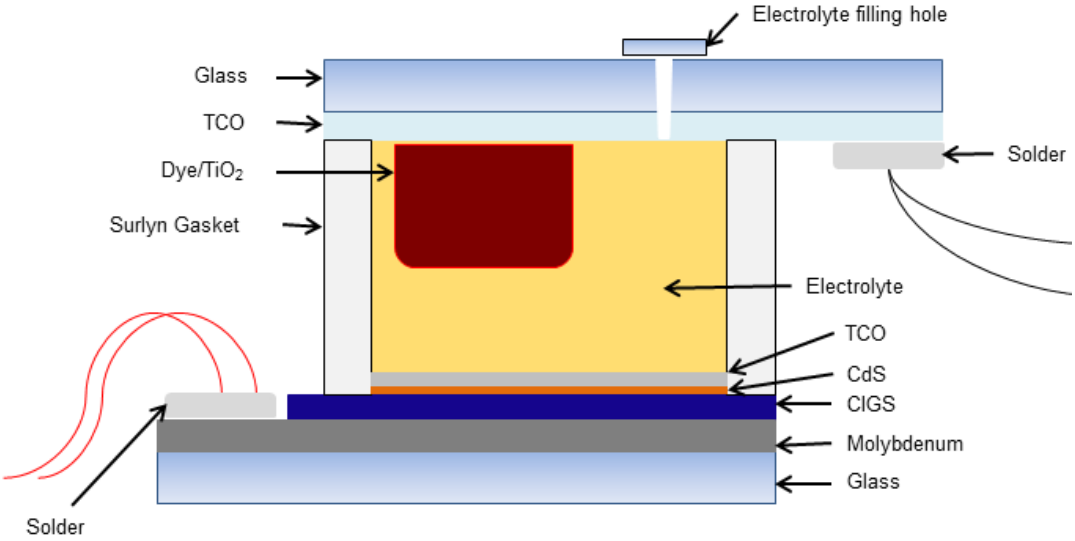

Figure 5.2: A schematic cross section of the monolithic DSC/Cu(In,Ga)Se_2 tandem solar cell.

To date the highest efficiency for a monolithic DSC/CIGS solar cell is 12.2 %, which is substantially lower than that of the stacked device considering the reduced optical losses [108]. The tandem is able to generate an open circuit voltage close to that of the two cells combined and generated a slightly lower short circuit current than the DSC. The reduction in voltage may be explained by the reduction in photons available after passing through the top cell, which is also responsible for current matching the CIGS cell. Of the two devices the DSC has the limiting current and as a result, efficiency. Because of this there is no advantage of using a high efficiency CIGS cell, such as the devices close to 20 %. To this extent CIGS devices with efficiencies in the range of 10-

12 % have been used previously, as well as in the work presented later in this chapter. These lower efficiency devices typically deliver a lower current density, fill factor and to a lesser extent open circuit voltage. However with these cells it is possible to realise a tandem cell with a greater overall efficiency than the highest performing single cell (often the CIGS cell). Although the CIGS cells used to date have been deposited by vacuum evaporation, the performance of lower efficiency CIGS devices is comparable to those deposited by non vacuum techniques.

Monolithic devices do suffer one potentially fatal drawback, in that the electrolyte used to regenerate the TiO_2 electrode and form a contact between the DSC and CIGS devices causes a breakdown of the CIGS absorber. Within several hours of the device being assembled the I-V curve begins to resemble an I-V curve of a single DSC. Further investigation found that the I^-/I_3^- species present in the electrolyte was responsible for the corrosion of the CIGS film [109].

5.3 Measurement of a DSC/CIGS Tandem Device

I-V measurements of the DSC/CIGS tandem requires some modification of what is perceived as standard operating procedures for measuring a singular DSC. Standard low-cost solar simulators matched to the AM 1.5G spectrum use a xenon arc light source. These simulators have a similar irradiance profile to the visible spectrum, which is adjusted to better fit AM 1.5 through the use of a filter. Despite this, xenon arc light source simulators have large intense peaks in wavelengths approaching the near IR, particularly between 800 - 900 nm [110]. Before any kind of measurement the simulator must be calibrated with a reference diode (which usually has been calibrated to a world class simulator, such as at NREL, AIST or FHR). This calibration places the reference photodiode in the illuminated part of the simulator and a short circuit current is displayed. The illuminated section of the simulator is able to move toward or away from the light source, to increase or decrease the light intensity. The photodiode is moved up/down until the correct, known calibrated current is displayed, which identifies that the simulator is calibrated to AM 1.5G.

The choice of reference cell for simulator calibration is important, the absorption profile of the reference cell used should be as similar to the absorption profile of the device to be measured. Typically for DSCs the reference is a silicon photodiode, which has as similar absorption profile to a DSC. However this reference cell does absorb in the region of the xenon arc peaks not defined in AM 1.5G between 800 - 900 nm. As the calibration of the simulator would take these peaks into consideration and the DSC is unable to absorb them, it is necessary to have a cut-off filter on the reference cell when calibrating the simulator. This ensures that the irradiance is a realistic representation of that which a DSC can absorb, leading to a more accurate measurement. This I-V measurement can then be corroborated with an EQE measurement to check the current density output for the device is similar, to confirm the accuracy of the solar

simulator.

DSC/CIGS tandem cells are measured in a similar fashion to that of CIGS cells, which use a solar simulator calibrated without a cut-off filter. If a DSC were to be measured on the simulator calibrated to (a) the normal reference and (b) the IR cut-off reference we would see a DSC with a lower current and efficiency in (a) than in (b). As a result this would mean that a tandem solar cell, which is limited to the current of the lowest performing absorber (the DSC), would have an overall reduced current. If the IR cut-off calibration were to be used, the current in the CIGS device would also increase, potentially causing current mismatching. An ideal solution would be to use a dual source solar simulator, which uses both a xenon and halogen light source to better replicate the AM 1.5G spectrum. Unfortunately these simulators are not as common as xenon simulators and as a result has not been used in the work presented in this thesis. Given the inherent instability of DSC/CIGS devices, it was not possible to send any working devices for characterisation at other laboratories.

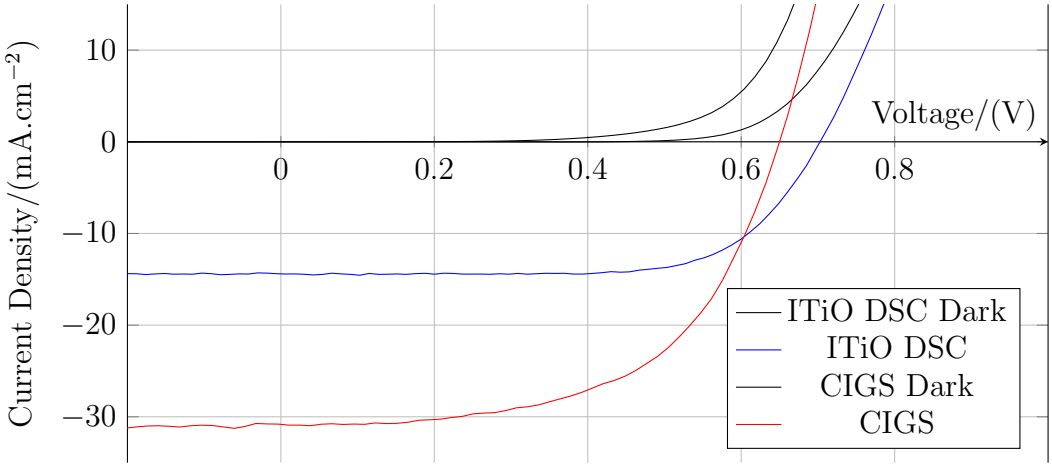

Figure 5.3: I-V curves of the single DSC finished with a typical FTO counter electrode and a CIGS device.

Table 5.1: Comparison of the performance of a typical DSC using fluorine-doped tin oxide as the TCO, a DSC using ITiO as the TCO and a CIGS solar cell. Light scattering layers were used in both DSCs.

	DSC (FTO)	DSC (ITiO)	CIGS
V_{oc}/(V)	0.77	0.70	0.65
J_{sc}/(mA.cm^{-2})	16.85	14.39	30.83
FF/(%)	73	69	57
Efficiency/(%)	9.5	7.0	11.5

5.3.1 Results

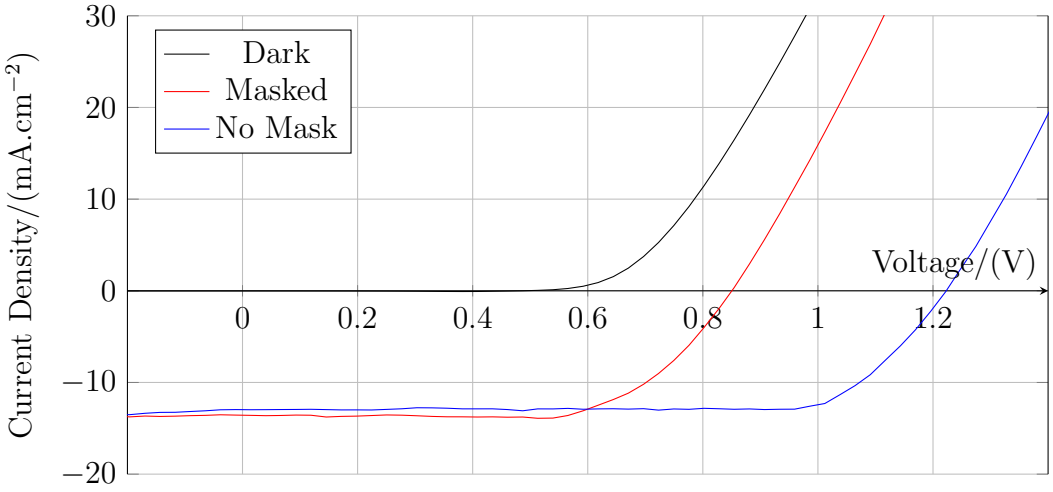

Figure 5.4: I-V curves of the monolithic tandem cell, fabricated following a reported method [108]. Two measurements are shown to highlight the differences between using a mask to measure the cell area and estimating the cell area using the area of the screen printer used to deposit the TiO_2 electrodes.

Table 5.2: Performance parameters of the monolithic tandem cell when masked to an area of 0.196 cm^2 or unmasked with the area estimated at 0.282 cm^2.

	Tandem (Masked)	Tandem (No Mask)
V_{oc}/(V)	0.85	1.2
J_{sc}/(mA.cm^{-2})	13.58	12.98
FF/(%)	67	79
Efficiency/(%)	7.8	12.4

5.3.2 Effects of Shading

In Chapter 2, the importance of masking a DSC during I-V measurements was briefly discussed. This procedure is required to accurately define the area of the DSC to a known pre-measured area of the mask. This ensures an accurate photon conversion efficiency measurement, as the cell area is required as part of the calculation. Application of this procedure to a DSC/CIGS solar cell must be continued, as the area of the DSC photoanode still may not be accurately determined prior to taking an I-V measurement.

Measurements of the tandem cells seen previously were taken immediately after the non masked measurements, prior to the onset of device breakdown. Interestingly the device sees a significant reduction in performance with the application of a mask during measurement. The primary cause of this reduced performance is the reduced voltage, which is almost 20 % less than the unshaded device. This change is not

attributed to the DSC top cell, as masking the device does not affect the device voltage, only the output current obtained. This difference in performance due to the application of an opaque mask can be attributed to the shading of the CIGS absorber layer. The effects of shading on PV systems is well documented, causing losses in both voltage and current. The effect of full and partial shading on an ideal thin film PV device (such as CIGS) can be seen in Figure 5.5. The overall shape of the I-V curve is kept fairly constant, with no changes in series or shunt resistances. To this extent the curve appears to be vertically translated to the x axis to finally represent a typical dark I-V curve when it is completely shaded.

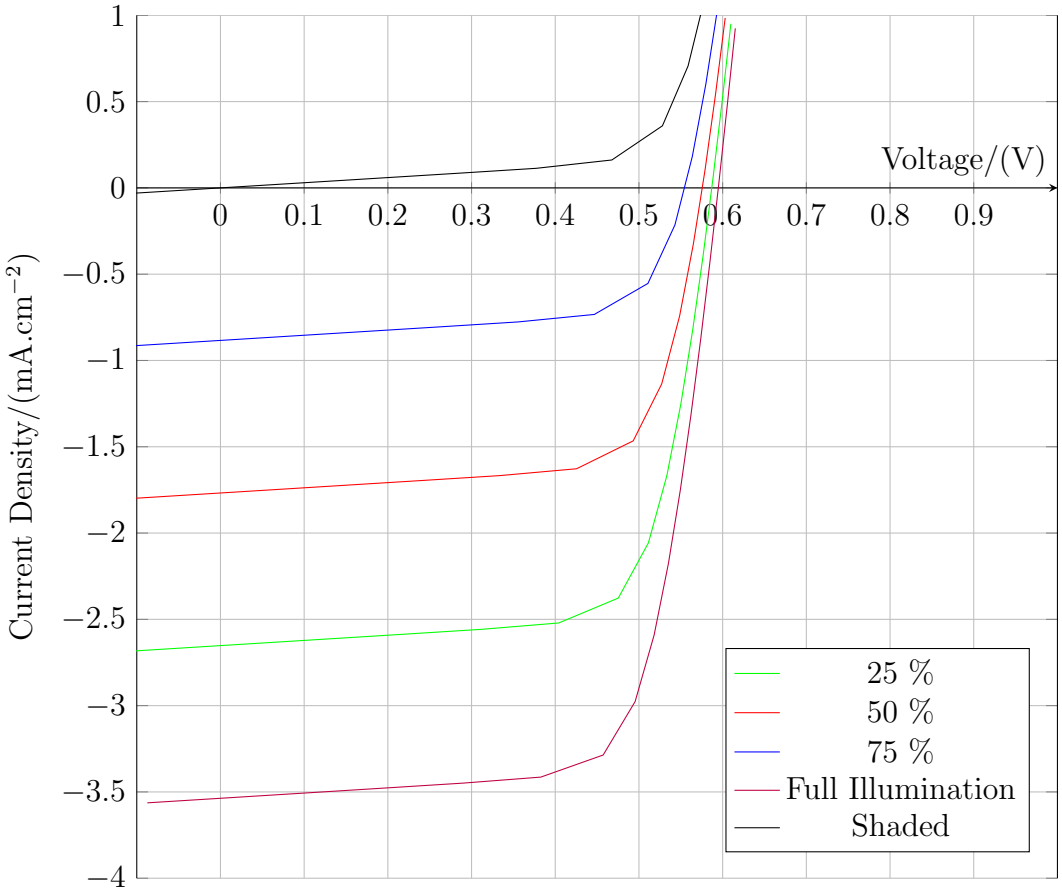

Figure 5.5: I-V curves of a modelled PV device, shaded at different percentages to demonstrate the effect of partial shading on the performance of a PV device.

This effect of the I-V curve being translated up the x axis is not seen in a DSC, instead the current output decreases as the illumination decreases, retaining the same voltage despite the amount of illumination received [43]. Currently the architecture used in a DSC/CIGS tandem is similar to a regular DSC, except the platinised FTO counter electrode is removed from the DSC and replaced with a CIGS cell. Typically the counter electrodes are cut to the dimensions with an area of 2.1 cm^2, which is significantly lower than the area (0.196 cm^2) of the mask used to measure the tandem device. However although the CIGS substrate is cut to these dimensions, a small portion must be mechanically removed to leave the bare molybdenum layer, so that

a contact may be taken from the device once assembled. Even with a portion of the absorber layer removed the CIGS layer still has an active area of approximately 1.8 cm^2.

5.4 Optimisation of Optical Parameters in the Monolithic Tandem Cell for Enhanced Performance

To reduce the detrimental effects of shading on the CIGS absorber in the DSC/CIGS device it is necessary to remove as much of the excess CIGS layer as possible. Excess CIGS is considered to be any of the layer that is not illuminated when a mask is applied to the completed tandem device. Ideally the CIGS layer would be the same area as the mask used when measuring the devices, however this would result in a CIGS cell with a smaller area than the DSC anode and gasket. This is an issue as the electrolyte from the DSC would be able to contact the bare Mo layer left from removing excess CIGS, leading to a shunting pathway in the tandem device. TiO_2 electrodes are screen printed in the shape of a circle, which requires a circular gasket. This therefore requires the CIGS to be removed in such a fashion that it is slightly greater than the gasket area. This would cause the gasket to be sealed on the top of the CIGS layer, ensuring that no electrolyte is brought into contact with the Mo back contact. A further consideration is the electrolyte filling port that is now present at the top of the device. This port must not be in close proximity to the TiO_2 electrode, otherwise the watch glass cover will obstruct the top of the device. The ideal location is far enough away from the electrode so as not to cause obstruction, however this requires the gasket to be widened to enable the port to fill the assemble cell with electrolyte. This then in turn requires a small amount of CIGS, directly underneath the relocated port, to not be removed. The modifications to the CIGS layer before assembly into a tandem device may be seen in Figure 5.6.

Modification to the CIGS layer was again carried out by mechanically removing the layer from the Mo substrate through the use of a sharp knife blade. Care was taken not to disrupt the remaining active layer, nor to damage the Mo back contact. As it is not possible to define the area needed to be removed through the use of any measurement equipment, merely to carefully etch some CIGS material off, place the gasket on top and check it will overlap and then remove any further material as required. This is quite a time consuming process and would have to be significantly simplified if a DSC/CIGS tandem were to be considered for any sort of commercial application.

Following fabrication as outlined previously with the applied modifications, I-V measurements were immediately taken with and without the use of the mask. The improvements to the I-V curve can be seen in Figure 5.7, where a marked improvement in V_{oc} can be seen in the masked device. This device is able to demonstrate a V_{oc}

Figure 5.6: A photograph depicting the modifications to the CIGS layer necessary to reduce shading losses from measurement of the DSC/CIGS tandem, whilst eliminating potential shunting pathways from contact between the liquid electrolyte and Mo back contact.

of 1.2 V, close to the sum of the two separate absorbers, 1.3 V. Both the masked and unmasked measurements show similar curves, with little differences to suggest any change in sheet and shunt resistances. Interestingly though is the difference in current density between the two measurements. Unlike the tandem device with the larger CIGS area, the small area CIGS tandem cell has a lower J_{sc} when masked than when unmasked. In addition the reduced area tandem cell has a much lower J_{sc} than that of its large CIGS area device counterpart, when both are masked. This sudden reduction in current density would seem to be brought about by the reduction in area of the CIGS absorber layer. However it is difficult to determine the uncertainty of the unmasked measurement, considering the area may be lower than predicted when calculating the current density from current measured.

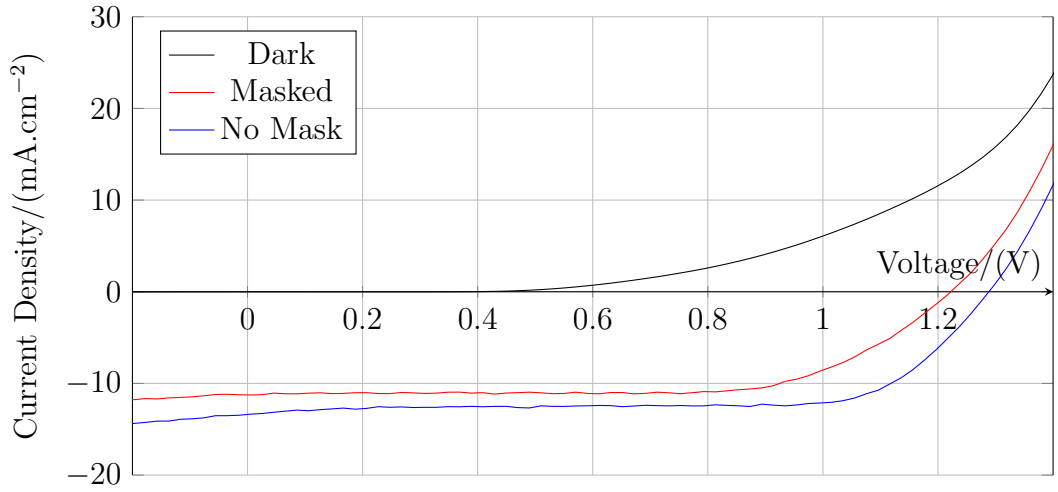

Figure 5.7: I-V measurements of the monolithic tandem device with a reduced CIGS area, measured with both the mask and without the mask.

Table 5.3: Performance of the reduced CIGS area monolithic tandem device measured with both the mask and without, detailing the similarities between both devices.

	Tandem (Masked)	Tandem (No Mask)
V_{oc}/(V)	1.2	1.3
J_{sc}/(mA.cm^{-2})	11.20	13.38
FF/(%)	67	71
Efficiency/(%)	9.4	12.3

It is possible to attribute the lower current density to several factors. TiO_2 electrodes prepared by screen printing are typically more consistent in producing similar performance devices, but requires a degree of experience and skill to do this. Even competence in this technique can lead to variance in quality of electrodes, typically responsible for higher sheet resistances and lower current densities in DSCs.

5.4.1 Improvements

Evidently there are some limitations in the current DSC/CIGS device, both in fabrication and choice of materials. Even with the reduction in area of the CIGS there is a large area still shaded during measurements. Whilst this is a practical concern for accurate measurement of the device's photon conversion efficiency, it is also using an excess of material which could be otherwise saved. Ideally the CIGS area should match that of the DSC, or even the mask used to measure the finished tandem cell. However the latter is impractical due to the inability to view through what would be the larger DSC electrode to line up the mask with the CIGS absorber. Ideally the CIGS would be deposited in such a fashion that it would match the shape/area of

the DSC electrode, however as the cells are only supplied on a 5 x 5 cm substrate an alternative solution was sought.

Two problems must be overcome to match the area of the CIGS layer to the DSC electrode, the CIGS area must be much more closely matched to the DSC electrode area using a more accurate method of removal from the substrate to further reduce shading losses and as a result there must be a solution to shunting pathways created by contact of the electrolyte with the Mo back contact. A potential solution to the shunting pathway would be to deposit a highly resistive material on the exposed Mo contact, to confine electrical contacting between the electrolyte and CIGS layer.

A candidate material is silicon dioxide (SiO_2, or silica) which is a highly resistive transparent material, which may be deposited at room temperature using sputtering apparatus. This material is typically used as an anti-reflective coating on some types of solar cell and as a result is currently used in industry. To test the suitability of silica as a resistive layer to prevent shunting pathways in a reduced area CIGS tandem device, a series of DSCs were fabricated with different thicknesses of silica deposited on their counter electrodes. The thicknesses deposited were 300, 600 and 900 nm by pulsed DC magnetron sputtering from a SiO_2 target. The I-V curves of these devices are shown in Figure 5.8, compared with a reference DSC without a silica layer.

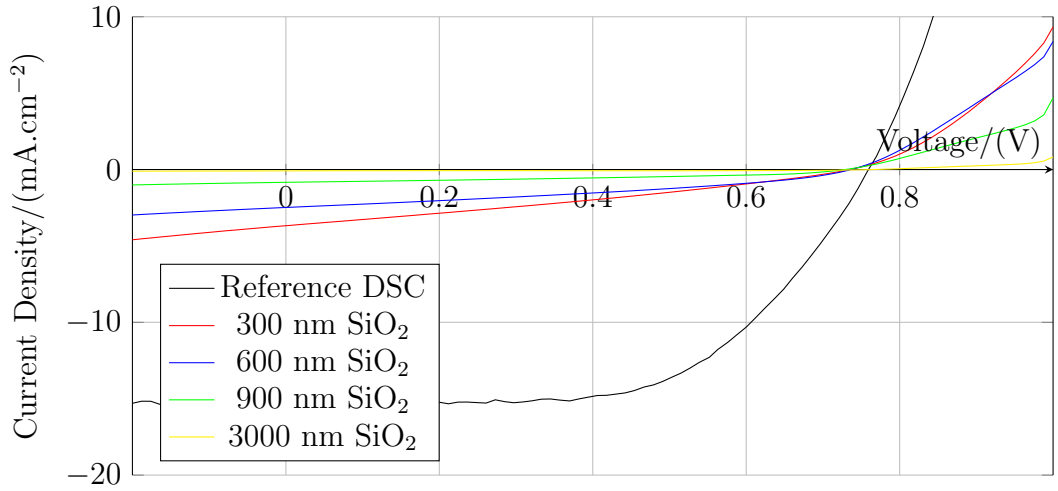

Figure 5.8: I-V curves of several DSCs fabricated with various thicknesses of SiO_2 deposited on the platinised counter electrode, detailing the resistive losses in the device.

As expected the thicker the SiO_2 layer, the greater the series resistance seen in the device I-V curve. Interestingly it takes a very thick layer of 3 microns to suppress a large proportion of the current generation in the DSC, however the device is still able to generate an open circuit voltage under illumination comparable to the reference cell. A layer this resistive should prevent a great deal of losses through the lack of shunt resistance through the Mo/electrolyte interface. Application of this approach to a working device can be a complication, as depositing this layer around the CIGS to only come into contact with the Mo requires the use of a mask. Whilst masks

are using in sputter deposition equipment, such as applying grid fingers onto singular CIGS devices.

A way in which to remove the excess CIGS whilst also then allowing the sputtering of SiO_2 was devised. The use of a self-adhesive mask was employed to cover an area of CIGS, whilst the entire substrate was submerged into a Br^-/MeOH solution. This solution is effective at etching semiconductor absorbers such as CdTe and CIGS. It was seen that application of this mask and submersion accurately etched the area required, without etching underneath the masked area. This would then allow for the transfer of the substrate into sputtering equipment to deposit the SiO_2 resistive layer. A photograph of the self adhesive masks and their application onto a CIGS substrate can be seen in Figure 5.9.

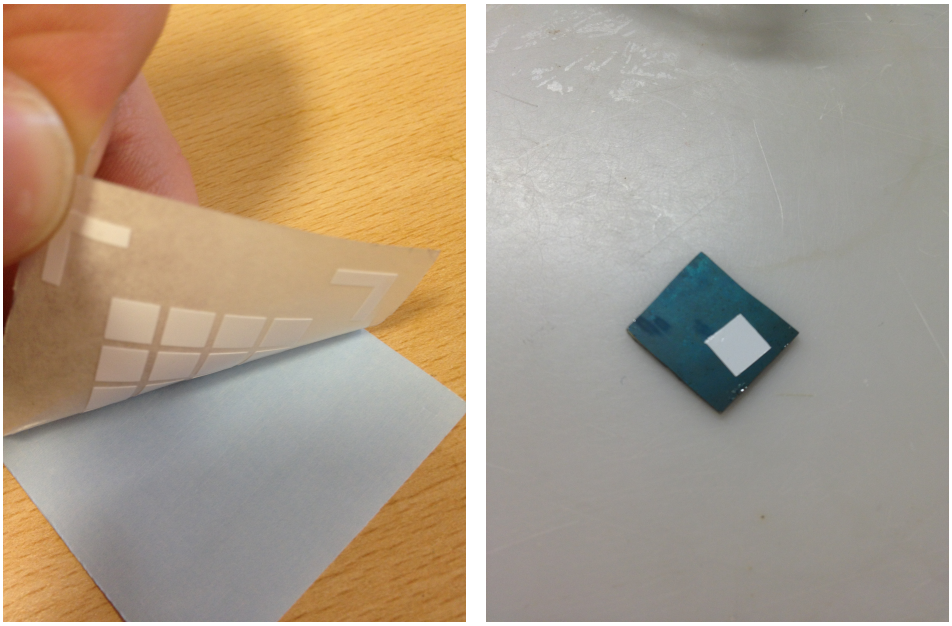

(a) The self adhesive masks used to accurately etch CIGS

(b) Applied mask to CIGS layer prior to etching

Figure 5.9: The self-adhesive mask used to etch a specific area of a CIGS absorber

Although successful at both preventing the etching of the desired area and allowing the correct application of the silica layer, the adhesive used on the mask unfortunately removed parts of the CIGS absorber as it was removed. Different approaches were taken to remove this mask with care, such as the use of solvents to weaken or dissolve the adhesive that would not further damage the CIGS, such as isopropyl alcohol. Although in its current manifestation the mask damages the CIGS layer to render it useless in a tandem device, further investigation into more suitable adhesives could potentially lead to the successful implementation of this method to fabricate a low area CIGS tandem device.

5.4.2 Potential Strategies to Eliminate Corrosion in the Tandem Solar Cell

Initial attempts to prevent or even prolong the onset of electrolyte corrosion of the CIGS layer were undertaken with the deposition of a thin 200 nm SnO_2 layer. Ultimately unsuccessful in prolonging the lifespan of the device, it has been seen previously that other materials such as ZnO has only impeded the electrolyte corrosion for at most 24 hours. Potentially the use of an electrolyte that does not contain the I^-/I_3^- redox shuttle would be the easiest to eliminate the corrosion. Many iodine/iodide electrolytes have been developed and tested, but few are able to demonstrate efficiencies close to 10 %, which is a requirement for consideration in a tandem cell. One electrolyte was used in an efficiency record holding DSC prior to the success of the perovskite based cells. This electrolyte used a cobalt based redox shuttle, but required the use of a dye with specifically tailored energy levels. Use of this dye and electrolyte in a tandem setup would require a degree of modelling to determine the CIGS absorber needed to maximise efficiency, as this dye has only been tested using a combination of transparent and scattering TiO_2 pastes.

Another method to eliminate the corrosion would be to replace the ITO/AZO layer on the CIGS cell with an amorphous TCO. Amorphous TCOs have several benefits over ITO/AZO for use in CIGS solar cells. They can be deposited at room temperature whilst still maintaining a good quality film and sheet resistance. These TCOs have already been demonstrated to work well as the top contact in CIGS solar cells, achieving comparable performance to a AZO/CIGS device [111]. The absence of any grain boundaries may prevent the electrolyte from reaching the surface of the CIGS layer, eliminating the corrosion of this layer. Application and development of such a TCO is presented in the next chapter.

5.5 Conclusion

It has been demonstrated that the accurate measurement of a DSC/CIGS tandem device requires further modifications to the tandem architecture from that presented previously. Fabrication of a DSC/CIGS tandem device at a laboratory scale with careful measurements has resulted in a loss of voltage, associated with shading losses in the tandem device. These losses in open circuit voltage arise due to unintentional shading of the series connected CIGS layer, introduced by masking the entire tandem cell during measurements. This shading was eliminated through the matching of the absorber area in both separate devices so that they were roughly equivalent. Although successful in increasing the V_{oc} the modified device did not completely match the performance of the unmasked tandem device. In addition the modified tandem device did not show as strong a J_{sc} as seen in the unmasked device.

Breakdown of the CIGS layer by the electrolyte is a serious drawback that must

be addressed if the device is to prove its potential for commercialisation. Methods to hopefully combat this corrosion have been identified, perhaps the most intriguing being the use of an amorphous TCO, which is explored in the next chapter.

Chapter 6

APPLICATION OF AMORPHOUS TRANSPARENT CONDUCTING OXIDES IN TANDEM SOLAR CELLS

6.1 Introduction

The crucial functions that the TCO in a DSC/CIGS tandem solar cell must perform are to allow a greater number of near-infrared photons into the device and to potentially act as a barrier to in-situ corrosion/dissolution of the CIGS layer caused by the DSC electrolyte. Attempts at using thin films such as ZnO and SnO_2 have proved unsuccessful, theorised that percolation of the electrolyte through grain boundaries in the TCO leads to contact with the CIGS surface. The use of an amorphous material could potentially prove effective to combat the device corrosion/dissolution, given the lack of appreciable grain boundaries. This amorphous layer would need to demonstrate the ability to not only impede the contact between the electrolyte and CIGS surface, but also not interfere with the current and voltage of the completed tandem as SiO_2 has been shown to in the previous chapter. Any alteration in the device's electronic behaviour may have unwanted side effects or even manifest as parasitic losses.

6.1.1 Amorphous Transparent Conducting Oxides

Amorphous TCOs are able to demonstrate the parameters required for application in a DSC/CIGS tandem solar cell. These materials exhibit similar properties to their crystalline counterparts however with slight differences in their electron transport. It has been shown that the transport is not band tail limited, but dependent on the ionicity of the bulk film [112]. This is due to the conduction band being derived from spherically symmetric, heavy metal cation ns orbitals with $(n\text{-}1)d^{10}ns^0$ ($n \geq 4$)

electronic configurations [112]. These relatively large atomic radii overlap with other metal cations, leading to well defined conduction pathways regardless of the bulk film structure. The formation of mixed metal oxide films should then in theory deliver conductive thin films with defect states dictating the conduction process [112].

A potential advantage over crystalline TCOs is their ability to be deposited at room temperature whilst still delivering a film capable of desired opto-electronic performance unlike their crystalline counterparts. Whilst it is possible to deposit ITiO, ITO and IMO at room temperature, higher deposition temperatures typically produce better quality films and therefore more desirable opto-electronic properties for solar cell applications [113]. The addition of the TCO as the last step in solar cell processing often requires the TCO be deposited at lower temperatures due to the inherent thermal instability of the solar cell absorber layer. For example the top contact in a typical Cu(In,Ga)Se_2 cell is ITO, this is deposited at a low or moderate temperature (not above 100 °C), as heating the unfinished device to deposit a higher quality ITO film would cause irreversible damage to the functionality of the completed CIGS device.

As a result the use and development of low temperature deposited TCOs are not limited to the application required in this thesis, they may be utilised in other existing applications.

6.2 Zinc oxide-doped indium oxide thin films

Zinc oxide-doped indium oxide (IZO) is an amorphous TCO (α-TCO), able to be deposited at room temperature from a single ceramic target or by co-sputtering from two separate indium oxide and zinc oxide targets. In a similar fashion to the way the doping concentration affects the electronic performance of a TCO, the zinc oxide concentration in the film dictates the crystallinity of the IZO film. It has been observed that co-sputtering of IZO films from intrinsic In_2O_3 and ZnO targets produces an amorphous film at a lower In at% than films produced from a single ceramic target [114]. Crystalline films result from indium concentrations of either $\leq$45 at% or >80 at % with the desired α-TCO film deposited with an indium content of 40-80% [114]. Through the use of a single ceramic target the α-TCO film can instead be produced from an indium concentration of 60-84 at % [115].

Annealing of IZO films at high temperatures in air causes a reduction in performance, similar to most indium oxide based TCOs. This will require consideration when incorporating IZO into existing procedures with DSC/CIGS solar cells, in addition it has been shown that heating IZO films in vacuum during deposition causes recrystallisation of the film.

6.2.1 Motivation

The deposition of TCOs at a low temperature is a great advantage to industrial applied thin film coating services. As previously mentioned it is possible to deposit TCOs at lower temperatures, such as room temperature, but with a reduction in opto-electrical performance. Whilst this is not ideal for optimum performance it is often employed in industry given the significant cost reduction for some applications it is also unavoidable. For example the sputtering system used in this thesis is capable of heating a 10 cm x 10 cm substrate to 600 °C accomplished through the use of two 1 kW halogen bulbs. To achieve temperatures of 450 °C used for ITiO depositions there is a 30 minute heating step to achieve the correct temperature through the use of a PID. The cost associated in upward scaling this process would incur additional costs. Commercially available TCOs are often deposited at room temperature which do not perform as highly as TCOs deposited in research laboratories.

Many previous studies concentrate on the optimisation of the ZnO:In_2O_3 ratio through the use of co-sputtering of intrinsic ZnO and In_2O_3 targets. Some have focussed on the use of ceramic single targets but have not then focussed on the application of the films deposited. For consistent results it is much easier to use a single target which was chosen for use in this chapter. Although this reduces the amount of direct control over the films electrical properties during deposition due to a lack of control over compositional changes, it requires a less complicated characterisation step, as a graded matrix does not need to be calculated for each film at each change in atomic composition. Furthermore a great deal of optimisation work has already been documented to detail the change in crystalline structure against concentration of ZnO in bulk In_2O_3 films. The target composition was chosen at 10 % wt ZnO in 90 % wt In_2O_3 using a RF power supply, as this has been the most documented and is also more readily available for purchasing, suggesting a more popular choice amongst other institutions.

Thin films of IZO were deposited to assess their suitability, first as a TCO to replace the ITO/AZO commonly used in CIGS solar cells. The transmission and electronic properties of IZO must ideally be equivalent or superior to existing ITO/AZO films. Following this the suitability as a barrier for electrolytic corrosion/dissolution of the CIGS device layer may be determined.

6.2.2 Results

Initial trials with a ceramic target proved unsuccessful in establishing a plasma at power densities, typically used for other non conducting materials. Discussion with other research groups revealed that the density of the IZO target is paramount to successful target operation. The IZO density can conveniently be identified by the colour of the target surface, a yellow surface is indicative of a lower and incorrect density that was not exactly specified by the manufacturer. A correct green surface

yields a density of greater than 95 % and will sustain a plasma to deposit useful films. The correct colour target was obtained and initial results delivered transparent, conducting films with promising performance. At the time of these initial trials most literature had been concerned with the co-sputtering of IZO from separate intrinsic targets and very little had been published regarding the trends and characteristics seen from ceramic deposited films.

To fully understand the effect of deposition parameters on the film properties, optimisation similar to that of ITiO was carried out to document the effect of temperature and pressure on the IZO films. Following the burning in of the new target an initial film was deposited using similar parameters to ITiO as a familiar starting point. The optoelectronic properties of this first film, A130038, are given in Figure 6.1.

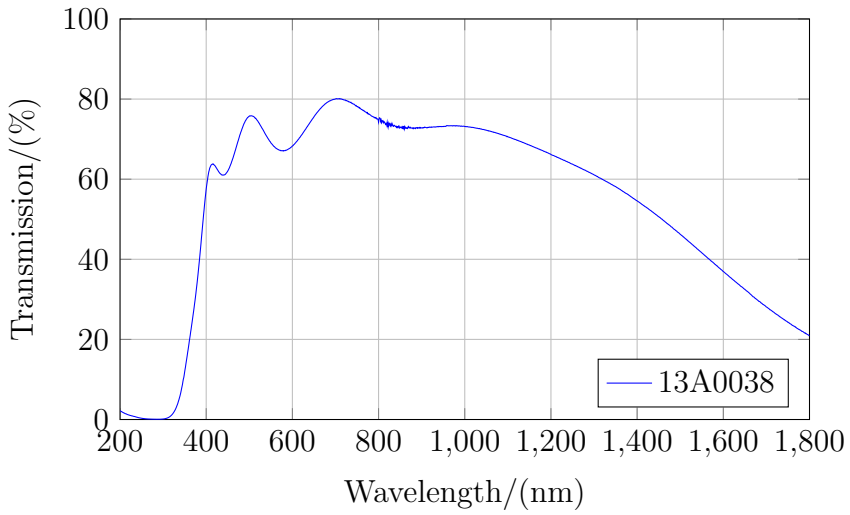

Figure 6.1: Transmission properties of the first IZO film, 13A0038, deposited from a ceramic target. The film was deposited with a RF power supply at 150 W and a pressure of 1 mTorr for 60 minutes.

Several films were deposited using these parameters to deliver consistent results. Although the transmission of the IZO film is not a vast improvement over current ITO films, further optimisation such as the addition of oxygen during deposition would increase transmission. To determine the deposition parameters required to deposit a film with optimum properties for use in a tandem solar cell a series of depositions were set up similarly to ITiO and their resulting electrical properties are summarised in Table 6.2, whilst the optical data are presented in Figure 6.2.

As has been demonstrated an increase in temperature during deposition of IZO leads to a reduced performance in both electrical and optical performance [116]. It can be seen in Figure 6.2 that transmission is reduced in the near-infrared with increased deposition temperature, further demonstrating the potential of IZO in low temperature applications. Similarly to ITiO a reduced deposition pressure also leads to a more transparent film and the same is true of an increased oxygen presence, up to 1 % v/v O_2 / Ar. Further films were deposited with an oxygen content of 10 % v/v

Table 6.1: Deposition parameters for the optimisation of IZO thin films.

Sample Name	Power Supply	Temp/ (°C)	Power/ (W)	Pressure/ (mTorr)	Deposition/ Time (mins)	Oxygen in Plasma/ (%)
13A0038	RF	RT	150	1	60	0
13A0037	RF	100	150	1	60	0
13A0040	RF	200	150	1	60	0
13A0043	RF	RT	150	1	30	0
13A0036	RF	RT	150	2	30	0
13A0044	RF	RT	150	5	30	0
13A0045	RF	RT	150	10	30	0
13A0047	RF	RT	150	10	30	0.1
13A0048	RF	RT	150	10	30	1
13A0062	RF	RT	180	1	30	1
13A0063	RF	RT	120	1	30	1
13A0065	RF	RT	120	1	60	1

, the results are not displayed as these films were very thin due to a greatly reduced rate of deposition and were not electrically conductive.

Table 6.2: Electronic parameters of all IZO films deposited during optimisation.

Sample Name	Sheet Resistance/ ($\Omega/\square$)	Film Thickness/ (nm)	Mobility/ ($cm^2.V^{-1}.s^{-1}$)	Resistivity/ $x10^{-4}$(ohm.cm)	Carrier Conc./ $x10^{20}(cm^{-3})$
13A0038	10.6	365	33.7	3.74	4.90
13A0037	9.4	360	34.0	3.39	5.30
13A0040	9.2	368	33.0	3.48	5.30
13A0043	20.4	172	40.0	3.44	4.50
13A0036	24.0	165	34.6	3.69	4.90
13A0044	28.2	143	24.2	3.91	5.10
13A0045	o/s	120	20.9	4.81	4.98
13A0047	21.0	197	37.2	4.01	4.10
13A0048	19.2	181	48.1	3.80	3.37
13A0062	16.3	212	48.0	3.64	3.50
13A0063	28.2	154	52.3	4.77	2.40
13A0065	13.9	265	49.8	3.99	3.13

Typically for AZO and ITiO an increase in oxygen content from 0 to a maximum during deposition can lead to a reduced mobility, increased resistivity and a higher sheet resistance until a peak is reached, beyond which further increasing the oxygen content will diminish the performance of the film. Interestingly for IZO this trend is identical despite the differences in crystallinity between the two material systems. The changes in temperature and pressure interestingly do not affect the resistivity of any

film to the extent of AZO/ITiO, although the carrier concentration does vary. The most influential parameter observed that affects the film performance is the power density. Increasing the power density whilst depositing crystalline TCOs typically leads to a better quality film, which was seen with ITiO in chapter 4.

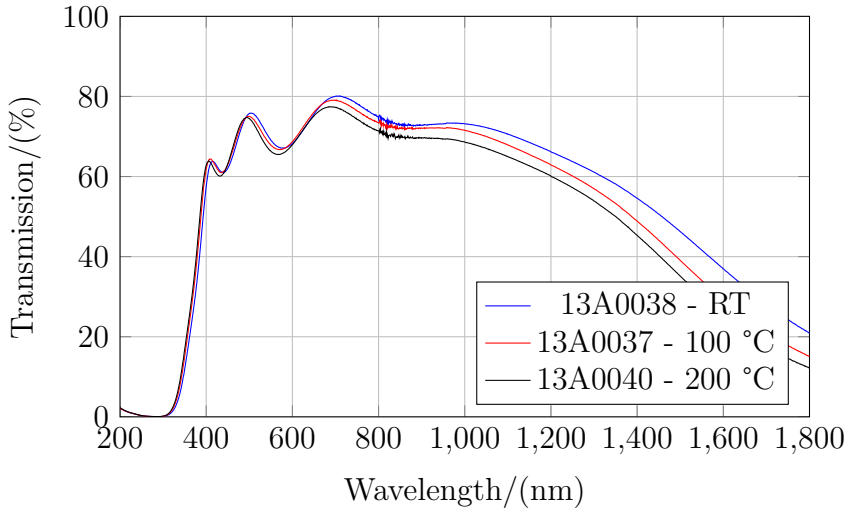

(a)

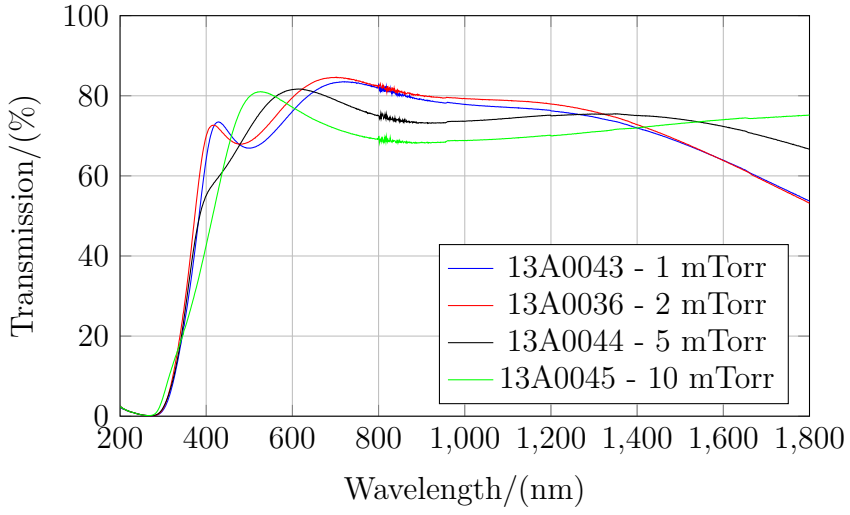

(b)

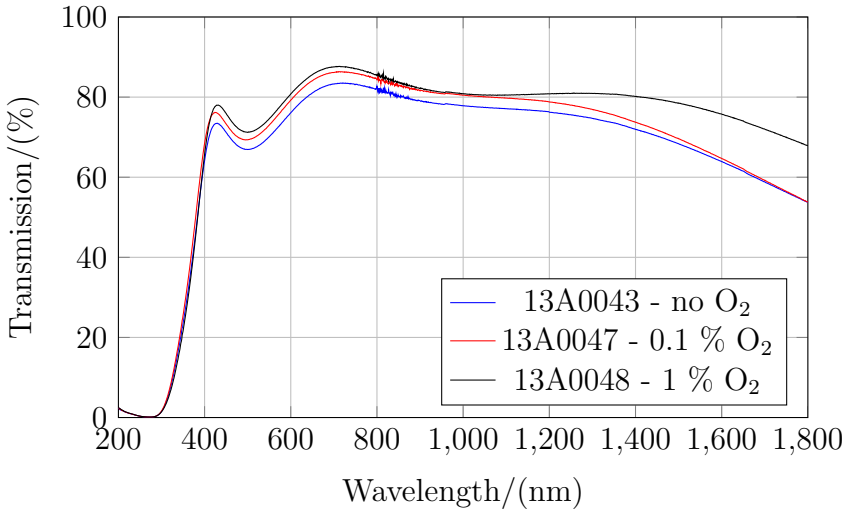

(c)

Figure 6.2: Transmission vs wavelength for all IZO films deposited during the optimisation process, with varying (a) temperature, (b) pressure and (c) oxygen concentration.

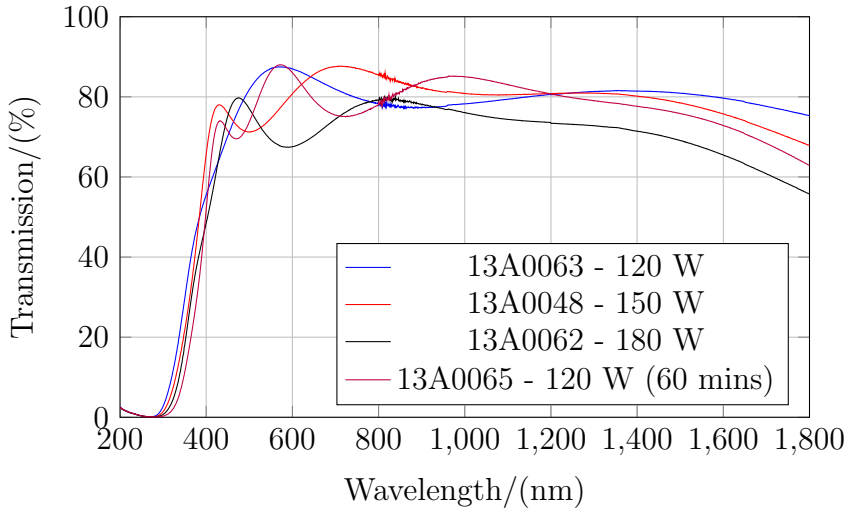

Figure 6.3: Transmission vs wavelength for IZO films deposited at varying power supplied to the target.

Relationship between the bandgap and IZO film thickness

Thicker TCO films not only have an overall reduced transmission, but the transmitted light is redshifted, which is well understood in semiconductor films as the Burnstein-Moss effect. As an increasing number of states in the conduction band are occupied by carrier electrons, the bandgap of the TCO increases, giving an apparent redshift of the optical transmission. A similar yet exaggerated effect is seen in IZO films, perhaps a result of their amorphous structure. A series of films with thickness 100, 200, 300, 400 and 500 nm were deposited using the determined optimum deposition parameters, with their electrical properties given in Table 6.3 and their optical performance in Figure 6.4a. For comparison to a crystalline TCO the transmission of varying thicknesses of AZO are also given in Figure 6.4b.

Table 6.3: Electrical characterisation of IZO thin films deposited at room temperature, 120 W and 1 mTorr.

Sample (deposition time, secs)	Sheet Resistance/ ($\Omega/\square$)	Film Thickness/ (nm)	Mobility/ ($cm^2.V^{-1}.s^{-1}$)	Resistivity/ $x10^{-4}$(ohm.cm)	Carrier Conc./ $x10^{20}.(cm^{-3})$
1200	42.3	85	54.0	3.67	3.15
2400	20.2	212	54.9	4.76	2.39
3600	13.1	308	52.1	4.26	2.82
4800	10.1	395	49.8	4.27	2.94
6000	8.3	492	61.4	4.23	2.40

As the film thicknesses of IZO increase, the carrier concentration only changes within an order of magnitude, which is less significant as that seen in crystalline ITiO films previously. The resistivity and mobility remain fairly constant, except for the

500 nm thick film which has a 20 % increase in mobility compared to the average of the other IZO films.

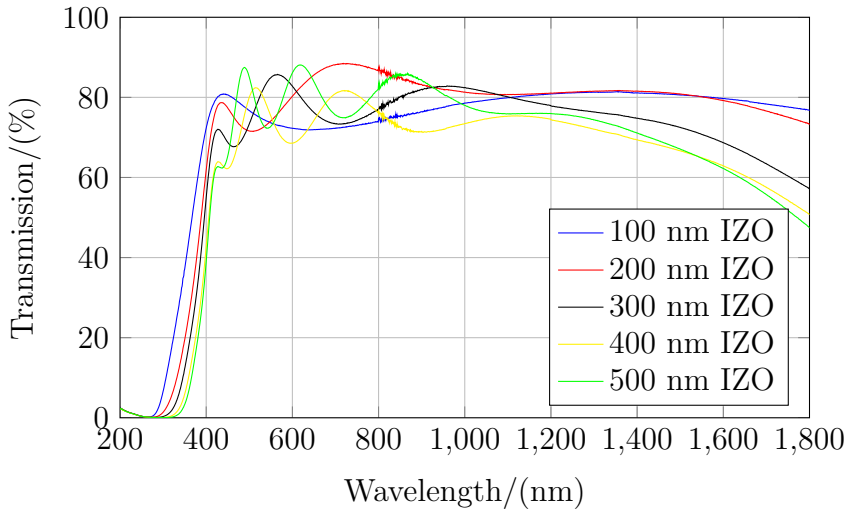

(a) %T of RF deposited ITiO

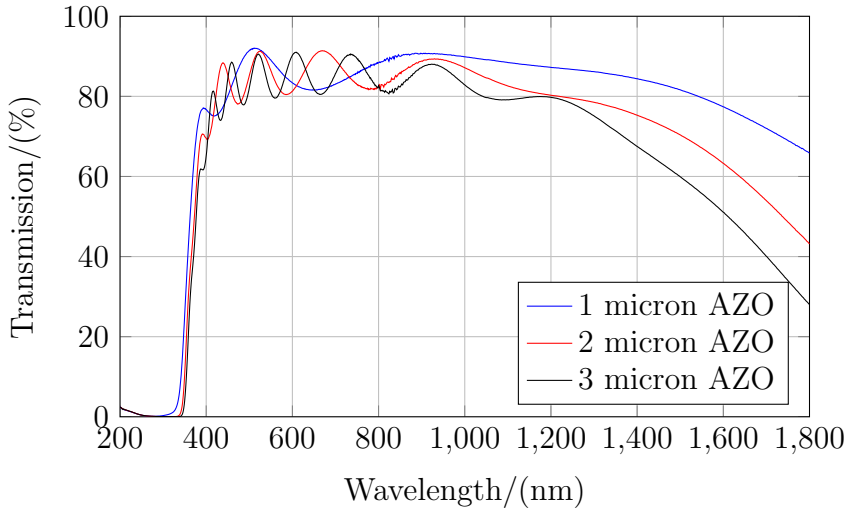

(b) %T of RF deposited AZO

Figure 6.4: Comparison of the redshift observed between the amorphous TCO, IZO and crystalline AZO with increasing thickness.

The increase in bandgap with increasing thickness is explained in amorphous films by the Urbach effect, originally documenting that an increase in temperature resulted in a redshift of absorption co-efficient when working with photosensitive AgBr emulsions [117]. It was later determined that this effect also applied to non colloidal solutions, but to disordered and ordered solids, being more pronounced in amorphous solids, expanding on Urbach's original observations [118]:

$$\alpha = \alpha_o exp^{\frac{\sigma(h\omega - E_o)}{k_B T}} \tag{6.1}$$

Where α is the absorption co-efficient, hω is the photon energy, $k_B T$ and E_o and σ are fitting parameters, with E_o proportional to $\frac{1}{K_B T}$ in Urbach's seminal paper. It

has previously been reported that it is possible for the thickness of an amorphous film to affect the optical gap of an absorbing thin film [119]. It is possible to estimate the optical gap (or band gap) from the transmission spectra of the IZO films, which are seen in Figure 6.5 using the Tauc method. It can clearly be seen that an increase in film thickness leads to a reduced band gap, causing a greater absorption of higher energy photons. This is seen in the transmission spectra, by the reduction in transmission of near UV/blue photons.

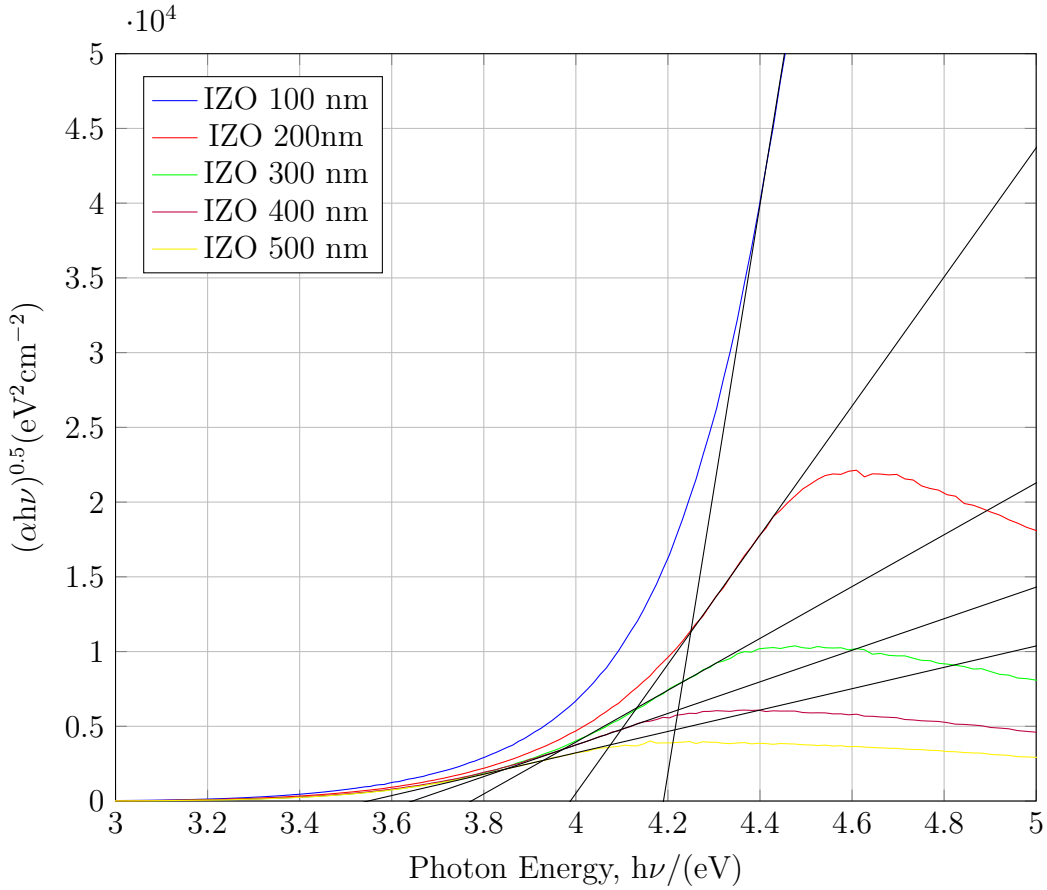

Figure 6.5: A tauc plot, calculating the band gap of the IZO films by extrapolation of the x axis intercept of the linear function for the plot of $(\alpha h\nu)^{0.5}(eV^2cm^{-2})$ vs $h\nu$.

It is already well documented that the absorption of near-infrared photons by free carrier electrons takes place in transparent conducting oxides and has been covered in this thesis by developing high mobility, low free carrier electron TCOs such as ITiO in chapter 4. However the cause of the reduced optical gap with increased temperature, detailed by the Urbach's original research is not fully understood [120]. The cause of this optical effect is generally attributed to Urbach Tails, whereby the valence and conduction bands of a binary semiconductor material become blurred, which can be seen in Figure 6.6. The typical band structure of a solid material is given on the left, with well defined conduction and valence bands. The right details the Urbach tails in blue, giving rise to the blurred conduction and valence bands described. This ultimately reduces the bandgap, but the distribution of energy states are less ordered. This effect is believed to be influenced by temperature, dopant concentration and

disorder in the structure.

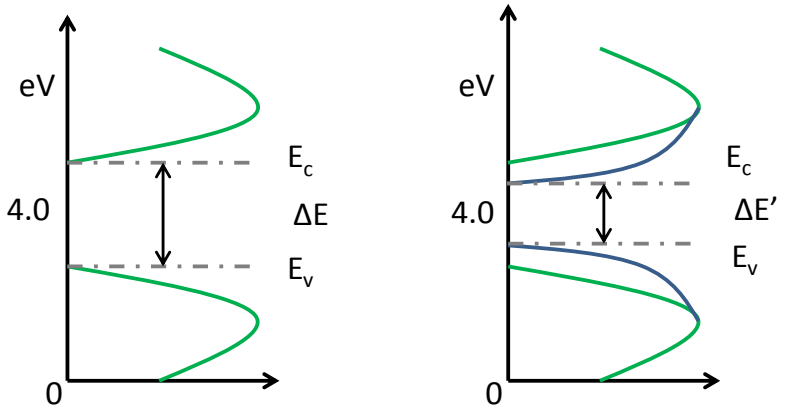

Figure 6.6: The Urbach tailing scheme, as outlined by Boubaker [120].

This reduction in transmission of near UV photons can therefore be explained by Urbach tailing, as IZO is an amorphous material. Given the array of causes of the optical gap variation this was not explored further, as it does not affect its suitability as a TCO in PV devices.

6.3 Prevention of Electrolytic Removal of CIGS in a DSC/ CIGS Tandem by Incorporating an Amorphous Transparent Conducting Oxide

6.3.1 Motivation

In a DSC/CIGS tandem solar cell the removal of the CIGS layer by the electrolyte is a major concern, requiring exploration of alternative device configurations and materials. Having speculated that the cause of the device breakdown is caused by percolation through the grain boundaries of the conventional TCOs used in CIGS solar cells, the use of an amorphous TCO could be a suitable solution. Previously a thin layer of SnO_2 and ZnO have been used in an attempt to stave off the CIGS removal, deposited by RF magnetron sputtering and atomic layer deposition (ALD) respectively[104],[109]. These methods under the right circumstances produce high quality crystalline films and as seen for ITiO in chapter 4, have the potential to deposit films with higher epitaxy. These methods and films merely slightly increased the time before the DSC/CIGS device performance was compromised. Potentially through the use of an amorphous thin film the percolation of the electrolyte through the film will

be prevented, potentially delivering stable long term operation of the tandem solar cell.

IZO has already been shown to function well as the top contact in a CIGS device, delivering comparable performance to ITO/AZO coated cells whilst also remaining stable in a humid environment, which also typically degrades CIGS PV devices [111]. The effects of humidity on the TCO layer should be quite different to that of the electrolyte, which will be in constant contact with the TCO surface during the lifetime of the device. Determining the suitability of IZO as an effective barrier to the electrolytic breakdown of CIGS has to be simplified for effective analysis. Previously the measurement of the corrosion/dissolution has been determined through the use of SEM to look for particular sites of corrosion/dissolution following the failure of the device. To simplify this analysis a substitute material to CIGS was used so that standard optical analysis could be used to track any removal of the CIGS that may have occurred.

Gold is susceptible to dissolution from the electrolyte used in DSCs, such that a thin layer (ca. 40 nm) can be etched by 1 ml of the electrolyte. The gold layer can typically be dissolved in 10-30 seconds and the colour of the gold layer makes for easier analysis using optical microscopy. The layers sputtered adhere poorly onto glass and as such a 100 nm layer of $SnO_2$was deposited onto a glass substrate prior to the gold layer to increase adhesion to the substrate.

6.3.2 Results

Initially a 200 nm layer of AZO was deposited over the SnO_2/Au stack to validate the ability to measure the dissolution of the gold layer. A much thinner AZO layer was used given the apparent mobility of the electrolyte through it. This SnO_2/Au-AZO layer was submerged in an electrolyte solution for 60 minutes and another for 120 minutes after which care was taken to remove excess electrolyte by rinsing with water, then iso-propyl alcohol. The films were then viewed under a Jeol optical microscope at varying magnification and images captured using video capture equipment.

The results from the AZO stack can be seen in Figure 6.7, which shows the extent of the dissolution that can occur through the crystalline AZO film. In the AZO films submerged for 60 mins the electrolyte appears to percolate through pinholes in the film surface, either present in the film before immersion or as a result of the dissolution process. The gold film has almost entirely been dissolved and it is only partially visible. Furthermore the AZO film has begun to crack and lift away from the surface, leading to the complete removal of gold below it. The cracks only appear directly above where the gold film originated, as seen in image (a). After 120 minutes the gold film has been completely removed from the SnO_2 surface, leaving a fractured AZO film above it. Given the dissolution rate through after 60 minutes this is to be expected and helps to highlight, yet exaggerating due to the use of another material,

the effect seen in CIGS solar cells.

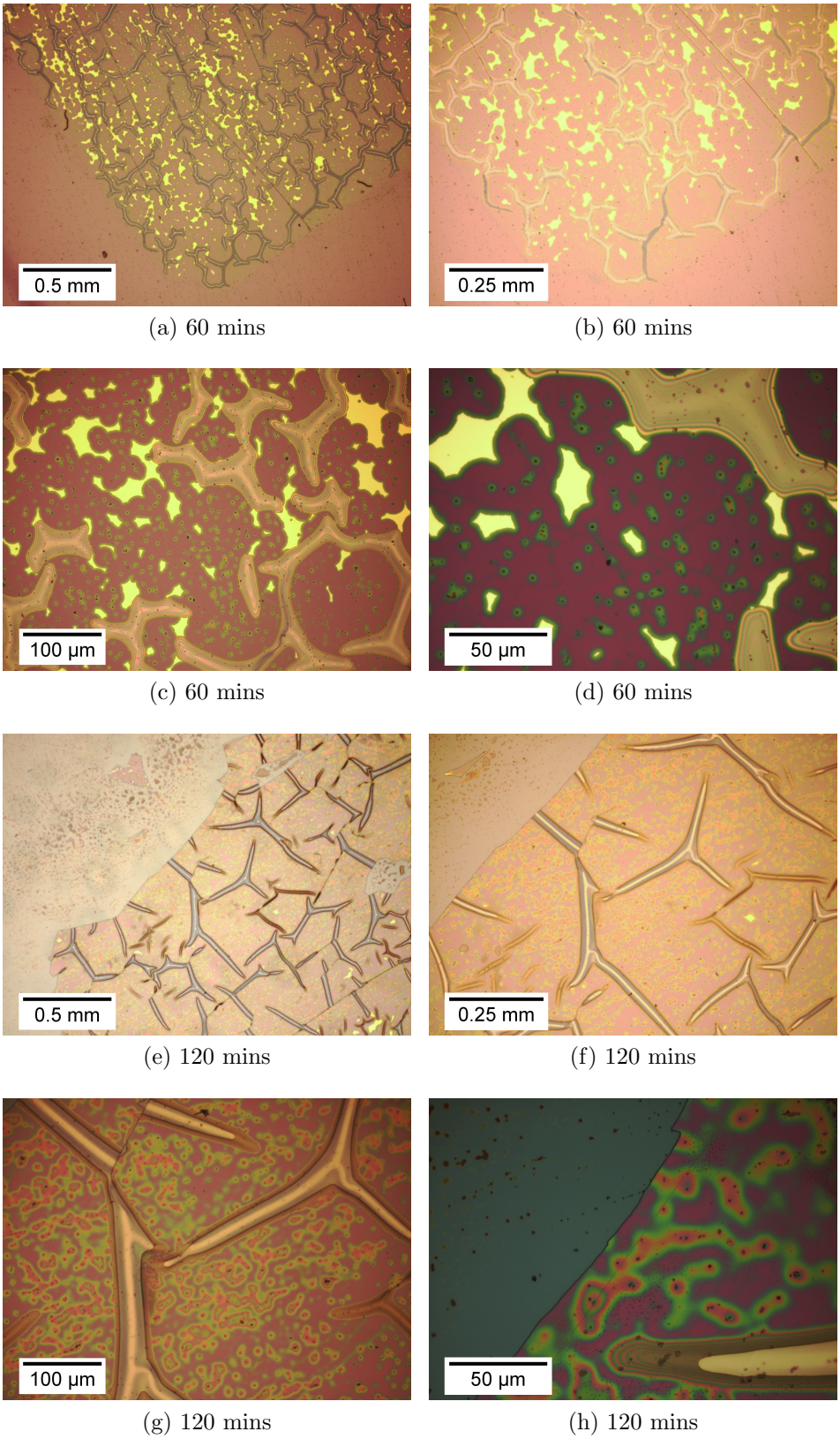

(a) 60 mins (b) 60 mins

(c) 60 mins (d) 60 mins

(e) 120 mins (f) 120 mins

(g) 120 mins (h) 120 mins

Figure 6.7: The SnO_2/Au/AZO (200 nm) stack under magnification following (a)-(d) 60 minutes immersion and (e)-(h) 120 minutes immersion in DSC electrolyte.

Increasing the thickness of the AZO layer to 1 μm gives a film closer to that typically used in CIGS solar cells. Three samples were prepared and submerged for 60, 120 and 180 minutes to investigate the effects on the gold layer and AZO film.

The effects may be seen in Figure 6.8 for all three samples. The pattern of the gold layer removal is now more easily visualised, with the dissolution sites appearing to centre around the pinholes already seen in Figure 6.7. In addition the much thicker film has not begun to crack apart, the reason for this could potentially be due to less stress on the structure as most of the gold layer is intact, it needs immersion in the electrolyte longer or simply that the thicker AZO film is not as susceptible to this effect. Zinc oxide based thin films are not typically chemically stable, with AZO able to be etched by $TiCl_4$ which is also true of IZO, which questions whether the pin holes from which the electrolyte reaches the gold film is a result of chemical action on the film surface, or are in fact intrinsic to the film due to the method of deposition.

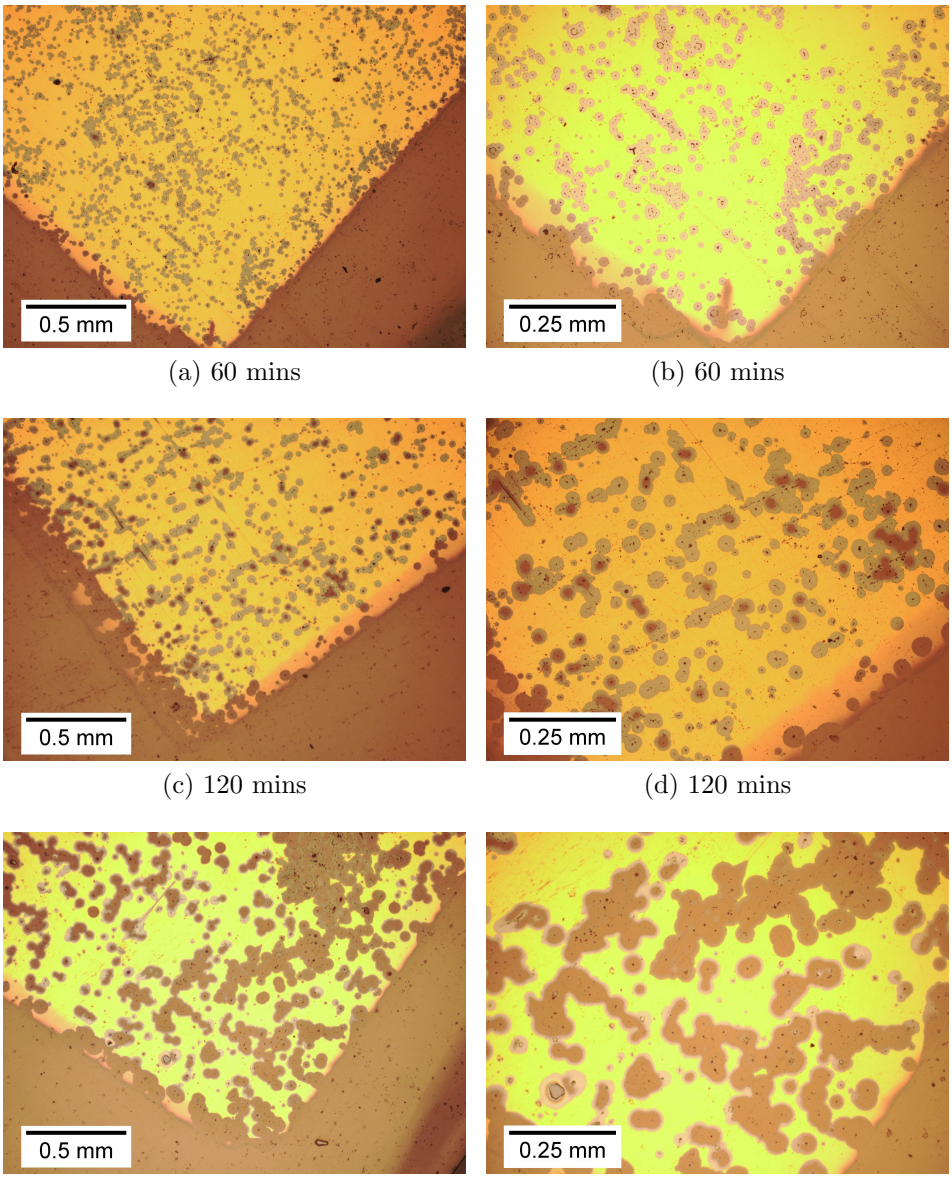

(a) 60 mins (b) 60 mins

(c) 120 mins (d) 120 mins

(e) 180 mins (f) 180 mins

Figure 6.8: The SnO_2/Au/AZO (1000 nm) stack under magnification following immersion in DSC electrolyte for: (a)-(b) 60 minutes, (c)-(d) 120 minutes and (e)-(f) 180 minutes.

To test the potential of α-TCO to prevent dissolution of the Au, IZO was deposited

onto the SnO_2/Au layer using the same parameters as those optimised for use in a tandem cell. This resulted in an approximately 200 nm thick IZO film on top of the substrate stack - SnO_2/Au/IZO. This stack was submerged into the same electrolyte solution for180 minutes, delivering similar results to the AZO film after 60 minutes. The effects of this can be see in Figure 6.9 with several pinholes present in the surface of the film, leading to removal of the gold film below, with very little left. Different to the AZO film though is the effect of the etching of the gold on the actual IZO film. No cracks were visible in the surface of the IZO film, which could suggest that the deformity of the AZO surface is caused due to stresses in the crystalline structure as the film below is dissolved.

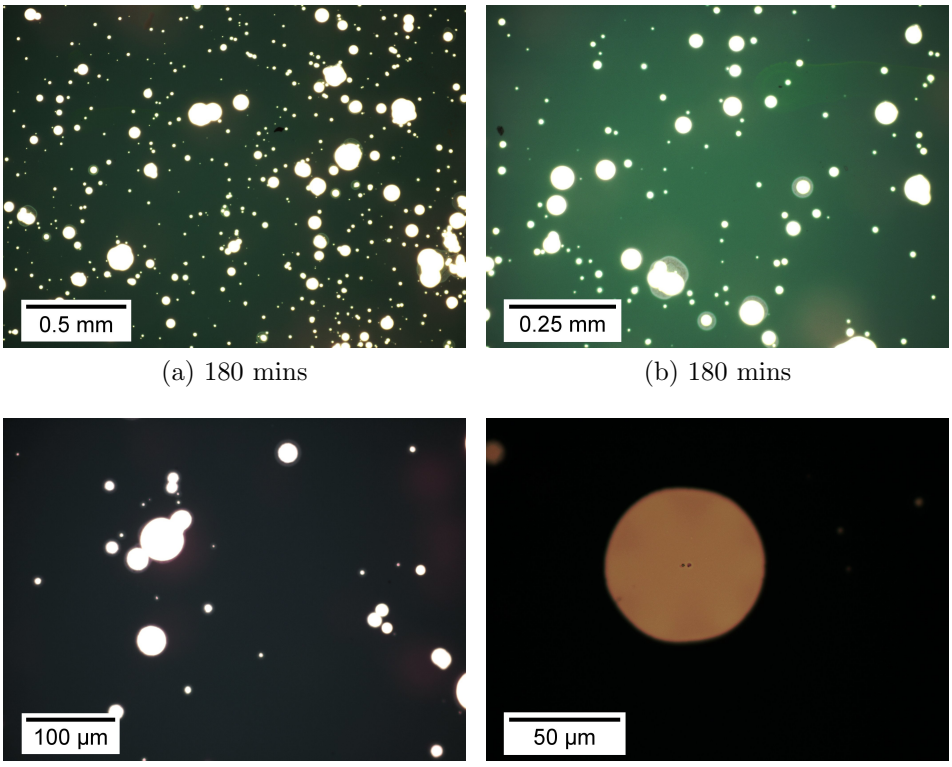

(a) 180 mins (b) 180 mins

(c) 180 mins (d) 180 mins

Figure 6.9: The SnO_2/Au/IZO (ca.200 nm) stack under magnification following 180 minutes immersion in DSC electrolyte.

From Figure 6.9d it appears that the cause of the gold dissolution is similar to that of AZO, via a pinhole in the surface of the film. This sample was particularly difficult to analyse, as there very little gold left to focus upon. A second IZO stack was deposited and submerged for 60, 120 and 180 minutes but was deposited instead to a thickness of 500 nm. The results from the thicker IZO film stack can be seen in Figure 6.10, depicting more clearly the effect of the gold removal on the IZO film. After 60 minutes the electrolyte has been able to penetrate below the IZO film in a similar way to the AZO films, via pinholes in the IZO. Curiously the dissolution pattern is dissimilar to that of AZO seen in Figure 6.8. Linear streaks where the gold has been etched are visible after 60 minutes, an alternative pathway perhaps than the pinholes. Similarly to the thinner AZO film, the IZO film begins to crack in sites of

gold removal, with this onset occurring in the 120 minutes samples. As the IZO film is thicker than the 200 nm AZO film and that this was not seen after 180 minutes in the 1000 nm AZO film, the cracking of the TCO likely occurring as a function of thickness against time.

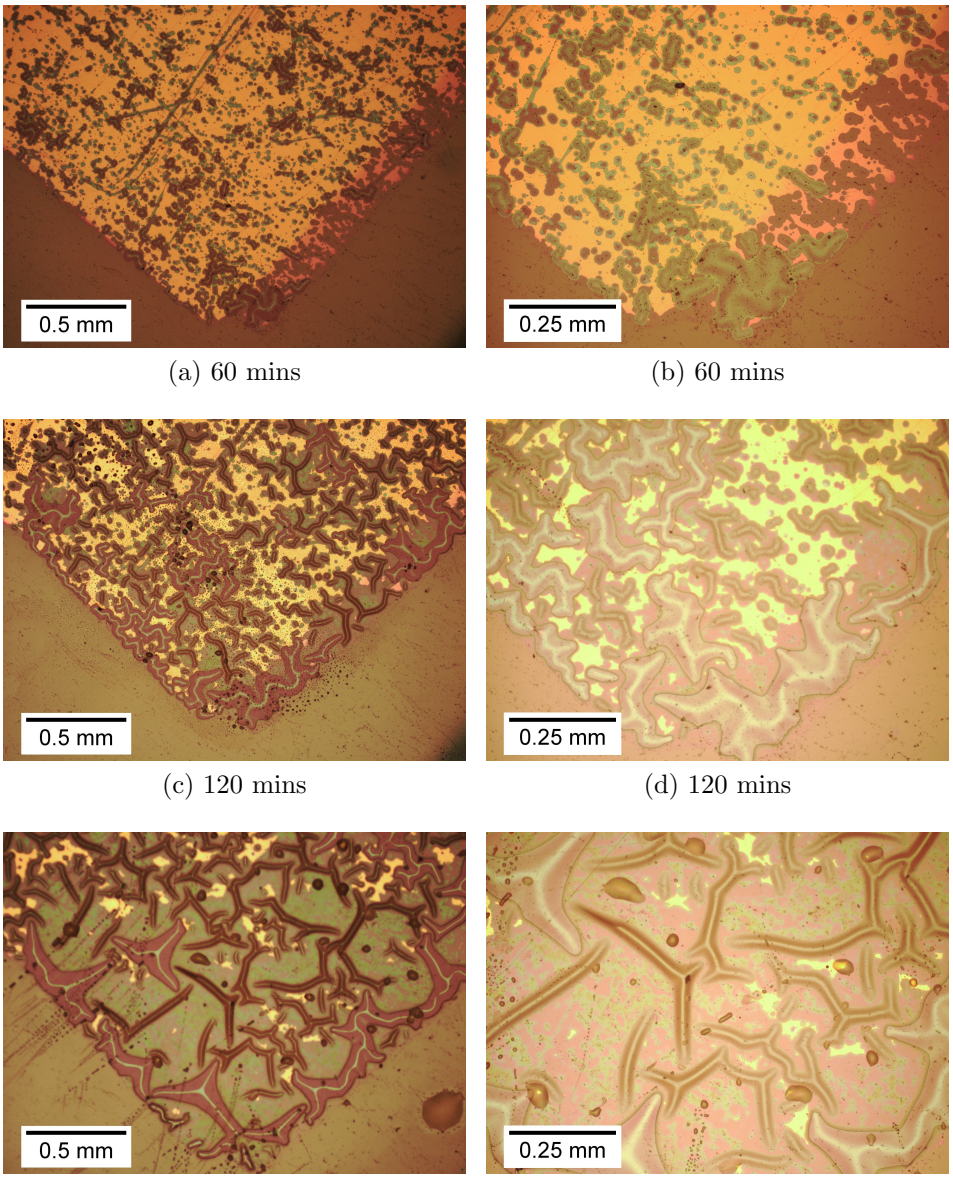

(a) 60 mins (b) 60 mins

(c) 120 mins (d) 120 mins

(e) 180 mins (f) 180 mins

Figure 6.10: The SnO_2/Au/IZO (ca.500 nm) stack under magnification following (a)-(b) 60 minutes, (c)-(d) 120 minutes and (e)-(f) 180 minutes immersion in DSC electrolyte.

Finally a much thicker layer of IZO was deposited to a thickness of 3 μm to test this hypothesis and determine whether a much thicker film was able to more effectively resist dissolution by the electrolyte. Given the increased thickness, this SnO_2/Au/IZO (ca.3 μm) stack was analysed after immersion in electrolyte for 180 minutes. The results of this can be seen in Figure 6.11. As expected the gold film has again been dissolved as a result of pathways through the IZO film. It would appear that the gold film has been dissolved at pinholes in the film. Despite this the cracks

in the films appear to be made up of a series of circular patterns resulting from gold removal, with the centre of these circles directly under the crack. It could be suggested that the gold removal occurs through the pinholes, eventually leading to cracking in the film. This pattern had not easily been identified previously in the thinner IZO or either AZO stacks.

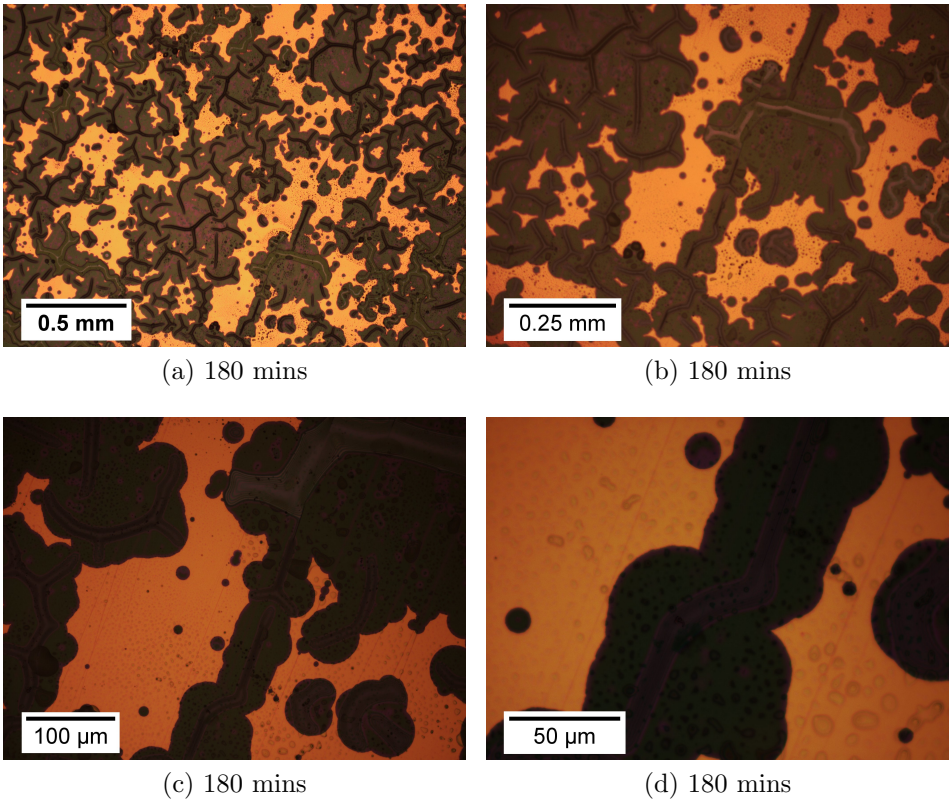

(a) 180 mins (b) 180 mins

(c) 180 mins (d) 180 mins

Figure 6.11: The SnO_2/Au/IZO (ca.3 μm) stack under magnification after 180 minutes immersion in DSC electrolyte

The subtle differences between the dissolution of the gold film from below the AZO and IZO suggests that a difference in the structures of both films may be responsible. A further stack was deposited, however a deliberate change in the structure was introduced to further attempt to prevent the removal of the gold layer. This was attempted by depositing a bi-layer of IZO, with inspiration taken from how molybdenum is deposited onto soda-lime glass. To enhance the adhesion of molybdenum to the glass substrate and reduce pinholes two layers are deposited, first a layer at a relatively higher pressure to form a layer with less crystalline stress, but more pinholes. A second layer is immediately deposited at a lower pressure, to form the higher quality film which delivers the superior electrical parameters required whilst filling the pinholes in the layer below. Without this layer the molybdenum layer can peel away from the glass substrate. ITiO deposited at varying pressures can affect the crystallite appearance and density, leading to films with different characteristics, thus the need for this method.

To form this bilayer stack, the SnO_2 and gold layers were deposited as normal. Following the deposition of the gold layer, the substrate was loaded into the AJA Orion

8 sputtering system, where a ca.200 nm layer of IZO was deposited at a pressure of 10 mTorr, followed by a run of ca.200 nm of IZO at 1 mTorr. The sample was then immersed as before in DSC electrolyte for 60, 120 and 180 minutes, the results can be seen in Figure 6.12. It is immediately apparent that this bilayer does not enhance the resistance of IZO to dissolution of the gold film, as nearly all of the gold layer is removed after 180 minutes. After 120 minutes the IZO film appears to crack in areas of complete gold removal, as has been seen consistently before. As such it can be concluded that α-TCOs do not appear to be an effective barrier to the DSC electrolyte, but are similar to their crystalline counterparts (ITO, AZO).

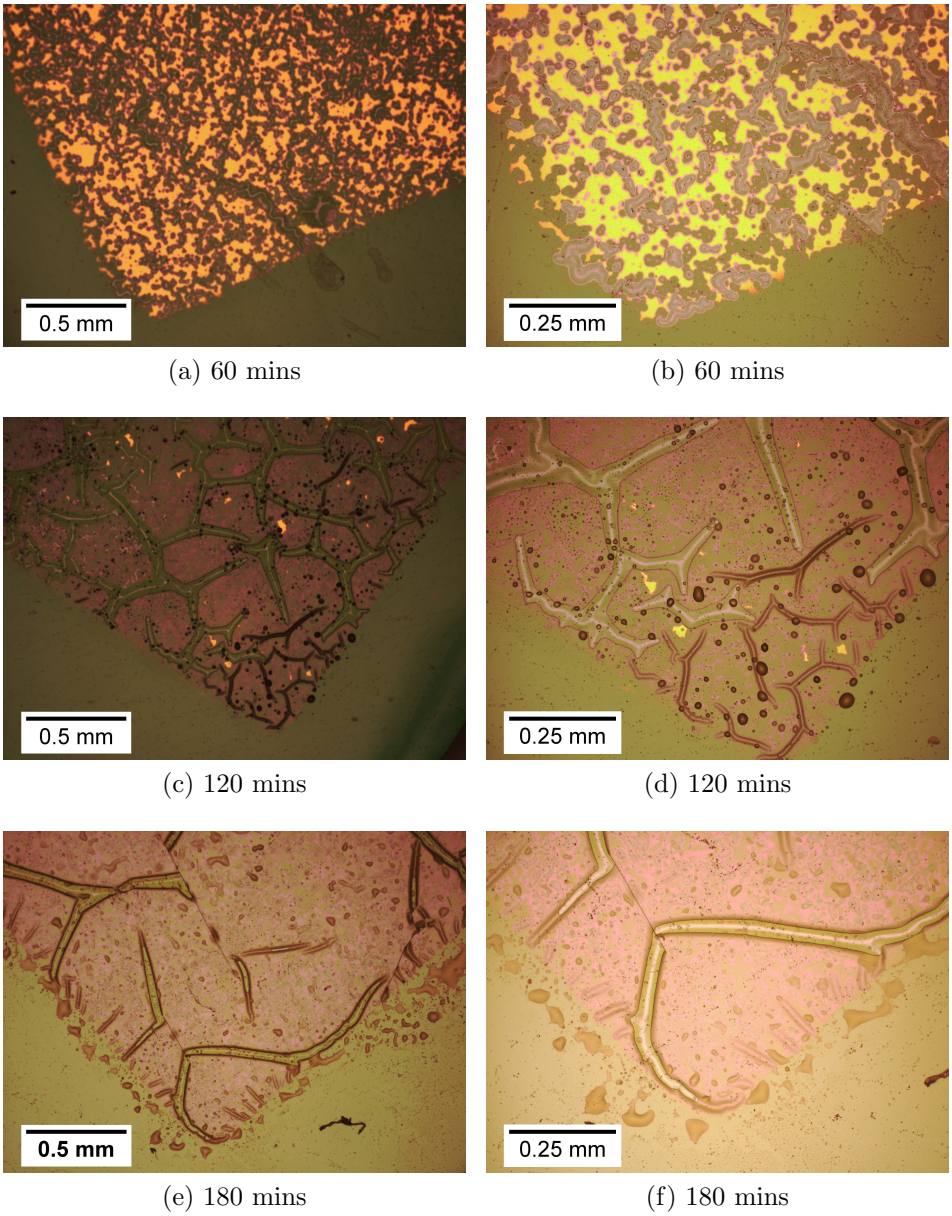

(a) 60 mins (b) 60 mins

(c) 120 mins (d) 120 mins

(e) 180 mins (f) 180 mins

Figure 6.12: The SnO_2/Au/IZO bilayer stack under magnification following (a)-(b) 60 minutes, (c)-(d) 120 minutes and (e)-(f) 180 minutes immersion in DSC electrolyte.

The susceptibility of ZnO based TCOs to chemical and thermal extremes is well documented and has been demonstrated again in this chapter. As part of a previous thesis the use of protective layers deposited on top of AZO has been demonstrated

by depositing layers of SnO_2 onto AZO at varying thicknesses, to reduce the chemical etching of a ITiO thin film by $TiCl_4$. Although the layers were typically ineffective when deposited as thin layers, thicker layers (ca. 800 nm) were able to prevent etching of the AZO film underneath [121].

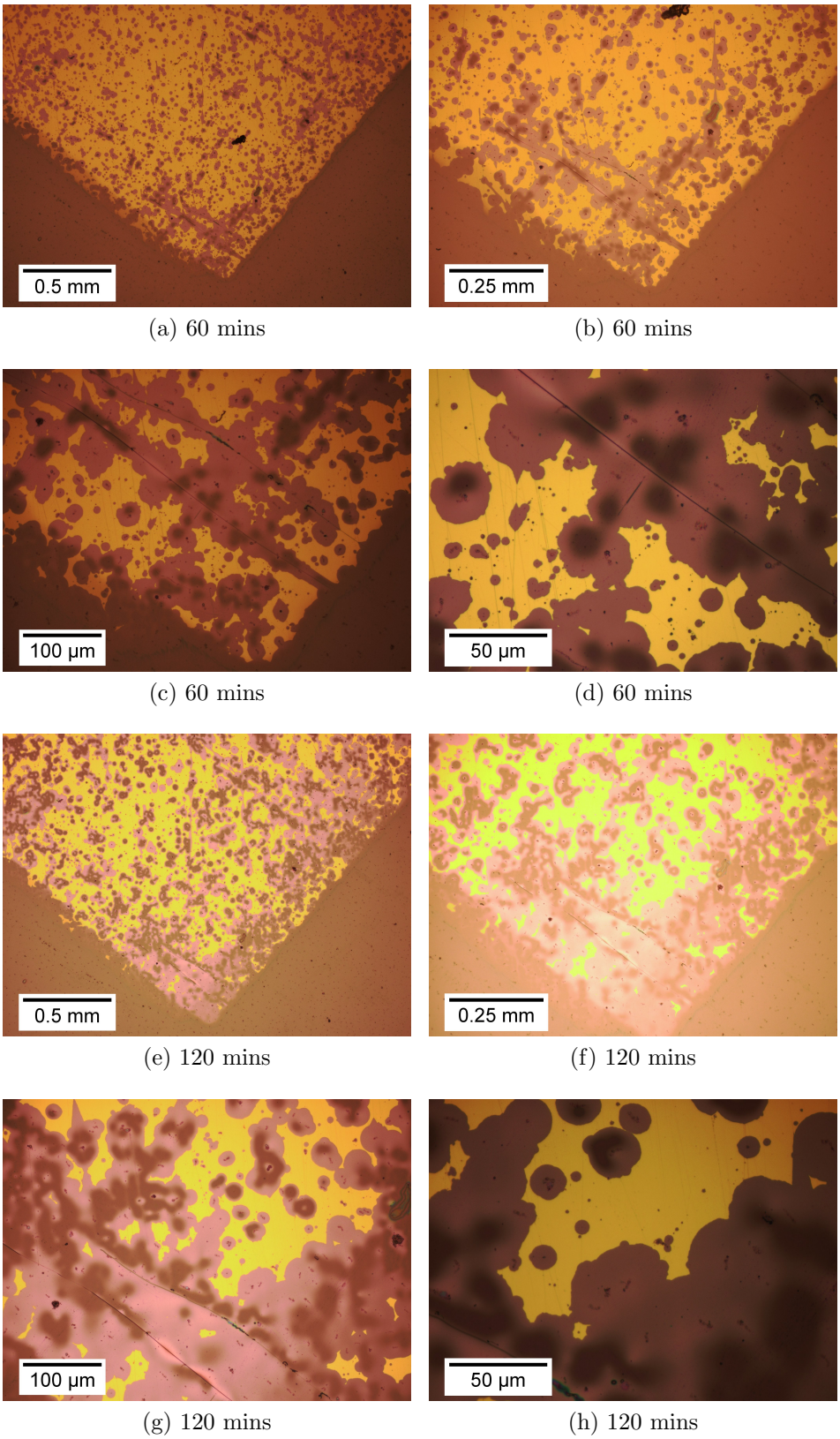

(a) 60 mins (b) 60 mins

(c) 60 mins (d) 60 mins

(e) 120 mins (f) 120 mins

(g) 120 mins (h) 120 mins

Figure 6.13: The SnO_2/Au/SnO_2 (1 μm) stack under magnification following (a)-(d) 60 minutes, (e)-(h) 120 minutes immersion in DSC electrolyte.

Given the effectiveness demonstrated by SnO_2 to prevent chemical attack by $TiCl_4$ when used as a barrier with AZO/ITiO it would be expected to perform better than that seen in Figure 6.13. The gold layer has been dissolved again in a mechanism similar to that in AZO and IZO, via pinholes in the film.

6.4 Conclusion

IZO has been shown to demonstrate optical and electrical performance desirable for use in tandem solar cells for either the top or bottom absorber layer. Additional benefits such as the possibility to be deposited at room temperature can potentially lead to performance improvements when used in place of ITO/AZO in a CIGS solar cell. Thicker IZO films exhibit a more pronounced absorption in the 200-300 nm range when compared to crystalline TCOs, due to the Urbach effect, which may limit the thickness (and therefore electrical performance) in some applications.

As a barrier to corrosion or dissolution of films deposited underneath it, it has been demonstrated that amorphous materials that are also able to fulfil the criteria of a TCO for the CIGS device is not possible. Several different materials were deposited but were unable to show any way of deterring the movement of electrolyte to the gold interface. As a further study from this it may be possible to use a hydrophobic material to prevent this passage of electrolyte through the TCO. However this would not be a trivial study and the material chosen must not remove the enhancements in transmission afforded by the use of ITiO and IZO over FTO and ITO.

Chapter 7

POTENTIAL CONFIGURATIONS OF LOW-COST TANDEM SOLAR CELLS

7.1 Introduction

Novel materials for application in solar cells, in addition to devices with a narrow absorption region (and/or low photon conversion efficiency) are often remarked as being suitable for use in a tandem solar cell. This is usually not followed up with substantial evidence pertaining to the claimed suitability or in fact any results to reinforce this statement. The complexity of tandem solar cells has been demonstrated previously from a materials aspect, although several challenges with measurements also exist. The selection of absorbing materials seems a trivial aspect in tandem devices, based solely on their respective bandgaps and EQE data. However the spectrum available to the bottom device is not always simply all wavelengths not absorbed by the top device.

Optical and electrical modelling of different absorbers/devices may be utilised to optimise a tandem configuration. The reliability of such a model is dependant on the data used and the design/complexity of the model. The DSC/CIGS tandem has been shown to demonstrate promising efficiencies when combined in a physical stack of each respective device, however when combined in a monolithic design in both this thesis and elsewhere, the same efficiency of the physical stack has been difficult to replicate. Two focus points of this difference in efficiency have been the transparent conducting oxide used in the top layer and the corrosion of the CIGS layer by the electrolyte used in the DSC.

7.2 Motivation

The highest efficiency tandem solar cells are currently the most expensive available, these find use in applications where the cost is not a consideration. Vast knowledge of III-V materials and vacuum deposition are used in addition to extensive research to the benefit of this technology. The overall device is set up to achieve a high efficiency and this is not accomplished by simply producing several absorber layers with maximised absorption in particular regions. So far the DSC/CIGS tandem has not been set up in a similar fashion, the main changes to the individual absorbers has been to remove the light scattering layer of the DSC and use a slightly lower efficiency CIGS device.

By modelling the optical parameters of the tandem device it may be possible to make modifications to enhance the efficiency of the device by methods not currently employed. This method will potentially help to increase the overall efficiency by identifying key areas of change.

7.3 Methodology

The model used to demonstrate the keys areas of focus for the DSC/CIGS tandem will be kept relatively simple, as the potential complexity (and to an extent, accuracy) may escalate into a thesis of its own. The model will simulate the effects of changing several parameters in the tandem device through the use of measured data from each of these individual layers. The DSC layer however may cause potential problems as ideally it would be possible to change the DSC thickness in the model to simulate the yield to the CIGS layer. To achieve this the DSC layer transmission and absorption must be modelled relative to its thickness, which as a mesopourous layer is not necessarily straightforward.

7.3.1 Model Design

Similar to estimating the band gap of a TCO the Beer-Lambert law may be used to describe the transmission and absorption of light through a tandem device (or any other solar absorber). Ideally reflective losses would be taken into account at each new interface layer, which may potentially be reabsorbed by the previous layer (and be re-reflected), however the fate of these reflected photons will not be taken into account or modelled further to keep the model simple, as these typically only account for less than 5 % of incident photons unless at the first glass interface.

Interference fringes are removed by using absorbance as a measure of how much light is lost through the optical stack. A model of the Glass/TCO/DSC will be compared to actual measured data of the same stack, as this is relatively simple to measure in the UV-Vis-NIR spectrophotometer.

The model should comprise of 5 layers and are listed in order of incident light: 1) Glass, 2) DSC TCO, 3) DSC absorber, 4) Electrolyte, 5) CIGS TCO which can be seen below in Figure 7.1. By examining the light available to the CIGS layer after passing through the tandem stack it may be possible to identify the optimal (In+Ga)/In ratio, rather than the standard used currently for single absorber layers.

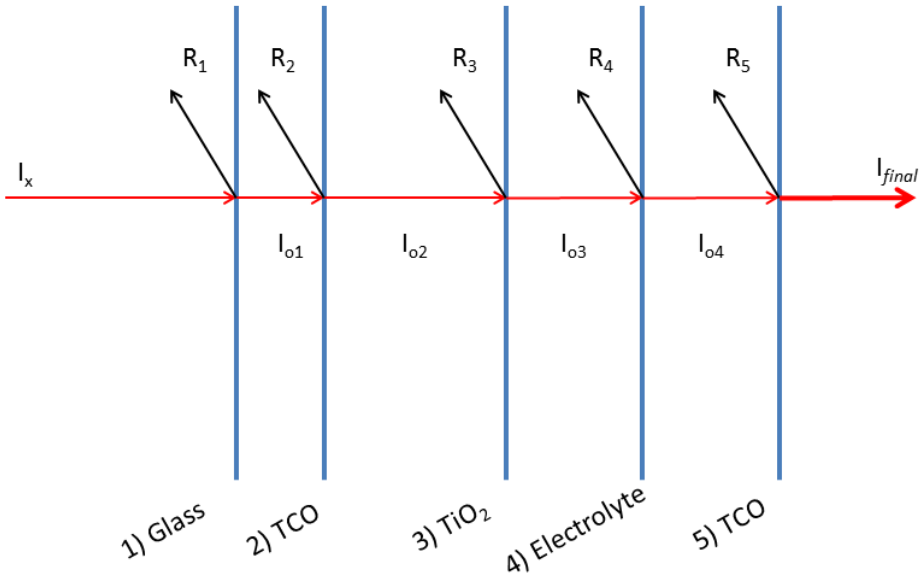

Figure 7.1: A depiction of the interfaces indicent light must pass through to get to the CIGS solar cell, used in this chapters model.

The absorbance for each layer was calculated by determination of the absorption co-efficient for each layer, determined using the Beer-Lambert law and measured with a UV-vis-NIR spectrophotometer. The Absorbance given by A = 100% - R% - T% by each material. It is possible to more accurately determine the transmission of light through several layers of thickness, t, by using the refractive index of each material, n, combined with the absorption co-efficient and the Fresnel equations, given in equation:

$$\% \ R = \left(\frac{n_1 - n_2}{n_1 + n_2} \right)^2 \tag{7.1}$$

The Fresnel equations although more accurate in modelling the reflections at each interface, require the refractive index of each material. It is possible to measure this in each material empirically, but difficulties arise with porous or light scattering layers, such at the dyed DSC layer. Ellipsometry may be used as a technique to calculate the refractive index but was not chosen as this technique uses a model to determine the refractive index. Several attempts were made to model the refractive index using

a dyed and undyed 8 μm TiO_2 electrode on a 1 mm thick glass slide. Despite several attempts to fit the best model in the ellipsometry software and Cauchy's equations it was not possible to accurately replicate the transmission spectrum of light through a glass/DSC interface. The absorption co-efficient can be measured directly from the layer of a known thickness, the refractive index can be modelled from measured data using ellipsometry. Although for thin films this can be a trivial measurement, for sensitised TiO_2 layers this can be complex. The ability of the undyed TiO_2 layer to reduce the transmission of incoming light through scattering rather than reflection can cause complications when modelling the refractive index. Initially the model would have been made from several interfaces using refractive indices. Several attempts were made to model the refractive index, so that the thickness of the layer could be adjusted to give more realistic transmission and reflectance data instead of using the Beer-Lambert law. No modelled data were able to simulate the transmission of light through the dyed or undyed TiO_2 layer as well as that derived from the absorption co-efficient and as such the crude approximation of optical behaviour in the device was made through the use of the Beer-Lamber law.

For comparison to this model the DSC transmission was measured for several TiO_2 thicknesses using a UV-vis-NIR spectrometer, each TiO_2 layer was dyed with N719 and had been screen printed onto TEC8 FTO coated glass. it would be preferential to be able to simply modify a numerical value to denote the thickness of the DSC absorber layer, rather than enter a new set of appropriate data, this may also help to remove any measurement error from the variation in TiO_2 electrode quality from screen printing. The thickness of the DSC layer can have a substantial effect on the transmission of light through to the CIGS layer and as such confirms the importance of being able to easily change the thickness for the model. The nature of the DSC absorber layer, a thin layer of TiO_2 dyed with a sensitising dye (such as N719), gives rise to several modelling challenges.

The transmission, reflectance and absorbance for the glass, FTO and dyed TiO_2 layer can be seen in Figure 7.2. As has been discussed in previous chapters there is a high absorption of NIR photons as a result of the FTO layer, with almost no contribution from the glass and TiO_2 layer. For comparison the dyed TiO_2 data can be seen in Figure 7.3, which details the extent of the absorption for a 6μm thick layer sensitised with N719 dye. This shows the typically observed double hump profile, with little absorption in the NIR.

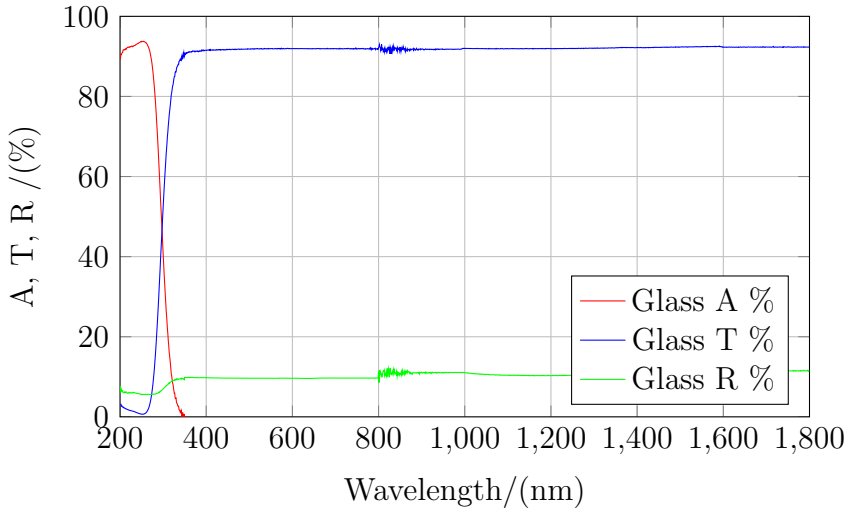

(a)

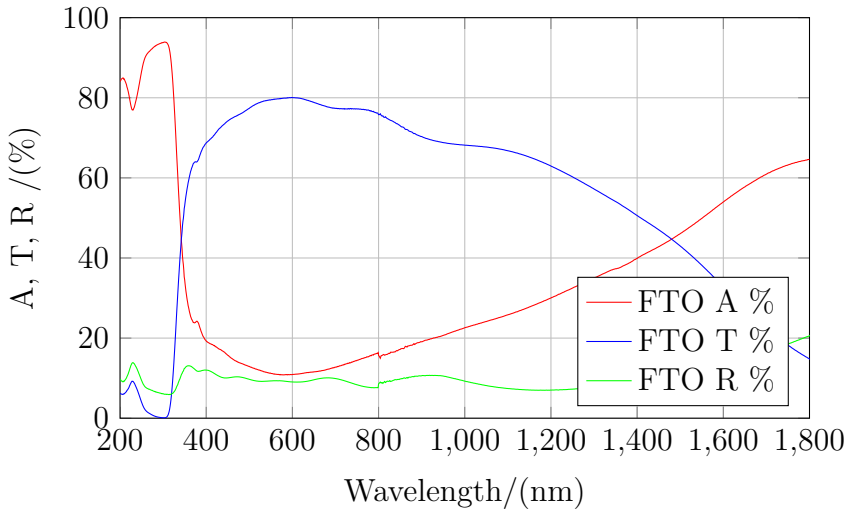

(b)

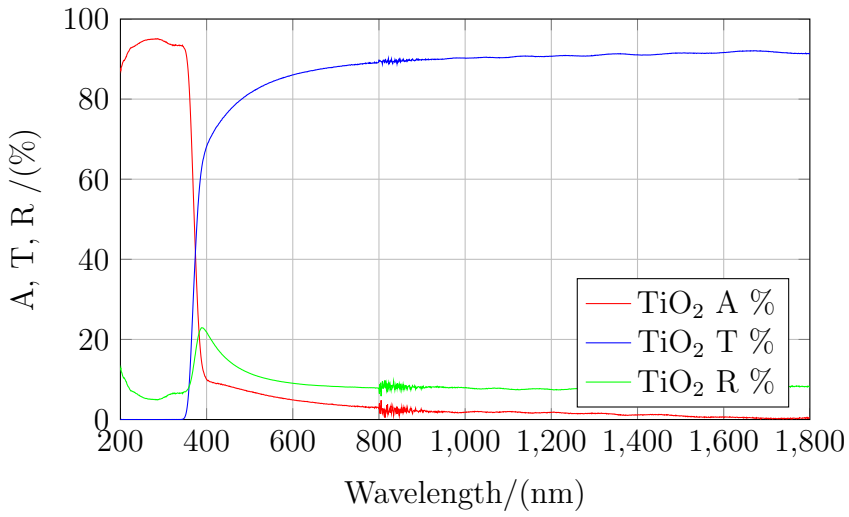

(c)

Figure 7.2: Absorbance, transmission and reflectance data as a percentile for 1.1 mm glass, TEC8 fluorine-doped tin oxide and unsensitised TiO_2.

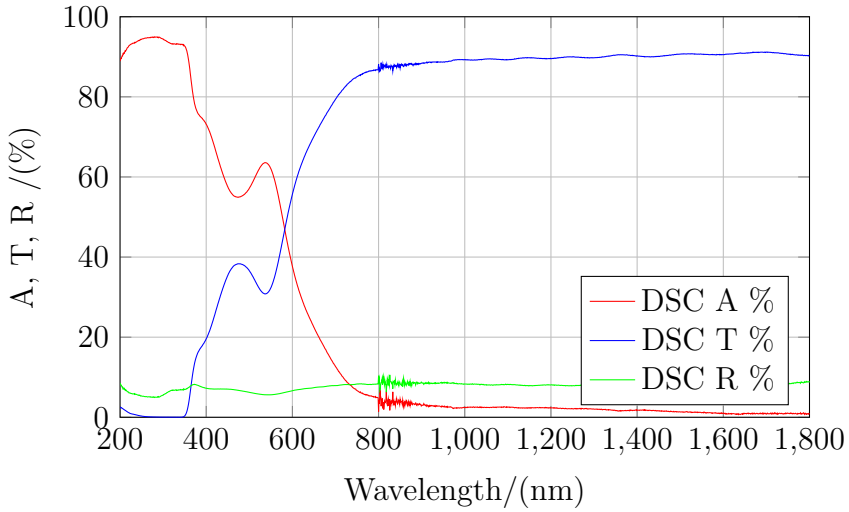

Figure 7.3: Measured absorbance, transmission and reflectance of a DSC with a 8 μm thick TiO_2 layer sensitised with N719 dye.

7.4 Results

Using FTO TEC 8 as the TCO and the primary source of reflection, the modelled transmission through a Glass/FTO/DSC stack can be seen in Figure 7.4a for varying thickness of TiO_2.The overall transmission of relevant wavelengths to the CIGS absorber layer (>800 nm) is not ideal, given the absorption of the FTO layer resulting in less than ca.70 % of all photons between 800 - 1200 nm available to the CIGS layer. It should also be highlighted that the CIGS device itself has several additional layers before the absorber layer, the second TCO layer (typically ITO) and CdS n-type layer. The absorption from the CdS layer is negligible given its typical 50 nm thickness and will be ignored in the remainder of the model in this chapter. Inclusion of this ITO layer into the model can be seen in Figure 7.4b. Further reduction of transmitted photons leaves almost half of photons with wavelength 800-1200 nm available, likely to manifest as a severe reduction in current density given the limitation of the device performance in a series configuration. Reduction of light to the CIGS layer has already been studied in this thesis, in Chapter 5, although the extent of this photon reduction is not likely to effect the V_{oc} in the same manner as the J_{sc}. Some solar cell materials such as silicon do not perform well in periods reduced solar irradiance, such as the sunrise/set and even the winter. A particular strength of DSCs is their ability to still deliver their optimum open circuit voltage, with only their current density slightly reduced. This has been demonstrated at illumination as low as 0.1 Suns, which is roughly 10 % of the intensity of AM 1.5G. This reduction in photons to the CIGS absorber described in the modelled FTO/DSC/ITO configuration demonstrates the necessity to improve the transmission to increase the performance of the overall tandem device. In Chapter 5 the J_{sc}produced from the DSC/CIGS devices were not equivalent to the DSC J_{sc}, which should be the current limiting junction.

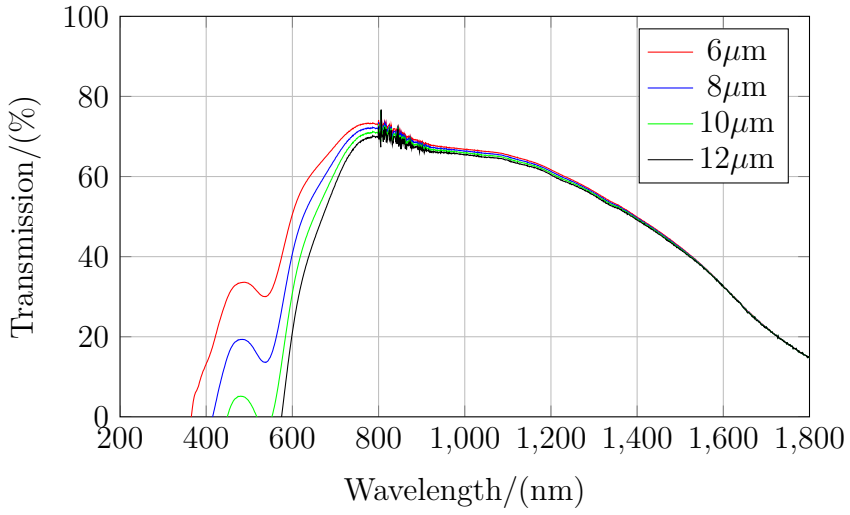

(a)

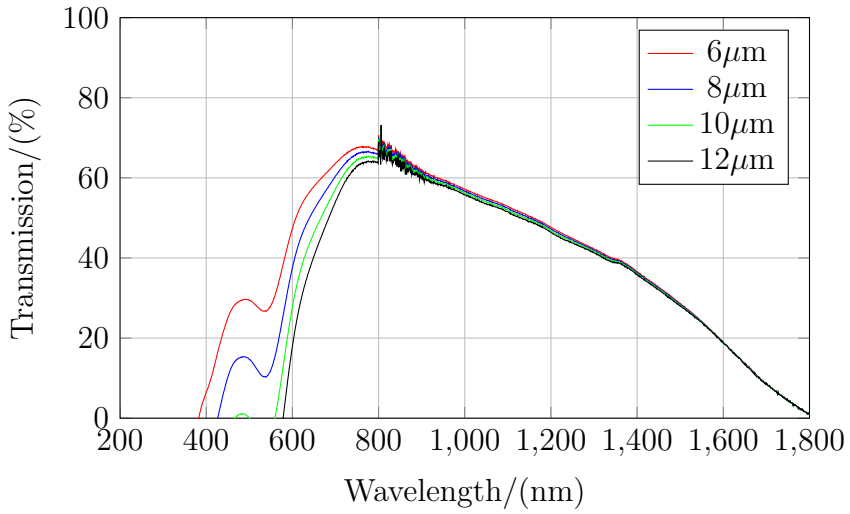

(b)

Figure 7.4: Modelled data for % transmission of indicent photons through a (a) glass/FTO/DSC and (b) glass/FTO/DSC/ITO stack at varying DSC thicknesses.

Introduction of a high transmittance TCO in the NIR in the form of either ITiO or IZO as the front contact shows a clear improvement in transmission of photons in the CIGS absorption region. An increased transmission of roughly 10 % can be seen in Figure 7.5 when compared to FTO. In part this corrects for the absorption by the CIGS ITO layer and is in agreement with empirical data reported elsewhere [122]. The transmission of light through the device is almost equivalent regardless of whether ITiO or IZO is used, with ITiO having a more flat profile in the CIGS absorption region. The transmission in the visible region of both profiles may also be used to confirm that 12 μm is an optimum thickness for the DSC layer. Given that layers thicker than this can result in sub-optimal performance electrically, this result is encouraging. Due to the lower bandgap of IZO over ITiO the absorption onset is redshifted, resulting in ITiO being the more suitable TCO for use with DSCs. In addition ITiO has shown thermal and chemical stability compatible with the DSC

fabrication process. It is unlikely that without using low temperature processing for DSCs, that IZO will be suitable as the top contact as heating in air causes crystallization of the thin film and degradation of electrical properties. Low cost processing has been studied in depth, however this typically yields TiO_2 electrodes of substandard performance compared with the method used throughout this thesis.

The inclusion of the CIGS ITO layer to the model further diminishes transmission as expected, seen in Figure 7.6, however both ITiO and IZO as a front contact realises an improvement in overall transmission of photons to the CIGS device, compared to the FTO/ITO combination in Figure 7.3.

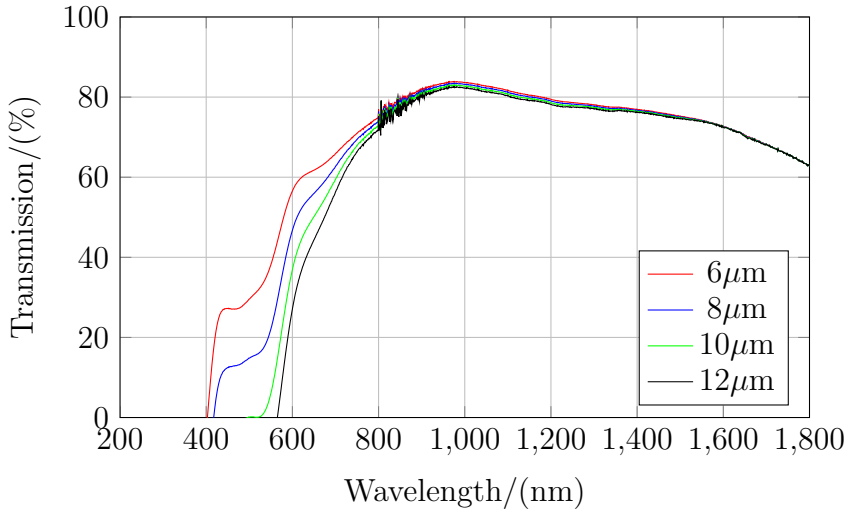

(a)

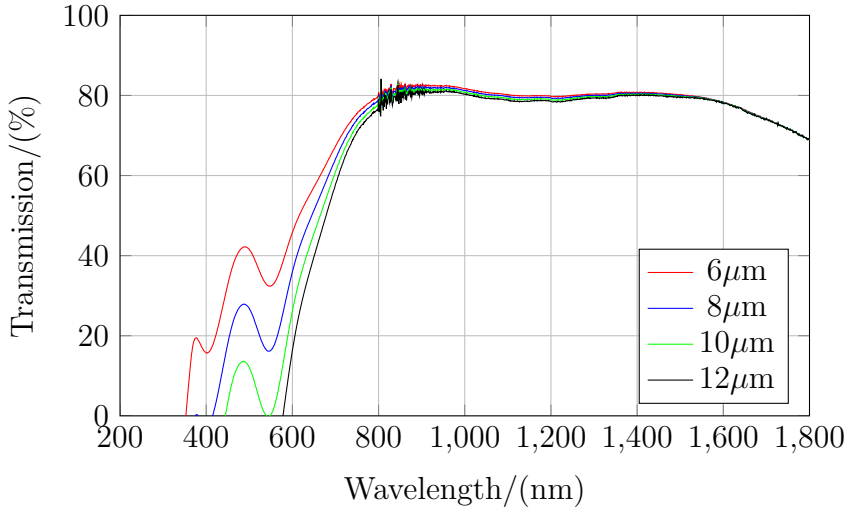

(b)

Figure 7.5: Modelled data for % transmission of incident photons through a (a) glass/IZO/DSC and (b) glass/ITiO/DSC stacks at varying DSC thicknesses.

ITiO shows a higher transmission in the glass/TCO/DSC/ITO stack compared to IZO, a result of its overall higher transmission in the NIR. Given the advantages of ITiO over IZO when considering its application in DSCs, it should be the TCO of choice in the front contact of a tandem DSC/CIGS and would be better suited than

FTO. IZO may not be a candidate for the top contact but may be better suited as the TCO of the CIGS device in stead of AZO/ITO. IZO may be deposited at room temperature with no loss in opto-electronic performance, which is not a characteristic in TCOs commonly used in CIGS device fabrication (AZO and/or ITO).

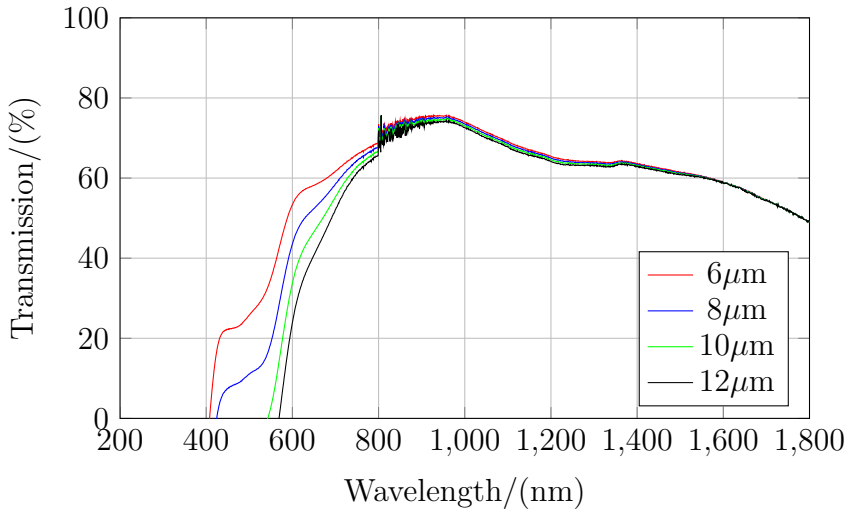

(a)

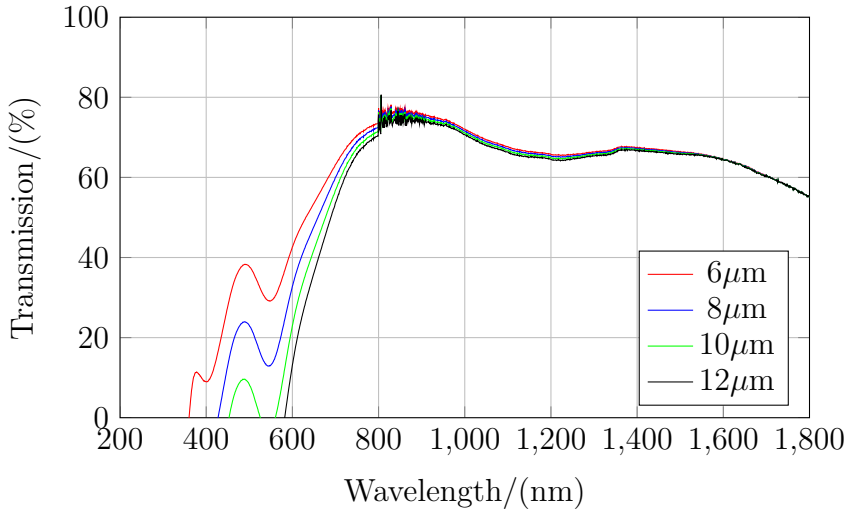

(b)

Figure 7.6: Modelled data for % transmission of incident photons through a (a) glass/IZO/DSC/ITO and (b) glass/ITiO/DSC/ITO stack at varying DSC thicknesses.

Potentially the combination of both TCOs presented in this thesis could overcome the current density limitation of the DSC/CIGS tandem solar cell. With ITiO used as the front contact and IZO as the CIGS contact it may be possible to greatly increase the transmission to the CIGS absorber layer and increase the current of the CIGS layer to match the DSC. If successful this could increase the efficiency of the monolithic device above the current 12 % maximum. The resulting optical model can be seen in Figure 7.7, with ITiO and IZO used as the TCOs. The 12 μm thick DSC layer can again be seen to be the optimum thickness, as it demonstrates the ability to absorb all light in the area of the DSC bandgap. The transmission to the CIGS

layer is also vastly improved over the original FTO/ITO combination seen previously in Figure 7.4b.

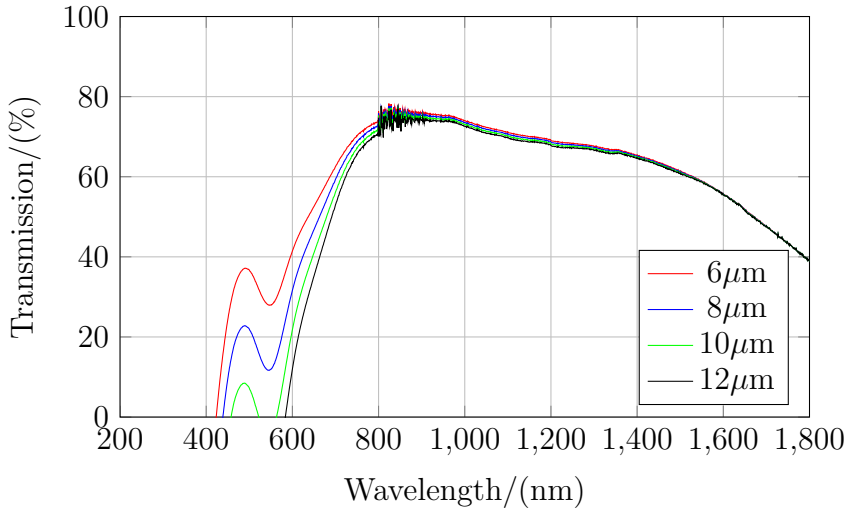

Figure 7.7: Modelled data for % transmission of incident photons through a glass/ITiO/DSC/IZO stack at varying DSC thicknesses.

This improvement in transmission gives an overall improvement in transmission of nearly 20 % between 800-1200 nm. The tandem cell presented previously was had a current density roughly 10 % lower than that of a DSC fabricated using a ITiO front contact, for a FTO this is closer to 25 %.

Figure 7.8 highlights the difference in transmission between the FTO/ITO and ITiO/IZO structures against the external quantum efficiency of CIGS cells with different indium/gallium ratios. The latter structure offers a strong platform to increase the performance of the DSC/CIGS tandem cell, but also raises questions to the combination of these materials. The DSC absorption knowingly overlaps the CIGS absorption region, which serves to current match the overall device by preventing absorption of blue photons. This is useful, but given the parasitic absorption of NIR photons it has led to DSC/CIGS devices with poor current output, as this is limited to the worst performing device. Altering the In/Ga ratio may also serve to increase performance, which has been suggested previously [74]. Reduction of the Ga content will ultimately increase the V_{oc} whilst reducing the J_{sc} previously the opposite was deemed the correct choice, as reducing the J_{sc} would serve to current match the DSC/CIGS device however the parasitic absorption of the DSC layer would seem to accomplish this too effectively. It may be possible by either substituting CIGS for CIS or a low gallium concentration CIGS cell to increase the current density delivered at slight detriment of the V_{oc}.

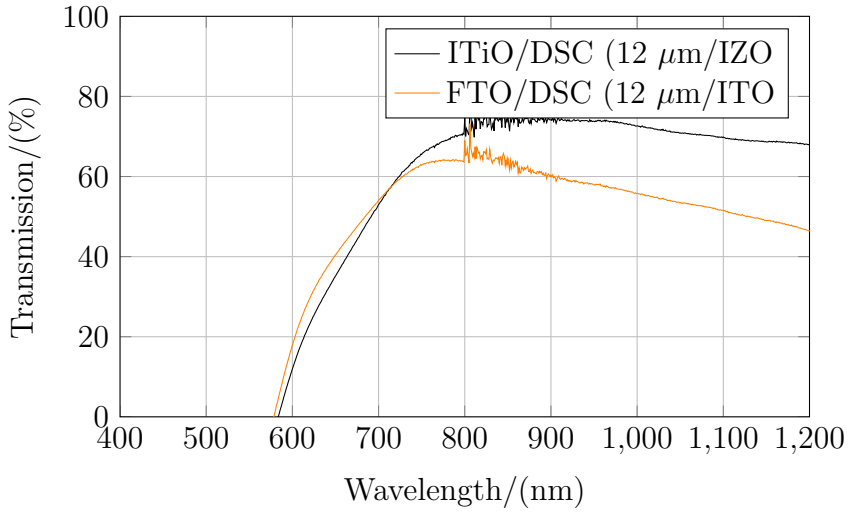

(a)

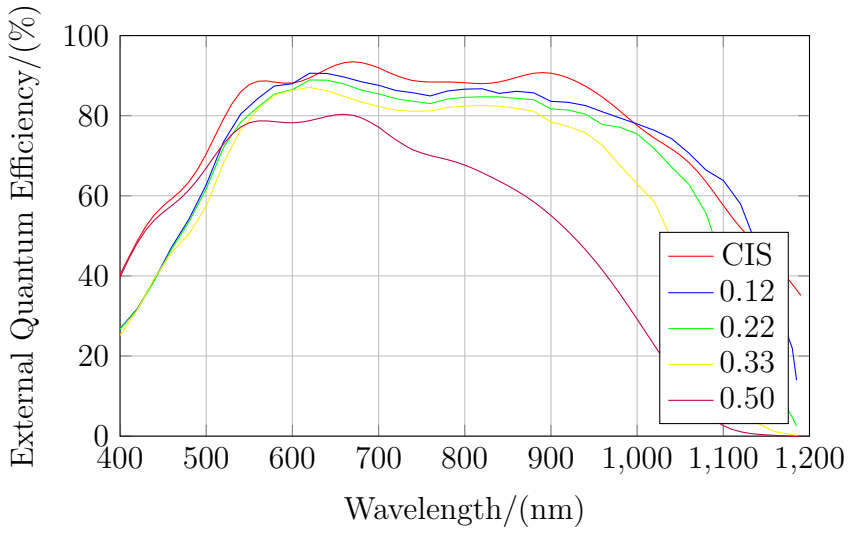

(b)

Figure 7.8: Modelled data for (a) transmission (%) for the FTO/DSC/ITO and ITiO/DSC/IZO stacks compared against (b) EQE data of CIGS absorbers with different indium/gallium ratios.

7.5 Conclusion

When attempting to enhance the efficiency of a solar cell the absorbing part of the device is often regarded at the key area to focus on. For CIGS this is particularly true given the complexity of the process used to form this quaternary structure. This chapter has signified the importance of ensuring that the optical interfaces are well optimised to complete a well performing device. The current TCOs used in both DSCs and CIGS solar cells are clearly not well suited to maximise current density in a monolithic DSC/CIGS solar cell and switching to NIR transmitting TCOs such as ITiO and IZO would benefit this setup. In doing so the balance of the current matching current achieved may be disturbed, however the ability to manipulate the CIGS In/Ga ratio will help to restore this balance and realise a fully optimised tandem

structure.

Chapter 8

CONCLUSIONS

This thesis has sought to solve and contribute to two of the main issues with DSC/CIGS tandem solar cells highlighted in both this thesis and by other research groups. Firstly the CIGS layer requires a greater number of photons relevant to its bandgap (800-1200 nm) to improve the overall efficiency of the device. These photons are currently absorbed by the FTO used as the top contact in the DSC layer. Secondly a solution to corrosion of the CIGS layer by the electrolyte used for hole conduction to the DSC TiO_2 layer. In addition to contributing to these two issues additional methodologies for the measurement and fabrication of DSC/CIGS tandem devices have been determined.

Replacement of the FTO top contact in the tandem device by the high mobility ITiO increases transmission through the DSC top stack without sacrificing performance of the DSC cell. This increase in transmission led, in part, to an increased efficiency of a DSC/CIGS tandem solar cell when in a monolithic configuration. This performance improvement was, however, slight and helped to raise additional questions about the simplicity of fabricating a tandem cell from existing separate technologies. Improvement in the deposition of ITiO itself was made to keep in theme with the low cost approach of this thesis. FTO is currently produced by deposition onto molten float glass, combining its production with that of the glass itself. With the remaining world supply of indium a topic of much discussion of whether supply not meeting demand will increase the cost, an alternative method to deposit ITiO was sought to increase deposition rates and throughput. The use of a pulsed DC power supply increased the deposition rate by 10 % when compared to that produced by RF sputtering. The use of the pulsed DC power supply did produce ITiO films with different crystallinity compared to those deposited using a RF power supply. Despite these differences in crystallinity the pulsed DC films were comparable in performance to the RF films and used to produce DSCs with identical performance.

Tandem DSC/CIGS solar cells fabricated to determine the performance increase of using ITiO also helped to highlight several issues facing measurement of such devices. I-V measurements of DSCs typically require partial masking of the absorber in order to accurately know the area for the calculation of the device efficiency. For CIGS this

is performed by mechanically scribing (and removing) the absorber layer. DSC/CIGS devices to date have been assembled by replacing the typical counter electrode with a complete CIGS solar cell of a similar area. This thesis has demonstrated the need to continue the practise of shading the device using a mask for more accurate efficiency measurements, but successfully describes a new method to drastically reduce V_{oc} and J_{sc} losses through unintentional shading of the CIGS cell. Removal of excess CIGS to reduce the cell area close to that of the DSC TiO_2 electrode brought the performance in line with that of an unmasked tandem device when masked. A considerable amount of CIGS was wasted during this process and would be uneconomical for any industrial application. It was concluded that this would be more effectively achieved through fabrication of the CIGS to match the cell area of the DSC, rather than removing excess material after.

Despite the improvements in cost reduction and efficiency increases, the DSC/CIGS solar cell is not currently a stable device as it suffers breakdown upto 48 hours after fabrication caused by corrosion by the electrolyte. As this corrosion occurs through pinholes in the CIGS TCO an alternative was investigated, the amorphous TCO zinc oxide-doped indium oxide. Other buffer layer materials have been employed as a barrier to chemical and thermal reactions, SnO_2 is an example employed in this thesis to protect ITiO. Novel characterisation of IZO deposited from a single ceramic target was documented, along with demonstrating the Urbach tailing typically observed in other amorphous materials. Despite the lack of apparent grain boundaries and pin holes IZO was shown to unsuccessfully withstand the percolation of the DSC electrolyte, resulting in etching of the test layers beneath it in every trial. Several other thin films were tested, also unsuccessful in preventing etching of the test layer. Despite this, IZO was identified as a candidate material to replace ITO/AZO as the CIGS TCO layer due to its ability to be deposited at the low/room temperatures required during CIGS cell fabrication without any loss of performance. In a DSC/CIGS tandem it was shown using modelled data, that the use of ITiO and IZO together to replace the currently used FTO and ITO/AZO could increase transmission to the CIGS layer by up to 30 %. The efforts made and achieved throughout the process of this thesis, in order to circumvent the issues around the DSC/CIGS tandem solar cell, has revealed a few inherent but new issues connected with tandem solar cell fabrication using the monolithic (2-wired) series configuration. These may be highlighted as below:

1. The development of the high mobility TCO, ITiO, was successfully deposited using an industrially favoured pulsed DC process for the first time. Thin films deposited by this method were then successfully incorporated into monolithic tandem DSC/CIGS devices.

2. It has been identified that the monolithic tandem DSC/CIGS tandem structure fabrication process has practical issues. Shading losses were detected from fabrication methods currently employed in research, when attempting to measure the

device with a mask. This thesis provides directions to modify the methodology of the fabrication process carried out at laboratory and industrial scales.

3. The choice of a low temperature processed and amorphous TCO, IZO, was successfully deposited and optimised in an attempt to provide a corrosion barrier to the CIGS cell whilst acting as a highly transparent conducting layer. It was shown that IZO did not cause any damage to the CIGS layer, but was unable to prevent damage from the liquid electrolyte used in conventional DSCs. This has made a firm conclusion on the fact that liquid electrolyte based tandem structures are not favourable routes and the alternatives for solid state devices remain as the only viable option.

8.1 Future Directions

DSC/CIGS tandem solar cells had been shown to be a promising combination of two well understood technologies. It has become clear however that further optimisation is required to integrate both separate devices to yield a true low-cost, high efficiency tandem device. The corrosion of the finished device is a clear limitation and must either be suppressed or the electrolyte removed from the tandem device. Some alternatives could be explored such as water based electrolytes or hole conducting polymers currently employed in solid state DSCs. Currently the most efficient DSCs exist with the redox electrolyte used in this thesis, exploring alternatives although recommended, may require further optimisation in keeping or in fact progressing the efficiency of the DSC/CIGS tandem. It is entirely possible to remain with the 2 device stacked approach from the seminal paper on this tandem device, however this is not a realistic prospect for electricity generation given the additional costs of the extra glass and coatings. Even the additional weight from this glass should be considered, given the transportation costs, ease of installation and the ability to install on certain properties. This 2 device stacked tandem immediately removes the advantage afforded from thin film solar cells and despite the current efficiency advantage should be avoided.

Exploration of emerging technologies such as perovskite solar cells to replace the DSC as the top absorber may solve the corrosion problem as they are solid state devices. These devices are met with their own challenges, such as their inherent instability in air, but their enormous improvement in efficiency over DSCs should not be overlooked. The TCOs demonstrated in this thesis would be suitable for both the front contact of the perovskite cell and the contact of the CIGS and their improvement in transmission would allow a greater J_{sc} to be obtained from the CIGS to match the perovskite (which is much greater than that of a DSC). Simple modelling can be performed, similar to that presented in this thesis, to suggest improvements to this architecture and identify any potential shortcomings.

References

[1] A Mirchi, S Hadian, K Madani, O. M. Rouhani, and A. M. Rouhani. World Energy Balance Outlook and OPEC Production Capacity: Implications for Global Oil Security. *Energies*, 5(12):2626–2651, July 2012.

[2] K H Nealson and P G Conrad. Life: past, present and future. *Philosophical transactions of the Royal Society of London. Series B, Biological sciences*, 354(1392):1923–39, December 1999.

[3] BP. Statistical Review of World Energy 2013.

[4] Max Planck. Ueber das Gesez der Engergieverteilung im Normalspectrum. *Annalen der Physik*, 309(3):553–563, 1901.

[5] NREL. http://rredc.nrel.gov/solar/spectra/am1.5/.

[6] ASTM Standard G173-03, 2012, Standard Tables for Reference Solar Spectral Irradiances: Direct Normal and Hemispherical on 37° Tilted Surface.

[7] William Shockley and Hans J. Queisser. Detailed Balance Limit of Efficiency of p-n Junction Solar Cells. *Journal of Applied Physics*, 32(3):510–519, 1961.

[8] C H Henry. Limiting efficiencies of ideal single and multiple energy gap terrestrial solar cells. *Journal of Applied Physics*, 51(August):4494–4500, 1980.

[9] Martin A Green, Keith Emery, Yoshihiro Hishikawa, Wilhelm Warta, and Ewan D Dunlop. Solar Cell Efficiency Tables (Version 41). *Progress in Photovoltaics: Research and Applications*, 21:1–11, 2013.

[10] Jianhua Zhao, Aihua Wang, Martin A Green, Francesca Ferrazza, and Via A D Andrea. 19.8% Efficient Honeycomb Textured Multicrystalline and 24.4% Monocrystalline Silicon Solar Cells. *Applied Physics Letters*, 73(14):1991–1993, 1998.

[11] NREL. Best Research-Cell Efficiencies, 2016.

[12] Leo Pessin and Douglas Rusta. A Comparison of Solar-Cell and Battery-Type Power Systems for Spacecraft. In *IEEE Transactions On Aerospace And Electronic Systems*, number 6, pages 889–897, 1967.

[13] Keith A Emery, Martin Green, and Ewan Dunlop. Solar cell efficiency tables (Version 45). (January), 2015.

[14] Simon M Sze. *Semiconductor Devices: Physics and Technology*. Wiley, New York, 2nd edition, 1981.

[15] J M Woodall and H J Hovel. High-efficiency $Ga_{1-X}Al_XAs$/GaAs Solar Cells. *Applied Physics Letters*, 21(8):131–133, 1972.

[16] J. J. Schermer, P. Mulder, G. J. Bauhuis, P. K. Larsen, G. Oomen, and E. Bongers. Thin-film GaAs Epitaxial Lift-off Solar Cells for Space Applications. *Progress in Photovoltaics: Research and Applications*, 13(7):587–596, November 2005.

[17] L. El Chaar, L.A. Lamont, and N. El Zein. Review of Photovoltaic Technologies. *Renewable and Sustainable Energy Reviews*, 15(5):2165–2175, June 2011.

[18] O. Schultz, S. W. Glunz, and G. P. Willeke. Multicrystalline Silicon Solar Cells Exceeding 20% Efficiency. *Progress in Photovoltaics: Research and Applications*, 12(7):553–558, November 2004.

[19] Xinming Huang, Fanghua Xu, Bo Zhao, and Genxiang Zhong. Ingot casting method for quasi-monocrystalline silicon, 2010.

[20] D. A. Cusano. CdTe Solar Cells and Photovoltaic Hetero-junctions in II-VI Compounds. *Solid-State Electronics*, 6:217–232, 1963.

[21] Ingrid Repins, Miguel A Contreras, Brian Egaas, Clay Dehart, John Scharf, Craig L Perkins, Bobby To, and Rommel Noufi. 19.9 %-efficient ZnO/CdS/$CuInGaSe_2$ Solar Cell with 81.2 % Fill Factor. *Progress in Photovoltaics: Research and Applications*, 16(February):235–239, 2008.

[22] V. K. Kapur, B. M. Basol, and E. S. Tseng. Low Cost Methods for the Productions of Semiconductor Films for $CuInSe_2$/CdS Solar Cells. *Solar Cells*, 21:65 – 72, 1987.

[23] Karl W Böer. The CdS/Cu_2S Solar Cell. *Journal of Crystal Growth*, 59:111–120, 1982.

[24] J Meier, J Spitznagel, U Kroll, C Bucher, S Fay, T Moriarty, and A Shah. Potential of Amorphous and Microcrystalline Silicon Solar Cells. *Thin Solid Films*, 451-452:518–524, March 2004.

[25] M Powalla, P Jackson, D Hariskos, S Paetel, W Witte, R Wurz, E Lotter, R Menner, and W Wischman. CIGS Thin-Film Solar Cells with an Improved Efficiency of 20.8%. *29th European Photovoltaic Solar Energy Conference, 3AO.4.2, Amsterdam*, 2014.

[26] First Solar. The Recycling Advantage: Committed to Responsible Life-Cycle Management.

[27] Hironori Katagiri, Kazuo Jimbo, Win Shwe Maw, Koichiro Oishi, Makoto Yamazaki, Hideaki Araki, and Akiko Takeuchi. Development of CZTS-based Thin Film Solar Cells. *Thin Solid Films*, 517(7):2455–2460, February 2009.

[28] Martin A Green, Keith Emery, Yoshihiro Hishikawa, Wilhelm Warta, and Ewan D Dunlop. Solar cell efficiency tables (version 43). *Prog. Photovolt: Res. Appl.*, 22:1–9, 2014.

[29] Antonio Luque. Will We Exceed 50 % Efficiency in Photovoltaics? *Journal of Applied Physics*, 110(031301):1–19, 2011.

[30] SHARP. Sharp Develops Concentrator Solar Cell with Worlds Highest Conversion Efficiency of 43.5%.

[31] P. Liska, K. R. Thampi, M. Gratzel, D. Bremaud, D. Rudmann, H. M. Upadhyaya, and A. N. Tiwari. Nanocrystalline dye-sensitized solar cell/copper indium gallium selenide thin-film tandem showing greater than 15% conversion efficiency. *Applied Physics Letters*, 88(20):203103, 2006.

[32] B. O'Regan and M. Gratzel. A low-cost, high-efficiency solar cell based on dye-sensitized colloidal TiO_2 films. *Nature*, 353(6346):737–740, 1991.

[33] S Ito, T Murakami, P Comte, P Liska, C Gratzel, M Nazeeruddin, and M Gratzel. Fabrication of thin film dye sensitized solar cells with solar to electric power conversion efficiency over 10%. *Thin Solid Films*, 516(14):4613–4619, May 2008.

[34] Takeru Bessho, Shaik M. Zakeeruddin, Chen-Yu Yeh, Eric Wei-Guang Diau, and Michael Grätzel. Highly Efficient Mesoscopic Dye-Sensitized Solar Cells Based on Donor-Acceptor-Substituted Porphyrins. *Angewandte Chemie International Edition*, 49:6646–6649, August 2010.

[35] Anders Hagfeldt, Gerrit Boschloo, Licheng Sun, Lars Kloo, and Henrik Pettersson. Dye-Sensitized Solar Cells. *Chemical Reviews*, 110(11):6595–6663, 2010.

[36] Akihiro Kojima, Kenjiro Teshima, Yasuo Shirai, and Tsutomu Miyasaka. Organometal halide perovskites as visible-light sensitizers for photovoltaic cells. *Journal of the American Chemical Society*, 131(17):6050–6051, 2009.

[37] Michael M Lee, Joël Teuscher, Tsutomu Miyasaka, Takurou N Murakami, and Henry J Snaith. Efficient hybrid solar cells based on meso-superstructured organometal halide perovskites. *Science (New York, N.Y.)*, 338(6107):643–7, November 2012.

[38] RR King, NH Karam, and JH Ermer. Next-generation, High-efficiency III-V Multijunction Solar Cells. *Proc. 28th IEEE Photovoltaic Specialists Conference, Anchorage, Alaska*, pages 28–31, 2000.

[39] Qing Wang, Seigo Ito, Michael Grätzel, Francisco Fabregat-Santiago, Iván Mora-Seró, Juan Bisquert, Takeru Bessho, and Hachiro Imai. Characteristics of high efficiency dye-sensitized solar cells. *The journal of physical chemistry. B*, 110(50):25210–21, December 2006.

[40] Laurence M Peter. Dye-sensitized nanocrystalline solar cells. *Physical chemistry chemical physics : PCCP*, 9(21):2630–42, June 2007.

[41] Inyoung Shin, Hyunwoong Seo, Min-Kyu Son, Jin-Kyoung Kim, K. Prabakar, and Hee-Je Kim. Analysis of TiO_2 thickness effect on characteristic of a dye-sensitized solar cell by using electrochemical impedance spectroscopy. *Current Applied Physics*, 10(3):S422–S424, May 2010.

[42] Liyuan Han, Ashraful Islam, Han Chen, Chandrasekharam Malapaka, Barreddi Chiranjeevi, Shufang Zhang, Xudong Yang, and Masatoshi Yanagida. High-efficiency dye-sensitized solar cell with a novel co-adsorbent. *Energy & Environmental Science*, pages 3–6, 2012.

[43] Henry J. Snaith. How should you measure your excitonic solar cells? *Energy & Environmental Science*, 5(4):6513, 2012.

[44] Qifeng Zhang, Christopher S. Dandeneau, Xiaoyuan Zhou, and Guozhong Cao. ZnO Nanostructures for Dye-Sensitized Solar Cells. *Advanced Materials*, 21(41):4087–4108, November 2009.

[45] Brian C O Regan, James R Durrant, Paul M Sommeling, and Nicolaas J Bakker. Influence of the $TiCl_4$ Treatment on Nanocrystalline TiO_2 Films in Dye-Sensitized Solar Cells, Charge Density , Band Edge Shifts , and Quantification of Recombination Losses at Short Circuit. pages 14001–14010, 2007.

[46] Christophe J Barbe, Francine Arendse, Pascal Comte, Marie Jirousek, Frank Lenzmann, Valery Shklover, and Michael Gra. Nanocrystalline Titanium Oxide Electrodes for Photovoltaic Applications. 71:3157–3171, 1997.

[47] Sorapong Pavasupree, Jaturong Jitputti, Supachai Ngamsinlapasathian, and Susumu Yoshikawa. Hydrothermal synthesis, characterization, photocatalytic activity and dye-sensitized solar cell performance of mesoporous anatase TiO_2 nanopowders. *Materials Research Bulletin*, 43(1):149–157, January 2008.

[48] Motonari Adachi, Yusuke Murata, Jun Takao, Jinting Jiu, Masaru Sakamoto, and Fumin Wang. Highly efficient dye-sensitized solar cells with a titania thin-film electrode composed of a network structure of single-crystal-like TiO_2

nanowires made by the "oriented attachment" mechanism. *Journal of the American Chemical Society*, 126(45):14943–9, November 2004.

[49] Motonari Adachi, Yusuke Murata, Issei Okada, and Susumu Yoshikawa. Formation of Titania Nanotubes and Applications for Dye-Sensitized Solar Cells. *Journal of The Electrochemical Society*, 150(8):G488, 2003.

[50] Michael Grätzel. Recent advances in sensitized mesoscopic solar cells. *Accounts of chemical research*, 42(11):1788–98, November 2009.

[51] Shane Ardo and Gerald J Meyer. Photodriven heterogeneous charge transfer with transition-metal compounds anchored to TiO_2 semiconductor surfaces. *Chemical Society reviews*, 38(1):115–64, January 2009.

[52] Mohammad K Nazeeruddin, Peter Pe, Thierry Renouard, Shaik M Zakeeruddin, Robin Humphry-baker, Pascal Comte, Paul Liska, Le Cevey, Emiliana Costa, Valery Shklover, Leone Spiccia, Glen B Deacon, and Carlo A Bignozzi. Engineering of Efficient Panchromatic Sensitizers for Nanocrystalline TiO_2 -Based Solar Cells. (c):1613–1624, 2001.

[53] Muhammad Imran Asghar, Kati Miettunen, Janne Halme, Paula Vahermaa, Minna Toivola, Kerttu Aitola, and Peter Lund. Review of stability for advanced dye solar cells. *Energy & Environmental Science*, 3(4):418, 2010.

[54] Neil Robertson. Optimizing dyes for dye-sensitized solar cells. *Angewandte Chemie (International ed. in English)*, 45(15):2338–45, April 2006.

[55] W.M. Campbell, K.W. Jolley, P. Wagner, K. Wagner, P.J. Walsh, K.C. Gordon, L. Schmidt-Mende, M.K. Nazeeruddin, Q. Wang, M. Gratzel, and D.L. Officer. Highly Efficient Porphyrin Sensitizers for Dye-Sensitized Solar Cells. *Journal of Physical Chemistry C*, 111(32):11760–11762, August 2007.

[56] L Giribabu, Ch Vijay Kumar, M Raghavender, K Somaiah, P Yella, and P Venkateswara Rao. Durable Unsymmetrical Zinc Phthalocyanine for Near IR Sensitization of Nanocrystalline TiO_2 Films With Non-Volatile Redox Electrolytes. *Nano*, 2:39–47, 2008.

[57] Kang Deuk Seo, Hae Min Song, Myung Jun Lee, Mariachiara Pastore, Chiara Anselmi, Filippo De Angelis, Mohammad K. Nazeeruddin, Michael Gräetzel, and Hwan Kyu Kim. Coumarin dyes containing low-band-gap chromophores for dye-sensitised solar cells. *Dyes and Pigments*, 90(3):304–310, September 2011.

[58] Jeong-Hyeok Im, Chang-Ryul Lee, Jin-Wook Lee, Sang-Won Park, and Nam-Gyu Park. 6.5% Efficient Perovskite Quantum-Dot-Sensitized Solar Cell. *Nanoscale*, 3(10):4088–93, October 2011.

[59] Pablo Docampo, James M Ball, Mariam Darwich, Giles E Eperon, and Henry J Snaith. Efficient organometal trihalide perovskite planar-heterojunction solar cells on flexible polymer substrates. *Nature communications*, 4:2761, January 2013.

[60] Aswani Yella, Hsuan-Wei Lee, Hoi Nok Tsao, Chenyi Yi, Aravind Kumar Chandiran, Md Khaja Nazeeruddin, Eric Wei-Guang Diau, Chen-Yu Yeh, Shaik M Zakeeruddin, and Michael Grätzel. Porphyrin-sensitized solar cells with cobalt (II/III)-based redox electrolyte exceed 12 percent efficiency. *Science*, 334(6056):629–34, November 2011.

[61] James R. Jennings and Qing Wang. Influence of Lithium Ion Concentration on Electron Injection, Transport, and Recombination in Dye-Sensitized Solar Cells. *The Journal of Physical Chemistry C*, 114(3):1715–1724, January 2010.

[62] Sara E Koops, Brian C O'Regan, Piers R F Barnes, and James R Durrant. Parameters influencing the efficiency of electron injection in dye-sensitized solar cells. *Journal of the American Chemical Society*, 131(13):4808–18, April 2009.

[63] Changneng Zhang, Yang Huang, Zhipeng Huo, Shuanghong Chen, and Songyuan Dai. Photoelectrochemical Effects of Guanidinium Thiocyanate on Dye-Sensitized Solar Cell Performance and Stability. *The Journal of Physical Chemistry C*, 113(52):21779–21783, December 2009.

[64] Peng Wang, Shaik M Zakeeruddin, Jacques E Moser, Mohammad K Nazeeruddin, Takashi Sekiguchi, and Michael Grätzel. A stable quasi-solid-state dye-sensitized solar cell with an amphiphilic ruthenium sensitizer and polymer gel electrolyte. *Nature materials*, 2(6):402–7, June 2003.

[65] Michael Grätzel. Dye-sensitized solar cells. *Journal of Photochemistry and Photobiology C: Photochemistry Reviews*, 4(2):145–153, October 2003.

[66] Yu Bai, Yiming Cao, Jing Zhang, Mingkui Wang, Renzhi Li, Peng Wang, Shaik M Zakeeruddin, and Michael Grätzel. High-performance dye-sensitized solar cells based on solvent-free electrolytes produced from eutectic melts. *Nature materials*, 7(8):626–30, August 2008.

[67] U Bach, P Comte, J E Moser, F Weisso, and M Gra. Solid-state dye-sensitized mesopourous TiO_2 solar cells with high photon-to-electron conversion efficiencies. *Nature*, 395(October):583–585, 1998.

[68] Jessica Kruger, Robert Plass, Le Cevey, Marco Piccirelli, Michael Gratzel, and Udo Bach. High efficiency solid-state photovoltaic device due to inhibition of interface charge recombination. *Applied Physics Letters*, 79(13):2085, 2001.

[69] Henry J Snaith, Adam J Moule, Cédric Klein, Klaus Meerholz, Richard H Friend, and Michael Grätzel. Efficiency enhancements in solid-state hybrid solar cells via reduced charge recombination and increased light capture. *Nano letters*, 7(11):3372–6, November 2007.

[70] Izak Kapilevich and Andy Skumanich. Indium Shortage Implications for the PV and LCD Market: Technology and Market Considerations for Maintaining Growth. In *34th IEEE Photovoltaics Specialists Conference (PVSC)*, pages 2055–2060, 2009.

[71] a Feltrin and a Freundlich. Material considerations for terawatt level deployment of photovoltaics. *Renewable Energy*, 33(2):180–185, February 2008.

[72] Billy J Stanbery. Copper Indium Selenides and Related Materials for Photovoltaic Devices. *Critical Reviews in Solid State and Materials Sciences*, 27(2):73–117, 2002.

[73] Physikalische Elektronik and Universitat Stuttgart. NEW ASPECTS OF PHASE SEGREGATION AND JUNCTION FORMATION IN CulnSe,. pages 323–326, 1997.

[74] S. Seyrling, S. Calnan, S. Bücheler, J. Hüpkes, S. Wenger, D. Brémaud, H. Zogg, and A.N. Tiwari. $CuIn_{1-x}Ga_xSe_2$ photovoltaic devices for tandem solar cell application. *Thin Solid Films*, 517(7):2411–2414, February 2009.

[75] M. Ruckh, D. Schmid, M. Kaiser, R. Schaffler, T. Walter, and H. W. Schock. INFLUENCE OF SUBSTRATES ON THE ELECTRICAL PROPERTIES OF Cu(ln,Ga)Se, THIN FILMS. *1st World Photovoltaic Solar Energy Conference, Hawaii*, pages 156–159, 1994.

[76] D. Rudmann, G. Bilger, M. Kaelin, F.-J. Haug, H. Zogg, and a.N. Tiwari. Effects of NaF coevaporation on structural properties of $Cu(In,Ga)Se_2$ thin films. *Thin Solid Films*, 431-432:37–40, May 2003.

[77] D. Rudmann, a. F. da Cunha, M. Kaelin, F. Kurdesau, H. Zogg, a. N. Tiwari, and G. Bilger. Efficiency enhancement of $Cu(In,Ga)Se_2$ solar cells due to post-deposition Na incorporation. *Applied Physics Letters*, 84(7):1129, 2004.

[78] Udai P. Singh and Surya P. Patra. Progress in Polycrystalline Thin-Film $Cu(In,Ga)Se_2$ Solar Cells. *International Journal of Photoenergy*, 2010:1–19, 2010.

[79] D Lincot, J Guillemoles, S Taunier, D Guimard, J Sicxkurdi, a Chaumont, O Roussel, O Ramdani, C Hubert, and J Fauvarque. Chalcopyrite thin film solar cells by electrodeposition. *Solar Energy*, 77(6):725–737, December 2004.

[80] Miguel A Contreras, John Tuttle, Andrew Gabor, Andrew Tennant, Kannan Ramanathan, Sally Asher, Amy Franz, James Keane, L Wang, John Scofield, and Rommel Noufi. HIGH EFFICIENCY Cu(In, Ga)Se_2 - BASED SOLAR CELLS: OF NOVEL ABSORBER STRUCTURES PROCESSING. pages 68–75, 1994.

[81] NREL. Method of fabricating high-efficiency Cu(In,Ga)$(SeS)_2$ thin films for solar cells, 1995.

[82] Congkang Xu, Hongwang Zhang, James Parry, Samanthe Perera, Gen Long, and Hao Zeng. Solar Energy Materials & Solar Cells A single source three-stage evaporation approach to CIGS absorber layer for thin film solar cells. *Solar Energy Materials and Solar Cells*, 117:357–362, 2013.

[83] J.a. Frantz, R.Y. Bekele, V.Q. Nguyen, J.S. Sanghera, a. Bruce, S.V. Frolov, M. Cyrus, and I.D. Aggarwal. Cu(In,Ga)Se_2 thin films and devices sputtered from a single target without additional selenization. *Thin Solid Films*, 519(22):7763–7765, September 2011.

[84] Y. C. Lin, Z. Q. Lin, C. H. Shen, L. Q. Wang, C. T. Ha, and Chris Peng. Cu(In,Ga)Se_2 films prepared by sputtering with a chalcopyrite Cu(In,Ga)Se_2 quaternary alloy and In targets. *Journal of Materials Science: Materials in Electronics*, 23(2):493–500, June 2011.

[85] MiaSole. MiaSolé Achieves 15.7% Efficiency with Commercial-Scale CIGS Thin Film Solar Modules, 2010.

[86] P. Reinhard, S. Buecheler, and A. N. Tiwari. Technological status of Cu(In,Ga)$(Se,S)_2$-based photovoltaics. *Solar Energy Materials and Solar Cells*, 119:287–290, December 2013.

[87] L. Ribeaucourt, G. Savidand, D. Lincot, and E. Chassaing. Electrochemical study of one-step electrodeposition of copperindiumgallium alloys in acidic conditions as precursor layers for Cu(In,Ga)Se_2 thin film solar cells. *Electrochimica Acta*, 56(19):6628–6637, July 2011.

[88] A. Duchatelet, T. Sidali, N. Loones, G. Savidand, E. Chassaing, and D. Lincot. 12.4% Efficient Cu(In,Ga)Se_2 solar cell prepared from one step electrodeposited CuInGa oxide precursor layer. *Solar Energy Materials and Solar Cells*, 119:241–245, December 2013.

[89] M Kaelin, D Rudmann, F Kurdesau, H Zogg, T Meyer, and A N Tiwari. Low-cost CIGS solar cells by paste coating and selenization. *Thin Solid Films*, 480-481:486–490, June 2005.

[90] Alexander R Uhl, Carolin Fella, Adrian Chiril, Marc R Kaelin, Lassi Karvonen, Anke Weidenkaff, Camelia N Borca, Daniel Grolimund, Yaroslav E Romanyuk, and Ayodhya N Tiwari. Non-vacuum deposition of Cu(In,Ga)Se_2 absorber layers from binder free, alcohol solutions. *Prog. Photovolt: Res. Appl.*, 20(January):526–533, 2012.

[91] Eunjoo Lee, Se Jin Park, Jin Woo Cho, Jihye Gwak, Min-Kyu Oh, and Byoung Koun Min. Nearly carbon-free printable CIGS thin films for solar cell applications. *Solar Energy Materials and Solar Cells*, 95(10):2928–2932, October 2011.

[92] David B. Mitzi, Min Yuan, Wei Liu, Andrew J. Kellock, S. Jay Chey, Vaughn Deline, and Alex G. Schrott. A High-Efficiency Solution-Deposited Thin-Film Photovoltaic Device. *Advanced Materials*, 20(19):3657–3662, October 2008.

[93] David B. Mitzi, Min Yuan, Wei Liu, Andrew J. Kellock, S. Jay Chey, Lynne Gignac, and Alex G. Schrott. Hydrazine-based deposition route for device-quality CIGS films. *Thin Solid Films*, 517(7):2158–2162, February 2009.

[94] Teodor K Todorov, Oki Gunawan, Tayfun Gokmen, and David B Mitzi. Solution-processed Cu(In,Ga)$(S,Se)_2$ absorber yielding a 15.2 % efficient solar cell. (January 2012):82–87, 2013.

[95] Leo J. van der Pauw. A method of measuring the resistivity and Hall coefficient on lamellae of arbitrary shape. *Philips Technical Review*, 20:220–224, 1958.

[96] Henry J. Snaith. How Should You Measure Your Excitonic Solar Cells? *Energy & Environmental Science*, 5(4):6513, 2012.

[97] Timothy J Coutts and David L Young. Characterization of Transparent Conducting Oxides. *Renewable Energy*, (August):58–65, 2000.

[98] Gregory J. Exarhos and Xiao-Dong Zhou. Discovery-based design of transparent conducting oxide films. *Thin Solid Films*, 515(18):7025–7052, June 2007.

[99] Yoshiyuki Abe and Noriko Ishiyama. Titanium-doped indium oxide films prepared by d.c. magnetron sputtering using ceramic target. *Journal of Materials Science*, 41(22):7580–7584, October 2006.

[100] Ryota Hashimoto, Yoshiyuki Abe, and Tokio Nakada. High Mobility Titanium-Doped In_2O_3 Thin Films Prepared by Sputtering/Post-Annealing Technique. *Applied Physics Express*, 1(1):015002, January 2008.

[101] R Gupta, K Ghosh, S Mishra, and P Kahol. Opto-electrical properties of Ti-doped In_2O_3 thin films grown by pulsed laser deposition. *Applied Surface Science*, 253(24):9422–9425, October 2007.

[102] Jong-Hyun Heo, Ki-Young Jung, Dong-Joo Kwak, Don-Kyu Lee, and Youl-Moon Sung. Fabrication of Titanium-Doped Indium Oxide Films for Dye-Sensitized Solar Cell Application Using Reactive RF Magnetron Sputter Method. *IEEE Transactions on Plasma Science*, 37(8):1586–1592, August 2009.

[103] J W Bowers, H M Upadhyaya, S Calnan, R Hashimoto, T Nakada, and A N Tiwari. Development of Nano-TiO_2 Dye Sensitised Solar Cells on High Mobility Transparent Conducting Oxide Thin Films. *Progress in Photovoltaics: Research and Applications*, 17:265–272, 2009.

[104] J.W. Bowers, H.M. Upadhyaya, T. Nakada, and a.N. Tiwari. Effects of surface treatments on high mobility ITiO coated glass substrates for dye sensitized solar cells and their tandem solar cell applications. *Solar Energy Materials and Solar Cells*, 94(4):691–696, April 2010.

[105] Yuzo Shigesato, Satoru Takaki, and Takeshi Haranoh. Electrical and structural properties of low resistivity tin-doped indium oxide films. *Journal of Applied Physics*, 71(7):3356, 1992.

[106] S. Seyrling, S. Bucheler, A. Chirila, J. Perrenoud, S. Wenger, T. Nakada, M. Gratzel, and A.N. Tiwari. Development of Multijunction Thin Film Solar Cells. *2009 34th IEEE Photovoltaic Specialists Conference (PVSC)*, pages 000622–000625, June 2009.

[107] W.L. Wang, H. Lin, J. Zhang, X. Li, a. Yamada, M. Konagai, and J.B. Li. Experimental and simulation analysis of the dye sensitized solar cell/Cu(In,Ga)Se_2 solar cell tandem structure. *Solar Energy Materials and Solar Cells*, 94(10):1753–1758, October 2010.

[108] Sophie Wenger, Sieghard Seyrling, Ayodhya N. Tiwari, and Michael Gratzel. Fabrication and performance of a monolithic dye-sensitized TiO_2/Cu(In,Ga)Se_2 thin film tandem solar cell. *Applied Physics Letters*, 94(17):173508, 2009.

[109] Sophie Wenger. *Strategies to Optimizing Dye-Sensitized Solar Cells: Organic Sensitizers, Tandem Device Structures, and Numerical Device Modeling.* PhD thesis, ÉCOLE POLYTECHNIQUE FÉDÉRALE DE LAUSANNE (EPFL), 2010.

[110] S Ito, H Matsui, K Okada, S Kusano, T Kitamura, Y Wada, and S Yanagida. Calibration of solar simulator for evaluation of dye-sensitized solar cells. *Solar Energy Materials and Solar Cells*, 82(3):421–429, May 2004.

[111] J D Perkins, T Gennett, J E Leisch, R Sundaramoorthy, I L Repins, M F A M Van Hest, and D S Ginley. Amorphous transparent conductors for PV applications. *Photovoltaic Specialists Conference (PVSC), 2010 35th IEEE*, 85:989–991, 2010.

[112] R. Martins, P. Barquinha, a. Pimentel, L. Pereira, and E. Fortunato. Transport in high mobility amorphous wide band gap indium zinc oxide films. *Physica Status Solidi (a)*, 202(9):R95–R97, July 2005.

[113] R.K. Gupta, K. Ghosh, S.R. Mishra, and P.K. Kahol. High mobility Ti-doped In_2O_3 transparent conductive thin films. *Materials Letters*, 62(6-7):1033–1035, March 2008.

[114] Matthew P Taylor, Dennis W Readey, Charles W Teplin, Maikel F a M Van Hest, Jeff L Alleman, Matthew S Dabney, Lynn M Gedvilas, Brian M Keyes, Bobby To, John D Perkins, and David S Ginley. The electrical, optical and structural properties of $In_xZn_{1x}O_y(0 \leqslant x \leqslant 1)$ thin films by combinatorial techniques. *Measurement Science and Technology*, 16(1):90–94, January 2005.

[115] Andrew Leenheer, John Perkins, Maikel van Hest, Joseph Berry, Ryan OHayre, and David Ginley. General mobility and carrier concentration relationship in transparent amorphous indium zinc oxide films. *Physical Review B*, 77(11):1–5, March 2008.

[116] Yeon Sik Jung, Ji Yoon Seo, Dong Wook Lee, and Duk Young Jeon. Influence of DC magnetron sputtering parameters on the properties of amorphous indium zinc oxide thin film. *Thin Solid Films*, 445(1):63–71, November 2003.

[117] Franz Urbach. The long-wavelength edge of photographic sensitivity and of the electronic Absorption of Solids [8]. *Physical Review*, 92(5):1324, 1953.

[118] E Mohler and B Thomas. Experimental Test of Theorectical Models for Urbach's Rule at Excitonic Absorption Edges. *Physical Review Letters*, 44(8):543–546, 1980.

[119] West Bengal. Optical and structural properties of amorphous and heat treated $In_{0.4}Se_{0.8}$ film of different thicknesses. *J. Mater. Sci.*, 23:4470–4476, 1988.

[120] K. Boubaker. A physical explanation to the controversial Urbach tailing universality. *The European Physical Journal Plus*, 126(1):10, January 2011.

[121] Jake William Bowers. Development of high efficiency dye sensitized solar cells : Novel conducting oxides, tandem devices and flexible solar cells. *Loughborough University*.

[122] S. Seyrling, S. Wenger, M. Grätzel, and a.N. Tiwari. Analysis of electronic and optical losses in Cu(In,Ga)Se_2 /dye sensitized cell tandem solar cells. *Energy Procedia*, 2(1):199–205, August 2010.